ESKİŞEHİR TECHNICAL UNIVERSITY
JOURNAL OF SCIENCE AND TECHNOLOGY

A – Applied Sciences and Engineering

Eskişehir Technical University Journal of Science and Technology A - Applied Sciences and Engineering (Other variant title: **Estuscience-Se**) is a peer-reviewed and refereed international journal published by Eskişehir Technical University. Since 2000, it has been regularly published and distributed biannually and it has been published quarterly and only electronically since 2016.

The journal accepts only manuscripts written in English.
The journal issues are published electronically in **March, June**, **September**, and **December**.

Eskişehir Technical University Journal of Science and Technology A - Applied Sciences and Engineering is an international peer-reviewed and refereed journal published by Eskişehir Technical University.

The journal is dedicated to the dissemination of knowledge in applied sciences and engineering disciplines.

The journal aims to publish high quality, original international scientific research articles with specific contributions to the literature in the field of engineering and applied sciences. The journal publishes research papers in the fields of applied science and technology such as Physics, Biology, Mathematics, Statistics, Chemistry and Chemical Engineering, Environmental Sciences and Engineering, Civil Engineering, Earth and Atmospheric Sciences, Electrical and Electronical Engineering, Computer Science and Informatics, Materials Sciences and Engineering, Mechanical Engineering, Mining Engineering, Industrial Engineering, Aeronautics and Astronautics, Pharmaceutical Sciences.

The journal publishes original research articles and special issue articles. All articles are peer-reviewed and the articles that have been evaluated are ensured to meet with researchers as soon as possible.

ABOUT

Eskişehir Technical University Journal of Science and Technology A - Applied Sciences and Engineering (**Estuscience-Se**) is a peer-reviewed and refereed international journal published by Eskişehir Technical University. Since 2000, it has been regularly published and distributed biannually and it has been published quarterly and only electronically since 2016.

The journal accepts only manuscripts written in English.

The journal issues are published electronically in **MARCH, JUNE, SEPTEMBER**, and **DECEMBER.**

AIM AND SCOPE

Eskişehir Technical University Journal of Science and Technology A - Applied Sciences and Engineering is an international peer-reviewed and refereed journal published by Eskişehir Technical University.

The journal is dedicated to the dissemination of knowledge in applied sciences and engineering disciplines.

The journal aims to publish high quality, original international scientific research articles with specific contributions to the literature in the field of engineering and applied sciences. The journal publishes research papers in the fields of applied science and technology such as Physics, Biology, Mathematics, Statistics, Chemistry and Chemical Engineering, Environmental Sciences and Engineering, Civil Engineering, Earth and Atmospheric Sciences, Electrical and Electronical Engineering, Computer Science and Informatics, Materials Sciences and Engineering, Mechanical Engineering, Mining Engineering, Industrial Engineering, Aeronautics and Astronautics, Pharmaceutical Sciences.

The journal publishes original research articles and special issue articles. All articles are peer-reviewed and the articles that have been evaluated are ensured to meet with researchers as soon as possible.

PEER REVIEW PROCESS

Manuscripts are first reviewed by the editorial board in terms of its its journal's style rules scientific content, ethics and methodological approach. If found appropriate, the manuscript is then send to at least two renown referees by editor. The decision in line with the referees may be an acceptance, a rejection or an invitation to revise and resubmit. Confidential review reports from the referees will be kept in archive. All submission process manage through the online submission systems.

OPEN ACCESS POLICY

This journal provides immediate open access to its content on the principle that making research freely available to the public supports a greater global exchange of knowledge. Copyright notice and type of licence : **CC BY-NC-ND.**

PRICE POLICY

Eskişehir Technical University Journal of Science and Technology A - Journal of Applied Sciences and Engineering is an English, peer-reviewed, scientific, free of charge open-access-based journal. The author is not required to pay any publication fees or article processing charges (APCs) for peer-review administration and management, typesetting, and open-access. Articles also receive Digital Object Identifiers (DOIs) from the CrossRef organization to ensure they are always available.

ETHICAL RULES
You can reach the Ethical Rules in our journal in full detail from the link below:

https://dergipark.org.tr/en/pub/estubtda/policy

Ethical Principles and Publication Policy

Policy & Ethics
Assessment and Publication

As a peer-reviewed journal, it is our goal to advance scientific knowledge and understanding. We have outlined a set of ethical principles that must be followed by all authors, reviewers, and editors.

All manuscripts submitted to our journals are pre-evaluated in terms of their relevance to the scope of the journal, language, compliance with writing instructions, suitability for science, and originality, by taking into account the current legal requirements regarding copyright infringement and plagiarism. Manuscripts that are evaluated as insufficient or non-compliant with the instructions for authors may be rejected without peer review.

Editors and referees who are expert researchers in their fields assess scientific manuscripts submitted to our journals. A blind peer review policy is applied to the evaluation process. The Editor-in-Chief, if he/she sees necessary, may assign an Editor for the manuscript or may conduct the scientific assessment of the manuscript himself/herself. Editors may also assign referees for the scientific assessment of the manuscript and make their decisions based on reports by the referees. Articles are accepted for publication on the understanding that they have not been published and are not going to be considered for publication elsewhere. Authors should certify that neither the manuscript nor its main contents have already been published or submitted for publication in another journal.

The Journal; Implements the Publication Policy and Ethics guidelines to meet high-quality ethical standards for authors, editors and reviewers:

Duties of Editors-in-Chief and co-Editors

The crucial role of the journal Editor-in-Chief and co-Editors is to monitor and ensure the fairness, timeliness, thoroughness, and civility of the peer-review editorial process. The main responsibilities of Editors-in-Chief are as follows:

• Selecting manuscripts suitable for publication while rejecting unsuitable manuscripts,
• Ensuring a supply of high-quality manuscripts to the journal by identifying important,
• Increasing the journal's impact factor and maintaining the publishing schedule,
• Providing strategic input for the journal's development,

Duties of Editors

The main responsibilities of editors are as follows:

• An editor must evaluate the manuscript objectively for publication, judging each on its quality without considering the nationality, ethnicity, political beliefs, race, religion, gender, seniority, or institutional affiliation of the author(s). Editors should decline any assignment when there is a potential for conflict of interest.
• Editors must ensure the document(s) sent to the reviewers does not contain information of the author(s) and vice versa.
• Editors' decisions should be provided to the author(s) accompanied by the reviewers' comments and recommendations unless they contain offensive or libelous remarks.
• Editors should respect requests (if well reasoned and practicable) from author(s) that an individual should not review the submission.
• Editors and all staff members should guarantee the confidentiality of the submitted manuscript.
• Editors should have no conflict of interest with respect to articles they reject/accept. They must not have a conflict of interest with the author(s), funder(s), or reviewer(s) of the manuscript.
• Editors should strive to meet the needs of readers and authors and to constantly improve the journal.

Duties of Reviewers/Referees

The main responsibilities of reviewers/referees are as follows:

• Reviewers should keep all information regarding papers confidential and treat them as privileged information.
• Reviews should be conducted objectively, with no personal criticism of the author.
• Reviewers assist in the editorial decision process and as such should express their views clearly with supporting arguments.
• Reviewers should complete their reviews within a specified timeframe (maximum thirty-five (35) days). In the event that a reviewer feels it is not possible for him/her to complete the review of the manuscript within a stipulated time, then this information must be communicated to the editor so that the manuscript could be sent to another reviewer.
• Unpublished materials disclosed in a submitted manuscript must not be used in a reviewer's personal research without the written permission of the author. Information contained in an unpublished manuscript will remain confidential and must not be used by the reviewer for personal gain.
• Reviewers should not review manuscripts in which they have conflicts of interest resulting from competitive, collaborative, or other relationships or connections with any of the authors, companies, or institutions connected to the papers.

• Reviewers should identify similar work in published manuscripts that has not been cited by the author. Reviewers should also notify the Editors of significant similarities and/or overlaps between the manuscript and any other published or unpublished material.

Duties of Authors
The main responsibilities of authors are as follows:

• The author(s) should affirm that the material has not been previously published and that they have not transferred elsewhere any rights to the article.
• The author(s) should ensure the originality of the work and that they have properly cited others' work in accordance with the reference format.
• The author(s) should not engage in plagiarism or in self-plagiarism.
• On clinical and experimental humans and animals, which require an ethical committee decision for research in all branches of science;
All kinds of research carried out with qualitative or quantitative approaches that require data collection from the participants by using survey, interview, focus group work, observation, experiment, interview techniques,
Use of humans and animals (including material/data) for experimental or other scientific purposes,
• Clinical studies on humans,
• Studies on animals,
• Retrospective studies in accordance with the law on the protection of personal data, (Ethics committee approval should have been obtained for each individual application, and this approval should be stated and documented in the article.)
Information about the permission (board name, date, and number) should be included in the "Method" section of the article and also on the first/last page.
During manuscript upload, the "Ethics Committee Approval" file should be uploaded to the system in addition to the manuscript file.
In addition, in case reports, it is necessary to include information on the signing of the informed consent/ informed consent form in the manuscript.
• The author(s) should suggest no personal information that might make the identity of the patient recognizable in any form of description, photograph, or pedigree. When photographs of the patient were essential and indispensable as scientific information, the author(s) have received consent in written form and have clearly stated as much.
• The author(s) should provide the editor with the data and details of the work if there are suspicions of data falsification or fabrication. Fraudulent data shall not be tolerated. Any manuscript with suspected fabricated or falsified data will not be accepted. A retraction will be made for any publication which is found to have included fabricated or falsified data.
• The author(s) should clarify everything that may cause a conflict of interests such as work, research expenses, consultant expenses, and intellectual property.
• The author(s) must follow the submission guidelines of the journal.
• The author(s) discover(s) a significant error and/or inaccuracy in the submitted manuscript at any time, then the error and/or inaccuracy must be reported to the editor.
• The author(s) should disclose in their manuscript any financial or other substantive conflicts of interest that might be construed to influence the results or interpretation of their manuscript. All sources of financial support should be disclosed under the heading of "Acknowledgment" or "Contribution".
• The corresponding author(s) must ensure that all appropriate co-authors are not included in the manuscript, that author names are not added or removed and that the authors' address information is not changed after the review begins and that all co-authors see and approve the

final version of the manuscript at every stage of the manuscript. All significant contributors should be listed as co-authors. Other individuals who have participated in significant aspects of the research work should be considered contributors and listed under "Author Contribution".

Cancellations/Returns

Articles/manuscripts may be returned to the authors in order to increase the authenticity and/or reliability and to prevent ethical breaches, and even if articles have been accepted and/or published, they can be withdrawn from publication if necessary. The Editor-in-Chief of the journal has the right to return or withdraw an article/manuscript in the following situations:

• When the manuscript is not within the scope of the journal,
• When the scientific quality and/or content of the manuscript do not meet the standards of the journal and a referee review is not necessary,
• When there is proof of ruling out the findings obtained by the research, (When the article/manuscript is undergoing an assessment or publication process by another journal, congress, conference, etc.,)
• When the article/manuscript was not prepared in compliance with scientific publication ethics,
• When any other plagiarism is detected in the article/manuscript,
• When the authors do not perform the requested corrections within the requested time (maximum twenty-one (21) days),
• When the author does not submit the requested documents/materials/data etc. within the requested time,
• When the requested documents/materials/data etc. submitted by the author are missing for the second time,
• When the study includes outdated data,
• When the authors make changes that are not approved by the editor after the manuscript was submitted,
• When an author is added/removed, the order of the authors is changed, the corresponding author is altered, or the addresses of the authors are changed in the article that is in the evaluation process,
• When a statement is not submitted indicating that approval of the ethics committee permission was obtained for the following (including retrospective studies):
• When human rights or animal rights are violated,

ETHICAL ISSUES
Plagiarism

The use of someone else's ideas or words without a proper citation is considered plagiarism and will not be tolerated. Even if a citation is given, if quotation marks are not placed around words taken directly from other authors' work, the author is still guilty of plagiarism. Reuse of the author's own previously published words, with or without a citation, is regarded as self-plagiarism.

All manuscripts received are submitted to iThenticate®, which compares the content of the manuscript with a database of web pages and academic publications. Manuscripts are judged to be plagiarized or self-plagiarized, based on the iThenticate® report or any other source of information, will be rejected. Corrective actions are proposed when plagiarism and/or self-plagiarism is detected after publication. Editors should analyze the article and decide whether a corrected article or retraction needs to be published.

Open-access theses are considered as published works and they are included in the similarity checks.

iThenticate® report should have a maximum of 11% from a single source, and a maximum of 25% in total.

AUTHOR GUIDELINES

All manuscripts must be submitted electronically.

You will be guided stepwise through the creation and uploading of the various files. There are no page charges. Papers are accepted for publication on the understanding that they have not been published and are not going to be considered for publication elsewhere. Authors should certify that neither the manuscript nor its main contents have already been published or submitted for publication in another journal. We ask a signed copyright to start the evaluation process. After a manuscript has been submitted, it is not possible for authors to be added or removed or for the order of authors to be changed. If authors do so, their submission will be cancelled.

Manuscripts may be rejected without peer review by the editor-in-chief if they do not comply with the instructions to authors or if they are beyond the scope of the journal. After a manuscript has been accepted for publication, i.e. after referee-recommended revisions are complete, the author will not be permitted to make any changes that constitute departures from the manuscript that was accepted by the editor. Before publication, the galley proofs are always sent to the authors for corrections. Mistakes or omissions that occur due to some negligence on our part during final printing will be rectified in an errata section in a later issue.

This does not include those errors left uncorrected by the author in the galley proof. The use of someone else's ideas or words in their original form or slightly changed without a proper citation is considered plagiarism and will not be tolerated. Even if a citation is given, if quotation marks are not placed around words taken directly from another author's work, the author is still guilty of plagiarism. All manuscripts received are submitted to iThenticateR, a plagiarism checking system, which compares the content of the manuscript with a vast database of web pages and academic publications. In the received iThenticateR report; The similarity rate is expected to be below 25%. Articles higher than this rate will be rejected.

Uploading Articles to the Journal
Authors should prepare and upload 2 separate files while uploading articles to the journal. First, the Author names and institution information should be uploaded so that they can be seen, and then (using the additional file options) a separate file should be uploaded with the Author names and institution information completely closed. When uploading their files with closed author names, they will select the "Show to Referee" option, so that the file whose names are closed can be opened to the referees.

Prepatation of Manuscript

Style and Format
Manuscripts should be **single column** by giving one-spaced with 2.5-cm margins on all sides of the page, in Times New Roman font (font size 11). Every page of the manuscript, including the title page, references, tables, etc., should be numbered. All copies of the manuscript should also have line numbers starting with 1 on each consecutive page.

Manuscripts must be upload as word document (*.doc, *.docx vb.). **Please avoid uploading** *texts in *.pdf format.*

Symbols, Units and Abbreviations
Standard abbreviations and units should be used; SI units are recommended. Abbreviations should be defined at first appearance, and their use in the title and abstract should be avoided. Generic names of chemicals should be used. Genus and species names should be typed in italic or, if this is not available, underlined.

Please refer to equations with capitalisation and unabbreviated (e.g., as given in Equation (1)).

Manuscript Content
Articles should be divided into logically ordered and numbered sections. Principal sections should be numbered consecutively with Arabic numerals (1. Introduction, 2. Formulation of problem, etc.) and subsections should be numbered 1.1., 1.2., etc. Do not number the Acknowledgements or References sections. The text of articles should be, if possible, divided into the following sections: Introduction, Materials and Methods (or Experimental), Results, Discussion, and Conclusion.

Title and contact information
The first page should contain the full title in sentence case (e.g., Hybrid feature selection for text classification), the full names (last names fully capitalised) and affiliations (in English) of all authors (Department, Faculty, University, City, Country, E-mail), and the contact e-mail address for the clearly identified corresponding author. The first page should contain the full title, abstract and keywords (both English and Turkish).

Abstract
The abstract should provide clear information about the research and the results obtained, and should not exceed 300 words. The abstract should not contain citations and must be written in Times New Roman font with font size 9.

Keywords
Please provide 3 to 5 keywords which can be used for indexing purposes.

Introduction

The motivation or purpose of your research should appear in the "Introduction", where you state the questions you sought to answer, and then provide some of the historical basis for those questions.

Methods

Provide sufficient information to allow someone to repeat your work. A clear description of your experimental design, sampling procedures, and statistical procedures is especially important in papers describing field studies, simulations, or experiments. If you list a product (e.g., animal food, analytical device), supply the name and location of the manufacturer. Give the model number for equipment used.

Results

Results should be stated concisely and without interpretation.

Discussion

Focus on the rigorously supported aspects of your study. Carefully differentiate the results of your study from data obtained from other sources. Interpret your results, relate them to the results of previous research, and discuss the implications of your results or interpretations.

Conclusion

This should state clearly the main conclusions of the research and give a clear explanation of their importance and relevance. Summary illustrations may be included.

Acknowledgments

Acknowledgments of people, grants, funds, etc. should be placed in a separate section before the reference list. The names of funding organizations should be written in full.

Conflict of Interest Statement

The authors are obliged to present the conflict of interest statement at the end of the article after the acknowledgments section.

CRediT Author Statement

Write the authors' contributions in detail using the specified CRediT notifications. Authors may have contributed in more than one role. The corresponding author is responsible for ensuring that descriptions are accurate and accepted by all authors.

CRediT Notifications	Explanation
Conceptualization	Ideas; formulation or evolution of overarching research goals and aims
Methodology	Development or design of methodology; creation of models
Software	Programming, software development; designing computer programs; implementation of the computer code and supporting algorithms; testing of existing code components

Validation	Verification, whether as a part of the activity or separate, of the overall replication/ reproducibility of results/experiments and other research outputs
Formal analysis	Application of statistical, mathematical, computational, or other formal techniques to analyse or synthesize study data
Investigation	Conducting a research and investigation process, specifically performing the experiments, or data/evidence collection
Resources	Provision of study materials, reagents, materials, patients, laboratory samples, animals, instrumentation, computing resources, or other analysis tools
Data Curation	Management activities to annotate (produce metadata), scrub data and maintain research data (including software code, where it is necessary for interpreting the data itself) for initial use and later reuse
Writing – Original Draft	Preparation, creation and/or presentation of the published work, specifically writing the initial draft (including substantive translation)
Writing – Review & Editing	Preparation, creation and/or presentation of the published work by those from the original research group, specifically critical review, commentary, or revision – including pre-or post-publication stages
Visualization	Preparation, creation and/or presentation of the published work, specifically visualization/ data presentation
Supervision	Oversight and leadership responsibility for the research activity planning and execution, including mentorship external to the core team
Project administration	Management and coordination responsibility for the research activity planning and execution
Funding acquisition	Acquisition of the financial support for the project leading to this publication

References

Writting Style; **AMA; References Writting format** should be used in the reference writing of our journal. If necessary, at this point, the reference writings of the articles published in our article can be examined.

Citations in the text should be identified by numbers in square brackets. The list of references at the end of the paper should be given in order of their first appearance in the text. All authors should be included in reference lists unless there are 10 or more, in which case only the first 10 should be given, followed by 'et al.'. Do not use individual sets of square brackets for citation numbers that appear together, e.g., [2,3,5–9], not [2], [3], [5]–[9]. Do not include personal communications, unpublished data, websites, or other unpublished materials as references,

although such material may be inserted (in parentheses) in the text. In the case of publications in languages other than English, the published English title should be provided if one exists, with an annotation such as "(article in Turkish with an abstract in English)". If the publication was not published with an English title, cite the original title only; do not provide a self-translation. References should be formatted as follows (please note the punctuation and capitalisation):

Journal articles
Journal titles should be abbreviated according to ISI Web of Science abbreviations.
Guyon I, Elisseeff A. An introduction to variable and feature selection. J Mach Learn Res 2003; 3: 1157-1182.

Izadpanahi S, Ozcınar C, Anbarjafari G, Demirel H. Resolution enhancement of video sequences by using discrete wavelet transform and illumination compensation. Turk J Elec Eng & Comp Sci 2012; 20: 1268-1276.

Books
Haupt RL, Haupt SE. Practical Genetic Algorithms. 2nd ed. New York, NY, USA: Wiley, 2004.
Kennedy J, Eberhart R. Swarm Intelligence. San Diego, CA, USA: Academic Press, 2001.

Chapters in books
Poore JH, Lin L, Eschbach R, Bauer T. Automated statistical testing for embedded systems. In: Zander J, Schieferdecker I, Mosterman PJ, editors. Model-Based Testing for Embedded Systems. Boca Raton, FL, USA: CRC Press, 2012. pp. 111-146.

Conference proceedings
Li RTH, Chung SH. Digital boundary controller for single-phase grid-connected CSI. In: IEEE 2008 Power Electronics Specialists Conference; 15–19 June 2008; Rhodes, Greece. New York, NY, USA: IEEE. pp. 4562-4568.

Theses
Boynukalın Z. Emotion analysis of Turkish texts by using machine learning methods. MSc, Middle East Technical University, Ankara, Turkey, 2012.

Tables and Figures
All illustrations (photographs, drawings, graphs, etc.), not including tables, must be labelled "Figure." Figures must be submitted in the manuscript.

All tables and figures must have a caption and/or legend and be numbered (e.g., Table 1, Figure 2), unless there is only one table or figure, in which case it should be labelled "Table" or "Figure" with no numbering. Captions must be written in sentence case (e.g., Macroscopic appearance of the samples.). The font used in the figures should be Times New Roman. If symbols such as ×, μ, η, or ν are used, they should be added using the Symbols menu of Word.

All tables and figures must be numbered consecutively as they are referred to in the text. Please refer to tables and figures with capitalisation and unabbreviated (e.g., "As shown in Figure 2…", and not "Fig. 2" or "figure 2").

The resolution of images should not be less than 118 pixels/cm when width is set to 16 cm. Images must be scanned at 1200 dpi resolution and submitted in jpeg or tiff format. Graphs and diagrams must be drawn with a line weight between 0.5 and 1 point. Graphs and diagrams with

a line weight of less than 0.5 point or more than 1 point are not accepted. Scanned or photocopied graphs and diagrams are not accepted.

Figures that are charts, diagrams, or drawings must be submitted in a modifiable format, i.e. our graphics personnel should be able to modify them. Therefore, if the program with which the figure is drawn has a "save as" option, it must be saved as *.ai or *.pdf. If the "save as" option does not include these extensions, the figure must be copied and pasted into a blank Microsoft Word document as an editable object. It must not be pasted as an image file (tiff, jpeg, or eps) unless it is a photograph.

Tables and figures, including caption, title, column heads, and footnotes, must not exceed 16 × 20 cm and should be no smaller than 8 cm in width. For all tables, please use Word's "Create Table" feature, with no tabbed text or tables created with spaces and drawn lines. Please do not duplicate information that is already presented in the figures.

Article Corrections and Uploading to the System
Authors should upload the desired edits for their articles without destroying or changing the Template file of the article, by selecting and specifying the relevant edits as Colored, and also submit the Clean version of the article in 2 separate files (using the Additional file option if necessary). * In case of submitting a corrected article, a separate File in Reply to the Referees must be prepared and the "Reply to the Referees" option in the Add additional file option should be checked and uploaded. If a separate file is not prepared in response to the referees, the Author will definitely be asked to upload the relevant file again and the evaluation will be in the pending phase.

CONTENTS

RESEARCH ARTICLE

RESEARCH ARTICLE

SELECTING THE OPTIMUM AMOUNT OF RECYCLED POLYPROPYLENE NONWOVEN WASTE IN SPUNBOND PRODUCTION FOR SUSTAINABILITY

Züleyha DEĞİRMENCİ [1], *

[1] Gaziantep University, Textile Engineering Department, Gaziantep, Türkiye
degirmenci@gantep.edu.tr 🆔 0000-0002-8669-4968

Abstract

During the Covid-19 pandemic, there was a significant increase in the use of polypropylene-based masks, leading to challenges related to raw material waste and supply limitations. This study aims to identify the optimal ratio of recycled and standard polypropylene fibers to produce a nonwoven spun-bond fabric with the best possible strength and elongation properties. In the rapidly expanding industry, polypropylene (PP)-based nonwoven fabrics (spunbond and meltblown) are increasingly being recycled by converting fabric waste into granules, which are then blended with virgin PP in specific proportions for reuse in production. This research focuses on analyzing the tensile strength and elongation at break of spunbond fabrics. First, fabric wastes from Spunbond-Meltblown processes were converted into granules, and their melt flow index (MFI) values were measured. These granules were then blended with virgin polypropylene fibers in varying proportions, resulting in five different spunbond fabric samples. The mechanical properties of these samples were compared with those of a fabric produced solely from virgin PP. The optimal mixing ratio of recycled to virgin fibers was then determined based on the results. The MFI of the recycled PP1 waste was measured at 38, while the MFI of a 75%-25% Spunbond-Meltblown waste blend (Recycle-PP5) was 104. Spunbond fabrics were produced by blending Recycle-PP1 granules with virgin raw material at ratios ranging from 0% to 20%. It was found that a 10% blend of recycled granules yielded the best results without compromising fabric quality. Higher proportions of recycled granules led to defects in the fabric. For instance, the tensile strength of spunbond fabrics containing 20% Recycle-PP5 granules decreased by approximately 26.9% compared to the fabric produced with 100% virgin PP. This study demonstrates the potential for using recycled granules in spunbond fabric production for specific applications, based on the observed strength properties. A key distinction of this research from existing literature is the identification of the most effective blending ratio of recycled and virgin polypropylene in a conventional production setting.

Keywords

1. INTRODUCTION

Polypropylene is a natural white-colored material obtained by polymerization of propylene monomer produced from "Naphtha", one of the crude oil derivatives. Since derivatives obtained from crude oil at an average rate of 97% are used in its production, its availability and price situation is directly related to world crude oil reserves and prices. Polypropylene is a synthetic fiber, it is one of the thermoplastics that can be reshaped once produced without undergoing and any chemical changes, and is widely used in daily life and industry. Compared to other polymer fibers, it is a 'versatile' fiber whose usage area is increasing day by day. Currently, there are 3 types of polypropylene raw materials used in daily life. Polypropylene homopolymer is produced only from propylene molecules. It is very soft since there is

---

no ethylene additive. It is used in the production of materials such as bags. The percentage of ethylene in the polypropylene block copolymer is 3%. It is not very resistant to temperature. It can only be used in the manufacture of plastic pipes that can be used in cold water transmission lines. Polypropylene random copolymer is a raw material whose ethylene percentage is between 3-7%. It can be used where very high temperature and pressure resistance is required. Polypropylene is a highly versatile material used across various industries due to its lightweight, durable, and chemical-resistant properties. In the textile industry, it is utilized for underwear, linings, denim, socks, swimwear, ski wear, and military clothing. For outdoor furniture and upholstery, it features in weather-resistant fabrics like taslan and chenille. In home textiles, it is found in carpets, furniture fabrics, and curtains. The automotive sector uses polypropylene for durable interior and exterior parts, while the construction industry benefits from its use in geotextiles and waterproofing materials. Additionally, it is essential for cable insulation, bottle and pipe manufacturing, and medical applications like syringes and surgical trays. Its adaptability makes it indispensable across these fields.Polypropylene shows very good fatigue resistance. It is low cost and has good impact resistance. It has a low coefficient of friction and provides very good electrical insulation. Chemical resistance is good. It is suitable for all thermoplastic processing processes. The moisture retention rate is less than 0.1%. It has high tensile strength but low abrasion resistance and low resistance to atmospheric effects. Ironing should be applied at lower temperatures than cotton, wool and nylon due to its low melting temperature, difficulty in dyeing after production, low UV resistance and thermal stability [1].

Polypropylene is used more and more in the field of plastic and technical textiles due to its easy availability and advantageous cost compared to other polymers. The increase in the interest in disposable products, especially with the Covid19 pandemic, has increased this consumption even more [2]. The use of disposable products brings with it two difficulties. The first of these is that the demand cannot be met; the second is the increase in the level of waste generated by these products. The importance of recycling is undeniable when it comes to sustainability. Therefore, it is very important to reintroduce the amount of waste generated during production in terms of economic and environmental aspects. The waste of nonwoven fabrics can be used in two ways. The first of these is the reprocessing of nonwoven fabrics produced from thermoplastic polypropylene polymers in the plastics industry. The other is the reprocessing of only spunbond fabrics in the spunbond fabric production machine in the form of feedback. However, the rate in the latter is quite low.

The increasing use of polypropylene and generation of waste during both production and post-consumer phases has emerged as a significant environmental challenge. Recycling these materials back into the production cycle is essential, not only to promote environmental sustainability but also to mitigate the rising costs of raw materials. An area of considerable interest is the optimization of blending ratios between recycled and virgin (standard) granules within production processes, as determining these optimal ratios could support the development of both economically viable and environmentally responsible manufacturing practices.

In response to these challenges, incorporating recycled polypropylene into existing production techniques, such as the spunbond process, presents a viable solution. However, the integration of recycled polypropylene demands a thorough examination of technical obstacles associated with nonwoven fabric manufacturing. By optimizing the blend of recycled and virgin polypropylene, industries can uphold high-quality standards while minimizing environmental impact. The complex nature of the spunbond process, influenced by numerous thermodynamic and aerodynamic factors, underscores the need to determine mixing ratios that preserve both mechanical properties and production efficiency. Thus, investigating these interactions is critical for advancing sustainable and efficient production practices.

Although the spunbond technique is the fastest technique in the production of nonwoven fabrics, the process conditions are quite complex [3,4]. With the help of a thermoplastic polypropylene pump melted

in the extruder, thousands of filaments are poured into the mold at the same time using constant pressure and a surface is formed [5,6] After this process, cold air is given to the mold at a certain flow rate. The filaments are oriented by the aerodynamic force between the belt fans. The applied drafting process ensures precise stacking of the filaments [4,7]. The most important parameters at this stage are the air permeability of the belt, the pore density and size of the filament fan screens, the distances of the towers and channels between the die and the belt, the size and number of die holes [8,3,1]. In order for these processes to be carried out properly, thermodynamic, aerodynamic and mechanical processes must be carried out in a controlled manner. For this, the MFI of the polypropylene polymer and the molecular weight distribution of the polymer are very important. In general terms, the more homogeneous the molecular weight, the less decomposition, combustion, or carbonization occurs during thermal processing and the easier the material is to be processed. In addition, the filter or mold does not clog, so the efficiency is high. Since the purest the raw material, the higher the production, the feeding of recycled polypropylene or edge waste to the system reduces the efficiency. Therefore, the amount of feedback that can be provided at the maximum level without reducing the quality varies. Therefore, nonwoven recycling fabric studies are becoming widespread [9-12]. Many studies on polypropylene are related to the plastics industry, but there are also studies using recycled polypropylene in the spunbond production line [13-17].

According to the literature chemical recycling [20-22] (melting and forming granules again) is simple but mainly limited to condensation polymers. Mechanical recycling [21,23] (carding and forming fiber again) is cost-effective, production efficiency is high and technology is well known; however, in this method pre-treatment is needed and this process may deteriorate the product's properties. From the point of this view recycling may not be the real solution for the mill, lanning the production line effectively is better.

In this study, unlike the literature, spunbond and meltblown fabrics were recycled and mixed at different rates to obtain granules again. As a result of the tests applied at the end of the first stage of the study, the most successful mixture was selected and these granules were mixed with pure polymer at different rates to produce spunbond fabrics. The strength and elongation values of the fabrics produced were compared with spunbond fabrics obtained from pure polypropylene.

Research Problem

 –To what extent can the different ratios of recycled pp be added to the pure pp?
 - What is the optimum recycled granule ratio and production method for the production of nonwoven fabrics?

Objectives

- Selecting the most suitable flow rate to obtain ranules again
-To study the mixing of recycled spunbond and melt blown granules to pure ones and measuring the performance.
 - Identify the optimal ratio by measuring the decreasing ratio of strength and elongation both machine and cross directions from pure one.

Research Hypotheses

- The recycled spunbond nonwoven fabrics have the similar strength and elongation values to those of pure nonwoven fabrics (or not?).
- Adding different ratios of recycled granules to pure one causes producing nonwoven fabrics with same quality (or not?).

2. EXPERIMENTAL

Recycling systems typically consist of five primary components: an extruder, filter, mold, coagulation bath, and shaper [10, 14]. The process involves melting and mixing the material in the extruder, purifying and further blending it in the filter, forming the material into filaments using the mold, cooling and stretching the filaments in the coagulation bath, and finally granulating the material with a cutter [17, 18]. Among these stages, filtration and material maturation are considered the most critical for ensuring high-quality output. An additional key factor is the purity of the raw materials used in the process, as it significantly impacts the overall efficiency and quality of the recycled product [11].
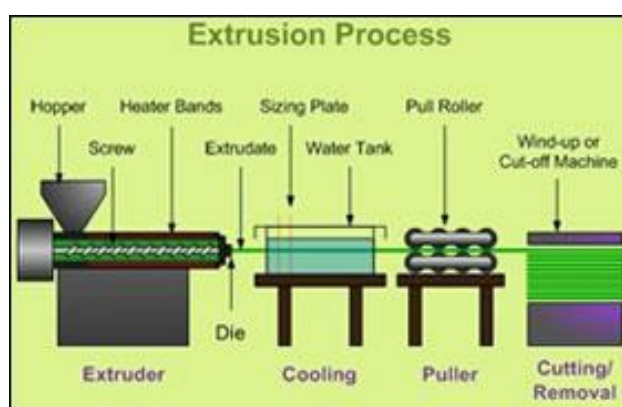
Figure 1. An example of classical extrusion process in a recycle mill [19]

In this study, meltblown fabrics produced from 1200 MFI polypropylene and spunbond fabrics produced from 38 MFI polypropylene were reprocessed into granules, both in their pure forms and as mixed formulations. These granules were then combined with standard polypropylene granules at varying ratios of 3%, 5%, 10%, 15%, and 20%, resulting in the production of five distinct spunbond fabric samples. To check the effect of ratio, a control sample of spunbond fabric made entirely from standard polypropylene was also produced, bringing the total to six different samples. The study utilized spunbond edge wastes derived from 38 MFI polymers and meltblown edge wastes from 1200 MFI polymers. To assess the performance of 24 MFI wastes, an additional sample containing 100% 24 MFI waste was produced. In this paper the standard pp refers to the raw material of the mill and the recycle one is obtained from the waste during production as pre-consumer. It was transformed to granul again and mixed to the original pp in the mill. Other details can not be shared because of the rules of mill. The exact blending ratios used in the study are presented in Table 1.

Table 1. Mixing ratio of spunbond ve meltblown waste

Sample codes	24 MFI Spunbond ratio	38 MFI Spunbond ratio	1200 MFI Melt Blown ratio
Recycle-PP1	%100		
Recycle-PP2		%100	
Recycle-PP3		%95	%5
Recycle-PP4		%90	%10
Recycle-PP5		%85	%15
Recycle-PP6		%80	%20

The purity of the raw material (waste) selected in the recycling process and the filter (mesh) to be used should be compatible with each other. For more fluid meltblown-weighted recycling processes, filters

with smaller pore sizes (higher frequency) should be used. In spunbond-weighted processes, filters with larger pores should be used [9,11]. In this study, a 3-layer filter with a porosity of 120*315*18 (mesh) was used and extruder temperatures were adjusted to obtain granules from the mixtures. Production details are given in Table 2.

Table 2. Recycling extruder regional temperatures

Material type	First region °C	Second region °C	Third region °C	Fourth region C	Fifth region°C	Sixth region°C	Seventh region °C
Spunbond	180	185	190	190	195	205	200
Mixture (Spunbond+Meltblown)	195	200	200	205	205	210	210

In terms of purity, nonwoven fabrics with added additives (such as hydrophilic, antistatic, FR, stabilizers, super hydrophobic, UV) can adversely affect the working parameters and even prevent filament formation. For this reason, it is necessary to collect wastes by classification and to use such mixtures in a controlled manner. No additives were used in this study, except for the blue and white dye used in the production of spunbond fabric.

The basic element in adjusting the forces during drafting is to thin the filament as much as possible without breaking. In order to withstand these forces, the molecular chain length of the polymer must be sufficient [18]. For spunbond, this expression can be followed by two values. The first is the difference between 24 and 38 MFI of PP polymer. 38 MFI polymers can operate at lower temperatures and pressures than 24 MFI polymers, and the final product can be obtained with a much softer handle [8]. Another is the distribution of the polymer chain length that makes up the polymer (it doesn't matter if it is 24 or 38 MFI) in the polymer content [18]. The lower (narrower) this distribution, the easier it is to process the polymer and adjust the parameters. More trouble-free productions can be realized. However, if the dispersion is wide, it will respond over a wider range of thermal and aerodynamic forces. However, while this wide range is sufficient to mature some polymers, it will be excessive for some other polymers. As a result, two situations may occur. In the first, burning/carbonization may occur in polymers at high temperatures, while in the other, breaks may occur in filaments that cannot mature before reaching the desired shrinkage amount. When production continues without breaking, filaments that cannot reach sufficient strength may naturally form low-strength fabrics.

It is known that recycled PP granules that can be added to the raw material have a negative effect on the chain lengths in the molecular structure of the polymer. However, since this may vary according to each production machine and the raw material used, how much recycled PP polymer can be used in percentage will be determined in this study. The parameters of the production are presented in Table 3.

Table 3. Production parameters of spunbond fabric

Parameters	Values	Parameters	Values
Extruder Temperature	210-245 °C	Calendar Temperatures	133-134°C
Filter Temperature	238-237 °C	Calendar Printing	85-89 N/mm
Pump Temperature	235-245 °C	Number of Mold Holes	20.000
Pump Speed	19-20 rpm	Die Hole Diameter	30-35 microns
Mold Temperatures	231-245 °C	Raw material PP	24 MFI
Exhaust Fan Speed	750-1050 rpm	Color	White (%60 TiO_2)
Filament Fan Cycle	900-1250 rpm	Belt Fan Cycle	600-780
Filament Fan Air Temperature	10-12°C	Belt Era	270-280 m/min

Recycled PP will be added at rates of 0, 3, 5, 10, 15, and 20% to the pure substance with a MFI of 24. The highest rate that can operate without breakage/problem in the spunbond machine will be determined and its strengths will be examined.

Recycled granules from nonwoven waste will be tested according to the ISO 1133 standard for the determination of melt mass flow rate (MFR) and melt volume flow rate (MVR). In short, the MFI/MFR test is a measure of how much-molten plastic (230°C / 2.16 Kg) flows in 10 minutes (g/10 min) through the standard nozzle under a certain temperature and load. The temperatures and mass applied for each polymer are different and are given in the standards where the polymer is defined. In the PP polymer standard, the temperature is specified as 230 °C and the mass as 2.16 kg. The tests were performed on the Zwick Roell Mflow instrument.

Zwcik Roell brand universal ZwickiLine 0.5 kN model test device was used for the strength of the fabrics produced with recycled polymers. Tests are applied according to ASTM E 8 Standard. 3 tests were aplied as adviced in this standard and the average is used Tests were carried out along both the machine (MD) and fabric width (CD) directions for the study in the test device, in which the breaking strength and elongation at break values were determined. In "ASTM E 8" method, the testing machine shall be operated such that the rate of stress application in the linear elastic region is between 1.15 and 11.5 MPa/s [10 000 and 100 000 psi/min]. The speed of the testing machine shall not be increased in order to maintain a stressing rate when the specimen begins to yield. It is not recommended that the testing machine be operated in closed-loop control using the force signal through yield; however closed-loop control of the force signal can be used in the linear-elastic portion of the test.

3. RESULTS and DISCUSSION

3.1. Determination of MFI of Recycled PP Granules

Granules were obtained from the recycling wastes studied at the temperature values specified in the previous section, and the MFI test results are given in Table 4. MFI tests are applied in accordance with ASTM D 1238-23 standard. Three tests are applied and the average result is used.
MfI

Table 4. MFI test results of recycled granules

Samples	Density (g/cm³)	MFI (g/10 min)	MVR (cm³/10 min)
Recycle-PP1	0, 82	23	49,30
Recycle-PP2	0,85	38	59,16
Recycle-PP3	0,84	47	75,89
Recycle-PP4	0,86	67	88,83
Recycle-PP5	0,86	85	130,39
Recycle-PP6	0,86	104	182,70

By using a polymer with a MFI of 1200 MFI, the molecular chains of the polymer exposed to heat treatment (chain length shortens) are broken. During the recycling of meltblown fabrics, i.e. granulation, polymers are again subjected to thermal degradation and the molecular chains of the polymer are broken more. Therefore, 100% meltblown fabrics (Recycle-PP7) could not be recycled and measurements could not be performed. Pictures of other samples are shown in Figure 2.
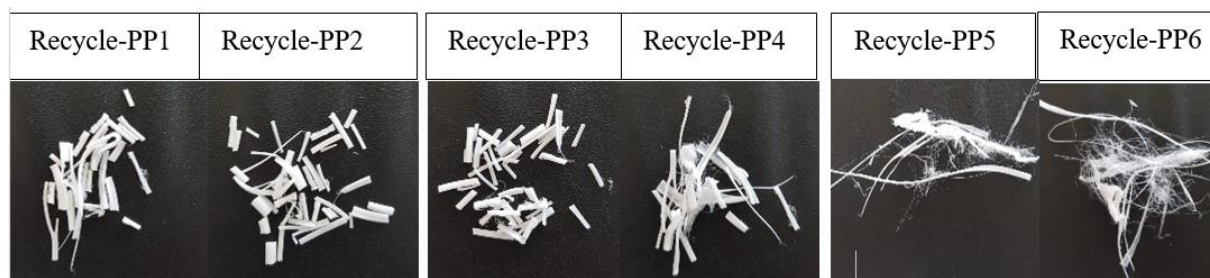
Figure 2. Recycled PP granule samples

As it is known, the density value of PP polymer is 0.91 g/cm^3 [11,18], but it was determined below this value in the measurements. The reason for this difference is that air is trapped inside the granules during granule formation. This undesirable situation is that the frequency of the filter used is not suitable. To solve this, it is recommended to choose a more densely woven lower mesh filter.

As it can be understood from the data, it is seen that the MFI value and naturally the fluidity increase as the amount of meltblown in the mixture content increases. This trend is broken in the Recycle-PP6 sample, because meltblown raw materials with high fluidity are fabrics and become too fluid to form when re-extruded.

Another detected situation is the correlation between the MFI values of the recycled granules produced from spunbond wastes obtained from 24 MFI and 38 MFI polymers. Granules from 24 MFI spunbond wastes are 23 MFI, while granules from 38 MFI spunbond wastes are 38 MFIs. It was observed that the MFI value did not change much with the recycling or extruding of the polymer with a high MFI value. This shows that the higher the MFI value of the PP polymer, the more difficult it is to recycle.

3.2. Determination of Strength Values of Produced Spunbond Fabrics

In this part of the study, spunbond fabric was produced by adding the granules obtained from 24 MFI waste and determined as 38 MFI in the original raw material at the specified rates (0, 3, 5, 10, 15, and 20%). Test results of mass and thickness values are given in Table 5.

Table 5. Mass and thickness values of spunbond fabrics

Sample codes	Granule Ratio (%)	Mass (g/m^2)	Thickness (mm)
Rec-PP1-G0	0%	13,2	0,13
Rec-PP1-G1	3%	12,9	0,15
Rec-PP1-G2	5%	12,8	0,17
Rec-PP1-G3	10%	13,1	0,14
Rec-PP1-G4	15%	12,7	0,15
Rec-PP1-G5	20%	13,3	0,16

The average weight values of the samples were found to be very close to each other with a standard deviation of 0.13%. This result shows how accurate the mold temperature settings, one of the process parameters produced in the spunbond machine, are. It should be noted that the most important observation is the absence of filament breaks that cause drip/melt defects in production. The low standard deviations of the weights of the recycled granule-added samples is another factor that indicates that the process parameters are chosen properly. A similar result can be seen when the mean thickness values and their standard deviation values are examined. The effect of the amount of granules added to the spunbond fabric on the fabric strength is shown in Figure 3.
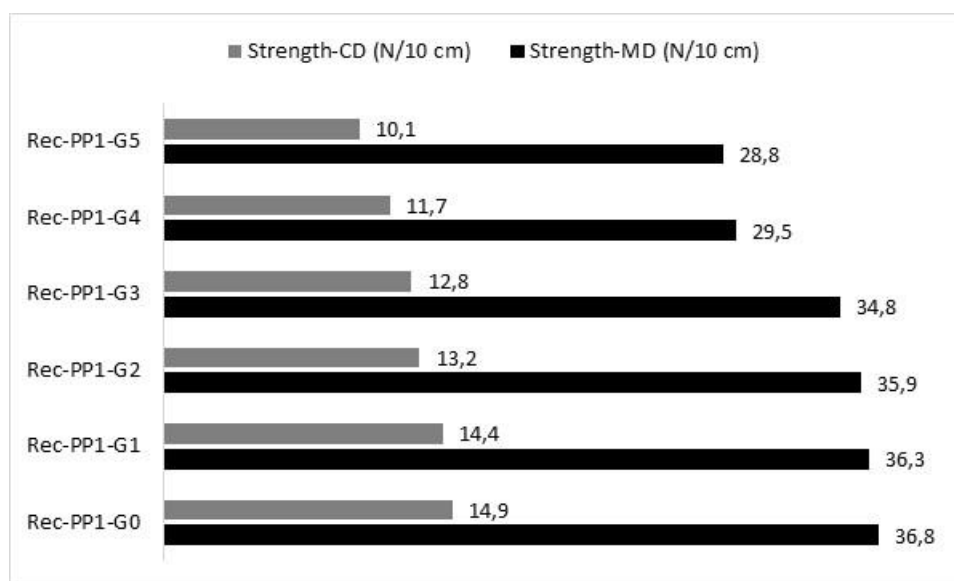
Figure 3. The effect of the increase in the number of granules on the strength of the fabrics

The strength values of spunbond fabrics gain importance according to the place of use of the fabric. Similarly, to give an example for the % elongation value; while the % elongation value is desired to be quite low in lamination processes, % elongation is desired to be quite high in Spunbond fabrics used in elastic nonwoven areas.

Both machine direction (MD) and fabric width (CD) strength values of recycled PP granule-added spunbond fabrics decreased with the increase in the number of granules. While the MD-strength value of spunbond (Rec-PP1-G0) fabric produced without using recycled granules was 36.8 N/10 cm, it was determined as 28.8 N/10 cm in 20% doped spunbond (Rec-PP-G5) fabric. The loss of strength value in the MD direction was determined as 21.7%. A similar situation occurred for the CD-strength value. The strength value loss in the CD direction is 32.2% compared to the MD direction. In this case, it is not recommended to use recycled granules in productions with high strength expectations from 13 g/m^2 spunbond fabrics. For example, it is recommended to use pure raw materials in building-construction textiles and geotextiles. In addition, in the hygiene-medical sector, pure raw materials should be used in accordance with the standards. However, it is understood that up to 10% of recycled PP can be added to fabrics produced for sectors where strength is not important. For example, there is no need for strength in products used as lining in the furniture industry. There is no need for strength in spunbond fabrics used as fruit protectors and fruit mats in fruit crates in the agriculture and greenhouse industry. The graph showing the change in the elongation values of spunbond fabrics with the amount of recycled PP granules is given in Figure 3.
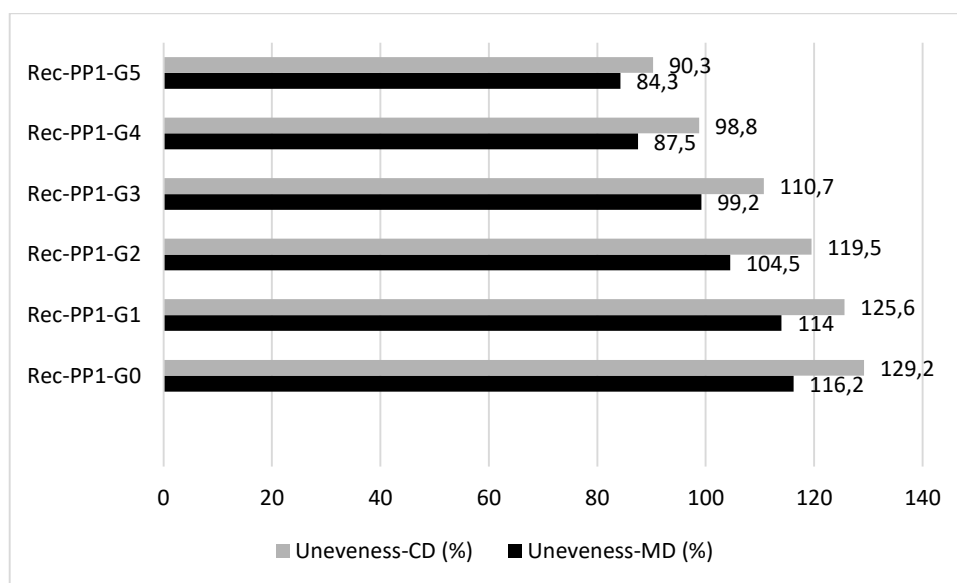
Figure 4. Elongation values of spunbond fabrics according to the number of granules

In Figure 4, the change in %-elongation values of spunbond fabrics obtained by doping recycled PP granules at determined rates was followed. As can be seen from the graph, the MD direction %-elongation value (U-MD) tends to decrease as the amount of added granules increases. The same is true for the U-CD value. A clear trend was not observed in the M-CD graph given in Figure 3. Due to the fact that the filament fan speed and belt suction fan speed values of the process parameters are adjusted in such a way that no breakage occurs in the filament, these settings may have been changed in a way that would affect the filament distribution of the fabric. As a result, low elongation value or keeping it constant at a certain value will facilitate processes such as lamination.

4. CONCLUSION

Polypropylene polymer has seen an extraordinary demand, especially with the Covid-19 pandemic, and manufacturers have not been able to meet this demand. The fact that there are not enough PP manufacturers in our country has created major problems in the supply of raw materials. The thermoplastic structure of PP polymer has enabled this experimental study to be used for the reuse of waste products made of PP polymer as raw materials.

First of all, the first step was to obtain recycled PP granules, which can be obtained by mixing spunbond and meltblown fabrics from nonwoven fabrics in certain proportions, and which will provide trouble-free use in production. As a result of the MFI measurements, the granules obtained from 100% spunbond fabric waste were added to the spunbond fabrics and the production phase was started.

The strength values of the fabrics obtained from recycled PP granules doped between 0 and 20% were investigated. As the doping ratio increased, the strength values in the machine (MD) direction and the fabric width (CD) direction decreased by 21.7%-32.2%, and the elongation value in the machine (MD) direction and fabric width (CD) direction decreased by 27.4%-30,1%. It was determined that there was a decrease of 30 percent. The reason why the amount of recycled PP granules cannot be fed more than 10% is the formation of defects in the fabric. These productions are long-term (8-hour) productions and there was no filament break during the production. However, in the trials of 20% or more (up to 25%), defective areas occurred in the fabric as a result of mold contamination or breaks during the maturation

of the filament. For this reason, it is not included in the comparison of strength values. However, this limitation may vary depending on the machine design, the purity of the raw material used, the lower and upper limits needed when setting the process parameters.

With the study, it has been shown that spunbond fabric wastes can be recycled and used at a rate of 10%. In future studies, the usability of recycled granules obtained by increasing the meltblown ratio in the meltblown line should be investigated.

From the perspective of environmental awareness, studies of this kind are highly significant. At the core of this importance lies sustainability, particularly considering that the proportion at which waste generated during production is reintegrated into the system as raw material is not fixed. This ratio can vary depending on the raw materials used by the company, the working conditions, the machinery chosen, and even the working methods of the operators. However, analyzing these values for the company in question and ensuring that the waste produced at the edges is re-granulated or transformed into fibers in opening machines and then recycled into rotor yarn or nonwoven surfaces is highly meaningful. This type of production process is referred to as a closed-loop system. Nevertheless, the data obtained from the company still indicates a waste rate of around 4% in the production line. Conducting LCA analyses on the production line to reduce the level of waste may be more beneficial than converting it back into granules or fibers.

CONFLICT OF INTEREST

The author stated that there are no conflicts of interest regarding the publication of this article.

CRediT AUTHOR STATEMENT

Züleyha DEĞİRMENCİ: Investigation, Writing - original draft, Visualization, Resources Supervision, Conceptualization

REFERENCES

[1]   Chua MH, Cheng W, Goh SS, Kong J, Li B, Lim JY, Mao L, Wang S, Xue K, Yang L, Ye E. Face masks in the new COVID-19 normal: materials, testing, and perspectives. Res, 2020, DOI: 10.34133/2020/7286735..

[2]   Shubhra QT, Alam AM, Quaiyyum MA. Mechanical properties of polypropylene composites: A review. J. Thermoplast. Compos. Mater,2013 Apr;26(3):362-91.

[3]   Gramsch S, Sarishvili A, Schmeißer A. Analysis of the fiber laydown quality in spunbond processes with simulation experiments evaluated by blocked neural networks. Adv Polym Tech, 2020(1):7648232.

[4]   Hosun L. A review of spun bond process. J. Text. Apparel, Technol. Manag, 2010;6(3):1-3.

[5]   Dönmez U, Kurt HA, Atıcı A. Effect of calender temperature and fabric layer number on fabric performance in combining nonwoven fabrics with calender method.. Gazı U. J. Scı Part C: Design and Technology, 2019;7(3):765-75.

[6]   Fedorova N. Investigation of the utility of islands-in-the-sea bicomponent fiber technology in the spunbond process [dissertation]. NC State University, Raleigh, 2006.

[7]   Nanjundappa R, Bhat GS. Effect of processing conditions on the structure and properties of polypropylene spunbond fabrics. J Appl Polym Scı, 2005 Dec 15;98(6):2355-64.

[8]   Geus HG. Developments in manufacturing techniques for technical nonwovens. In Advances in technical nonwovens, 2016 Jan 1 (pp. 133-153). Woodhead Publishing.

[9]   Bertin S, Robin JJ. Study and characterization of virgin and recycled LDPE/PP blends. Eur Polym J, 2002 Nov 1;38(11):2255-64.

[10]   Gregor-Svetec D, Tısler-korljan B, Leskovsek M, Sluga F. Monofilaments produced by blending virgin with recycled polypropylene. Text Appar, 2009 Jul 1;19(3):181-8.

[11]   Montagna LS, da Camargo Forte MM, Santana RM. Induced degradation of polypropylene with an organic pro-degradant additive. J Mater Scı Eng. A, 2013 Feb 1;3(2A):123.

[12]   Şengül Ü. and Şengül AB, "Evaluation of absorbent hygiene product waste in terms of potential and environmental economy in Turkey. In Internatıonal Congress Of Management Economy And Polıcy Proceedıngs Volume III (p. 2788)", ICOMEP 2016, 26-27 October, İstanbul, Turkey.

[13]   Ahmedzade P, Faınleıb A, Günay T, Grıgoryeva O, Usage of Recycled Postconsumer Polypropylene in Bituminous Binder. Tech J, 2016;27(3):7497-513.

[14]   Erem E, Gökkurt T. Investigation of the effects of nucleating agents, harmonizators and the antioxidants on recycled polypropylene, Adıyaman Üniversitesi Mühendislik Bilimleri Dergisi, 2021;8(14):1-22.

[15]   Öztürk O, Investigation of the Reusability of Recycled Polyethylene and Polypropylene Through Tensile Tests. Master's thesis, Pamukkale Üniversitesi Fen Bilimleri Enstitüsü, 2005

[16]   Strapasson R, Amico SC, Pereira MF, Sydenstricker TH. Tensile and impact behavior of polypropylene/low density polyethylene blends. Poly Test, 2005 Jun 1;24(4):468-73.

[17]   Şentürk B, Investigation of the Effect of Nucleating Additives on the Mechanical Behavior of Recycled Polypropylene. Doctoral dissertation, Institute of Applied Science, 2014

[18]   Aumnate C, Rudolph N, Sarmadi M. Recycling of polypropylene/polyethylene blends: Effect of chain structure on the crystallization behaviors. Polymers Basel, 2019 Sep 6;11(9):1456.

[19]   http://www.industrialextrusionmachinery.com/plastic_extrusion.html

[20]   Hopewell J, Dvorak R, Kosior E. Plastics recycling: challenges and opportunities. Philosophical Transactions of the Royal Society B: Biological Sciences, 2009 Jul 27;364(1526):2115-26.

[21]   Karayannidis GP, Achilias DS. Chemical recycling of poly (ethylene terephthalate). Macromol Mater Eng, 2007 Feb 2;292(2):128-46..

[22]   Achilias DS, Antonakou E, Roupakias C, Megalokonomos P, Lappas A. Recycling techniques of polyolefins from plastic wastes. Global Nest J, 2008 Mar 1;10(1):114-22.

[23]   Ragaert K, Delva L, Van Geem K. Mechanical and chemical recycling of solid plastic waste. Waste Manage, 2017 Nov 1;69:24-58.

RESEARCH ARTICLE

ADVANCED APPLICATIONS OF PHYSICS-INFORMED NEURAL NETWORKS (PINNS) IN R FOR SOLVING DIFFERENTIAL EQUATIONS

Melih AGRAZ [1, *]

[1] Department of Statisitcs, Giresun University, Giresun, Türkiye
melih.agraz@giresun.edu.tr, melihagraz@gmail.com- 🆔_0000-0002-6597-7627_

Abstract

Deep learning, a powerful machine learning technique leveraging artificial neural networks, excels in identifying complex patterns and relationships within data. Among its innovations is the emergence of Physics-Informed Neural Networks (PINNs), which have revolutionized the field of applied mathematics by enabling the solution and discovery of differential equations through neural networks. PINNs address two key challenges: data-driven solutions, where the model approximates the hidden solutions of differential equations with fixed parameters, and data-driven discovery, where the network learns parameters that best describe observed data. This study explores the implementation of PINNs within the R programming environment to solve two differential equations: one with boundary conditions $y' - y = 0$ with y(0)=0 and y(e)=1 boundaries and the Burgers' Equation. The research utilizes R libraries, including reticulate for Python integration and torch for neural network operations, to demonstrate the versatility and efficacy of PINNs in addressing both data-centric solutions and parameter discovery. The results showcase the ability of PINNs to handle complex, high-dimensional problems, offering a promising alternative to traditional numerical methods for solving differential equations.

1. INTRODUCTION

Differential equations, encompassing Ordinary Differential Equations (ODEs) and Partial Differential Equations (PDEs), serve as mathematical models for describing the dynamics of systems across various disciplines. Since Newton's *Principia*, these equations have been fundamental to understanding and explaining physical laws. The primary objective of differential equations is to derive solutions that adhere to governing mathematical expressions characterizing the phenomena under study. Consequently, devising efficient and accurate methods to solve these equations is critical for scientific advancement and engineering applications.

Deep Learning (DL), a branch of machine learning, employs artificial neural networks with multiple layers to tackle problems involving regression, pattern recognition, and classification. While traditionally DL has not been focused on solving differential equations, recent developments highlight its potential in this domain. The pioneering work by Lagaris et al. [1] laid the groundwork by employing artificial neural networks for boundary and initial value problems. Cheng et al. [2] extended this idea to Hamilton-Jacobi-Bellman equations. More recently, the advent of Physics-Informed Neural Networks (PINNs), introduced by Raissi et al. [3-5] under the mentorship of Karniadakis and colleagues, marked a significant breakthrough. PINNs utilize deep learning methodologies to address forward and inverse problems in PDEs, offering an innovative alternative to conventional solvers.

Several R packages exist for solving differential equations. For instance:

- The **deSolve** package (Soetaert et al. [6]) addresses initial boundary problems for ODEs and PDEs.
- The **ReacTran** package (Soetaert and Meysman [7]) focuses on reactive transport equations in 1D, 2D, or 3D domains.
- The **rootSolve** package (Soetaert [8]) employs the Newton-Raphson method to determine roots of nonlinear and linear equations.

In contrast, Python provides robust support for PINNs through libraries like PyTorch (Paszke et al. [9]) and TensorFlow (Abadi et al. [10]). However, the absence of an equivalent R package for PINNs presents a gap in the R ecosystem. This study addresses this limitation by demonstrating the implementation of the PINNs approach in R, paving the way for the development of a dedicated R package.

In this study, we first introduce the methodology of PINNs and provide a comprehensive overview of their workings. We then present two examples to illustrate how PINNs can be applied in R. These examples cover the definition of loss functions and parameter prediction, highlighting the effectiveness and versatility of this approach.

2. MATERIAL and METHODS

2.1. Overview of Physics-informed Neural Networks (PINNs)

Physics-Informed Neural Networks (PINNs) were initially proposed by Karniadakis, Raissi, and colleagues [3-5] as a neural network-based approach for solving partial differential equations (PDEs). A significant advancement in PINNs was the incorporation of a residual network, which represents a major innovation. This network incorporates the governing physical equations, utilizes the output of the deep learning model, and calculates the residual values, as highlighted by Markidis [11].

An equation that illustrates the general form of the partial differential equation addressed by Physics-Informed Neural Networks (PINNs) is as follows:

$$u_t + N\,[u; \lambda] = 0, x \in \Omega, t \in [0, \Omega], t \in [0, T]$$
$$u(0, x) = h(x), x \in \Omega \qquad (1)$$
$$u(t, x) = g(t, x), x \in \partial\Omega, t \in [0, T]$$

In this framework, *u* (that is, *u(t, x)*) denotes the unknown solution subject to boundary conditions *g(t, x)* and initial conditions *h(x)*; essentially, *u* is the target variable of interest (e.g., representing a wave). The derivative u_t denotes the partial derivative of *u* with respect to time *t* over the interval [0, T], while *x* is an independent spatial variable within the domain Ω. In other words, *x* and *t* are the given inputs (e.g., spatial location *x* and time *t*), and *N[u; λ]* is a linear or nonlinear differential operator characterized by a set of PDE parameters λ.

In solving the differential equation, the function *u* is approximated using a fully connected deep neural network, where *(t, x)* serve as inputs and $u_{NN}(t, x)$ as outputs. A deep neural network comprises multiple hidden layers, each of which has inputs (X = $[x_1, x_2,..., x_i]$) and outputs (Y = $[y_1, y_2, ..., y_i]$).

To simplify the equation, the left-hand side ($u_t + N\,[u; \lambda]$) can be expressed as *f(t, x),* that is,

$$f(t,x) := u_t + N[u; \lambda] \tag{2}$$

The artificial neural network is constructed using hidden layers, where the inputs and outputs of the layers are transmitted throughout the network according to the formula:

$$\sigma(w_{i,j} x_i + b_i), \tag{3}$$

where b_j and $w_{i,j}$ represent biases and weights, respectively. $\sigma(.)$ denotes the activation function, typically applied as a hyperbolic tangent activation function for each neuron except for the last layer, where no additional regularization is applied Cai et al. [12]. The parameters of the neural networks shared between u(t, x) and f(t, x) are learned by minimizing the loss function.

$$MSE = MSE_r + MSE_b + MSE_0, \tag{4}$$

where,

$$MSE_0 = \frac{1}{N_0} \sum_{i=1}^{N_0} |u(t^i, x^i) - h^i|^2 , \tag{5}$$

and

$$MSE_b = \frac{1}{N_b} \sum_{i=1}^{N_b} |u(t^i, x^i) - g^i|^2 , \tag{6}$$

and

$$MSE_r = \frac{1}{N_r} \sum_{i=0}^{N_r} |u_t(t^i, x^i) + N_x u(t^i, x^i)|^2 . \tag{7}$$

Here in Equations 4-7, MSE_0, MSE_b , and MSE_r correspond to the losses associated with initial conditions, boundary conditions, and the penalization of residuals in the governing equations, respectively. To compute the residuals for MSE_r, it is necessary to obtain the derivatives of the outcomes—namely, u_t and $N_x u$ with respect to the inputs. These derivatives are calculated using automatic differentiation, as described by Baydin et al. [13]. The overall loss function is then optimized using an algorithm such as stochastic gradient descent (Ruder [31]) or the ADAM optimizer (Kingma and Ba [14]), among others.

An illustration of the PINNs approach is provided in Figure 1 below. As depicted in Figure 1, a fully-connected deep feed-forward neural network is utilized to approximate *u(t, x)*. This approximation is subsequently utilized to formulate the initial conditions loss MSE_0, the boundary conditions loss MSE_b, and residual loss MSE_r.
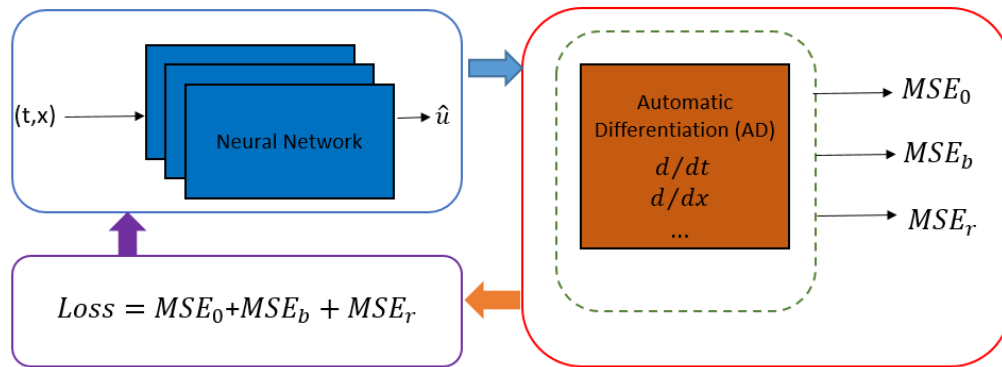
Figure 1. Physics-Informed Neural Networks (PINNs) Workflow [32].

Since their introduction, Physics-Informed Neural Networks (PINNs) contributed a significant impact on fluid mechanics and scientific computing, leading to notable advancements. Karniadakis and his collaborators have built upon these methodologies, resulting in various extensions of PINNs. These extensions include stochastic PINNs (Zhang et al. [15]), fractional PINNs (fPINNs) (Pang et al. [16]), conservative physics-informed neural networks (CPINNs) (Jagtap et al. [17]), parareal physics-informed neural networks (PPINNs) (Meng et al. [18]), extended physics-informed neural networks (XPINNs) (Jagtap and Karniadakis [19]), non-local PINNs (nPINNs) (Pang et al. [20]), PINNs with a variational formulation based on the Galerkin method (hp-VPINN) (Kharazmi et al. [21]), parallel PINNs (Shukla et al. [22]), Bayesian PINNs (Yang et al. [23]), and approaches for learning nonlinear operators via DeepONet (Lu et al. [24]). Agraz et al. [32] showed that simple differential equations can be effectively solved using a single multiplicative neuron.

PINNs can address two distinct problems: data-driven solutions for PDEs and data-driven discovery. In the first scenario, the model parameter λ remains constant, and PINNs approximate the hidden solution. In the latter scenario, PINNs are employed to identify the λ parameter that best characterizes the observed data [3, 25]. This article presents examples and definitions of both solution types, focusing on two different problems to illustrate the approach's efficacy. First, we begin by showcasing the solution to the differential equation $y' - y = 0$ with the initial conditions $y(0) = 1$ and $y(1) = e$. This is achieved through the utilization of the PINNs methodology, complemented by the incorporation of the reticulate package for data-centric solutions. Second, we tackle the one-dimensional Burgers' equation Basdevant et al. [26] using PINNs, employing the torch package Falbel and Luraschi [29] to exemplify a data-driven discovery scenario. The Burgers' equation is a fundamental partial differential equation that stems from the Navier-Stokes equations Raissi et al. [5]. Within this section, we embark on elucidating the foundational aspects of PINNs within the context of the R community. We commence this exploration with a clear-cut example centered around a simple differential equation. To facilitate a comprehensive understanding, the complete code for this illustrative instance is available in Supplementary A.1 on GitHub. Subsequently, we employ the torch package to tackle the one-dimensional Burgers' Equation as put forth by Basdevant et al. [26], leveraging the prowess of the PINNs approach to unveil insights driven by data. For interested readers, the comprehensive code pertaining to this particular example can be found in Supplementary A.2 on GitHub.

2. RESULTS

Data-Driven Solution of the $y' - y = 0$

To provide a straightforward introduction to the concept of PINNs, we offer an example that illustrates how to implement the PINNs approach for solving differential equations from the ground up using R

4.1.3. We begin by outlining a motivating example of a differential equation and its associated initial conditions, as defined in Equation8.

$$y' - y = 0, y(0) = 1, y(1) = e \qquad (8)$$

We initiate by installing and loading the pertinent packages and creating a Python virtual environment named "r-reticulate." The reticulate package Ushey et al. [27] facilitates the interaction between Python and R, enabling the utilization of required Python libraries within R. Additionally, we employ the TensorFlow library Abadi et al.[10], a well-known open-source machine learning framework, to address neural network and deep learning challenges. The complete code for the solution of $y' - y = 0$ is provided in Supplementary A.1.

```
#install_tensorflow(version = "1.15.0")
library(reticulate)
library(tensorflow)
library(ggplot2)
use_condaenv('r-reticulate')
```

We initiate by outlining the structure of the neural network along with its input and output specifications. Throughout all the experiments, we employ a 6-layer neural network, each layer comprising 50 neurons.

```
tf$set_random_seed(1234)
layers <- c(1, rep(50, 5), 1) #number of layers and neurons
N_residual <- 100  #number of residuals
N_test <- 80  #length of test data
x_f <- seq(0, 1, length.out=N_residual)
x <- c(0, 1) #inputs
y <- c(1, exp(1)) # outputs
x_train <- matrix(x, nrow = 2, ncol = 1)
y_train <- matrix(y, nrow = 2, ncol = 1)
x_f_train <- matrix(x_f, nrow = length(x_f), ncol=1)
```

Subsequently, we generate weights and biases following the truncated normal distribution utilizing a Xavier initializer, referred to as the xavier_initialization function. Following this, we proceed to create a fully-connected simple deep feed-forward artificial neural network, constituting the core structure of the PINNs methodology. In this context, the hyperbolic tangent (tanh) activation function is applied in each layer, excluding the final layer.

Following the neural network's construction, we proceed to define f(t, x)

$$f := y' - y, \qquad (9)$$

and we can now approximate the *u(t, x)* with a deep feed-forward artificial neural network. Accordingly, we define the *u(t, x)* function below,

```
u(t,x) <- function(x_){
 u <- neural_network(x_, weights, biases)
return(u)
}
```

Thereby, *f(t, x),* PINNs can be determined as,

```
f(t,x) <- function(x_){
y_ <- u_xt(x_)
y_x <- tf$gradients(y_, x_)[[1]]
# Residuals
f <- y_x - y_
return(f)
}
```

$$MSE = MSE_r + MSE_b, \qquad (10)$$

and the loss function is optimized by an Adam optimizer with the following codes.

```
loss_bd <- tf$reduce_mean(tf$square(y_pred - y_train))
residual_loss <- tf$reduce_mean(tf$square(f_pred))
Adam_optim <- tf$compat$v1$train$AdamOptimizer(1e-3)
Adam_opt_train <- Adam_optim$minimize(loss_bd+residual_loss)
```

After training for 10000 epochs, the loss functions are calculated and depicted in Figure 2 as separate plots.
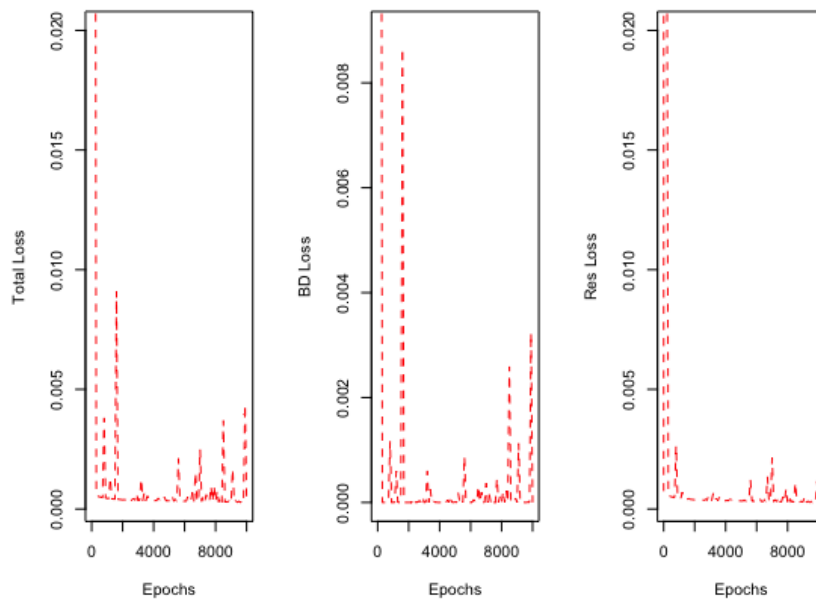
Figure 2. Total, Boundry (BD) and Residual Loss of the solution of y ′ − y = 0 with PINNs.

According to Figure 2, the Total Loss, Boundary Loss, and Residual Loss are approximately 0.00035, 0.000037, and 0.00031, respectively.

Post-training, we create a plot that showcases both the actual and estimated solutions on the test data. This comparison is made against the exact solution of the test data using the ggplot2 package Wickham and Chang]28[, as illustrated in Figure 3.
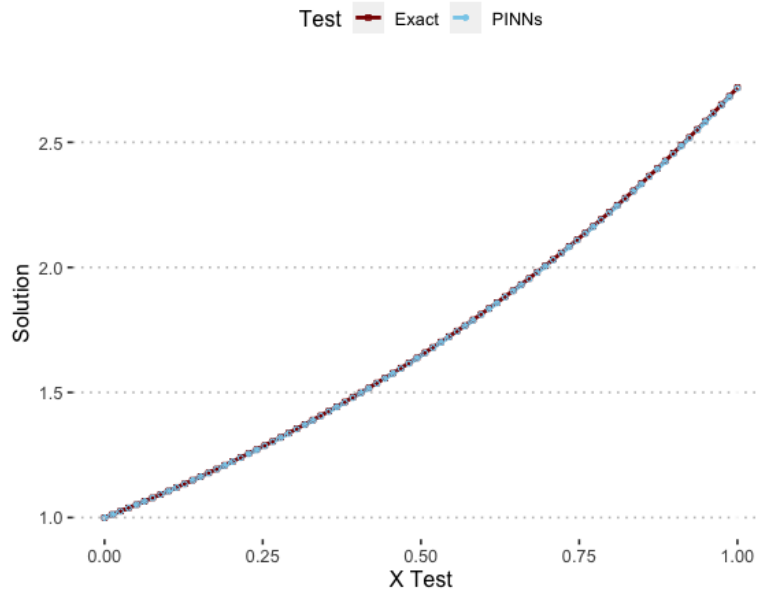
Figure 3. Comparison of predictions of test data and the exact solution.

According to Figure 3, the PINNs predicted solution accurately approximates the real solution. In conclusion, the mean squared error loss is computed from the test data and depicted in Figure 4.
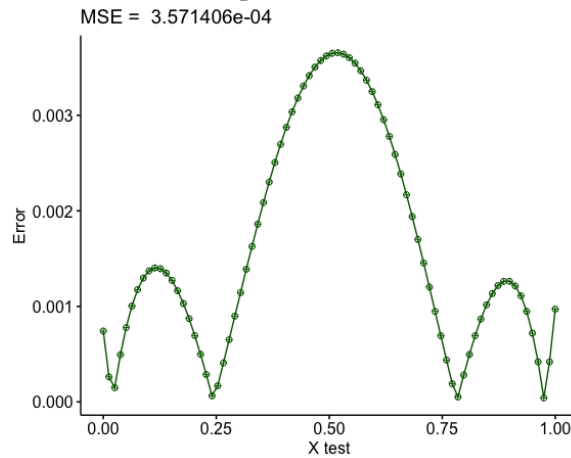
Figure 4. Mean squared error of the test data

Data-Driven Discovery of the Burgers' Equation

In this section, we tackle the one-dimensional Burgers' equation Basdevant et al. [26] using PINNs, employing the torch package Falbel and Luraschi [29] to exemplify a data-driven discovery scenario. The Burgers' equation is a fundamental partial differential equation that stems from the Navier-Stokes equations Raissi et al. [5].

Here, we demonstrate Burgers' equation first for solving forward problems using PINNs.

$$u_t + \lambda_1 u u_x - \lambda_2 u_{xx} = 0, x \in [-1,1], t \in [0,1] \tag{11}$$

We can define *f(t, x)* as,

$$f := u_t + \lambda_1 u u_x - \lambda_2 u_{xx} \tag{12}$$

in which the deep feed-forward neural network approximates *u(t, x)*, and the PINNs *f(t, x)* emerges as a consequence.

We begin by installing and loading the necessary packages. The torch package is an essential open-source machine learning package developed based on PyTorch Paszke et al. [9]. All the codes for solving the Burgers' equation can be found in Supplementary A.2 on GitHub.

```
library(R.matlab)  # reading .mat data
library(pracma)
library(torch)
library(akima)
```

We start by loading the data.

```
# Load data
data_burger <- readMat("data_burgers_shock.mat")
t <- as.vector(data_burger$t)
x <- as.vector(data_burger$x)
Exact <- t(data_burger$usol)
grid <- meshgrid(x, t)
X <- grid$X T <- grid$Y
```

The Burgers' data comprises information labeled as *t, x*, and *usol* in list form. We initiate by outlining the structure of the neural network along with its input and output specifications. Throughout all experiments, we employ a 9-layer neural network, each layer comprising 20 neurons.

```
torch_manual_seed(1234)
nu <- 0.01 / pi N_u <- 2000
layers <- c(2, 20, 20, 20, 20, 20, 20, 20, 20, 1)
X_star <- torch_stack(c(torch_flatten(torch_tensor(X)), +
torch_flatten(torch_tensor(T))))$t()
u_star <- torch_flatten(torch_tensor(Exact))$unsqueeze(1)$t()
# Domain boundries
lb <- apply(X_star, 2, min)
ub <- apply(X_star, 2, max)
X_u_train <- X_star[id_x,]
u_train <- u_star[id_x]
u_train <- u_train + noise * torch_std(u_train) *
+ torch_randn(dim(u_train))
```

We create a training dataset containing 2000 randomly generated observations corresponding to both $\lambda = 1.0$ and $\lambda = 0.01/\pi$. This is done to illustrate the effectiveness of the PINNs approach. The positions of the generated training points are depicted in Figure 5(d). Following this, we update the weights and biases utilizing a simple feed-forward deep neural network structure and the LBFGS optimizer Liu and Nocedal [30], aiming to minimize the loss function. After the training process, the PINNs approach estimates both the *u(t, x)* solution of the PDEs and the parameters $\lambda = (\lambda_1, \lambda_2)$ that characterize the underlying dynamics. The predictive accuracy of the PINNs approach is demonstrated in Figure 5(a-c),

while the comparison between the exact and predictive outcomes for noisy and noiseless data is presented in Table 1.

Table 1. Unequivocally indicates that the PINNs approach adeptly predicts the parameters. Notably, even with 1

(a)   (b)   (c)

(d)
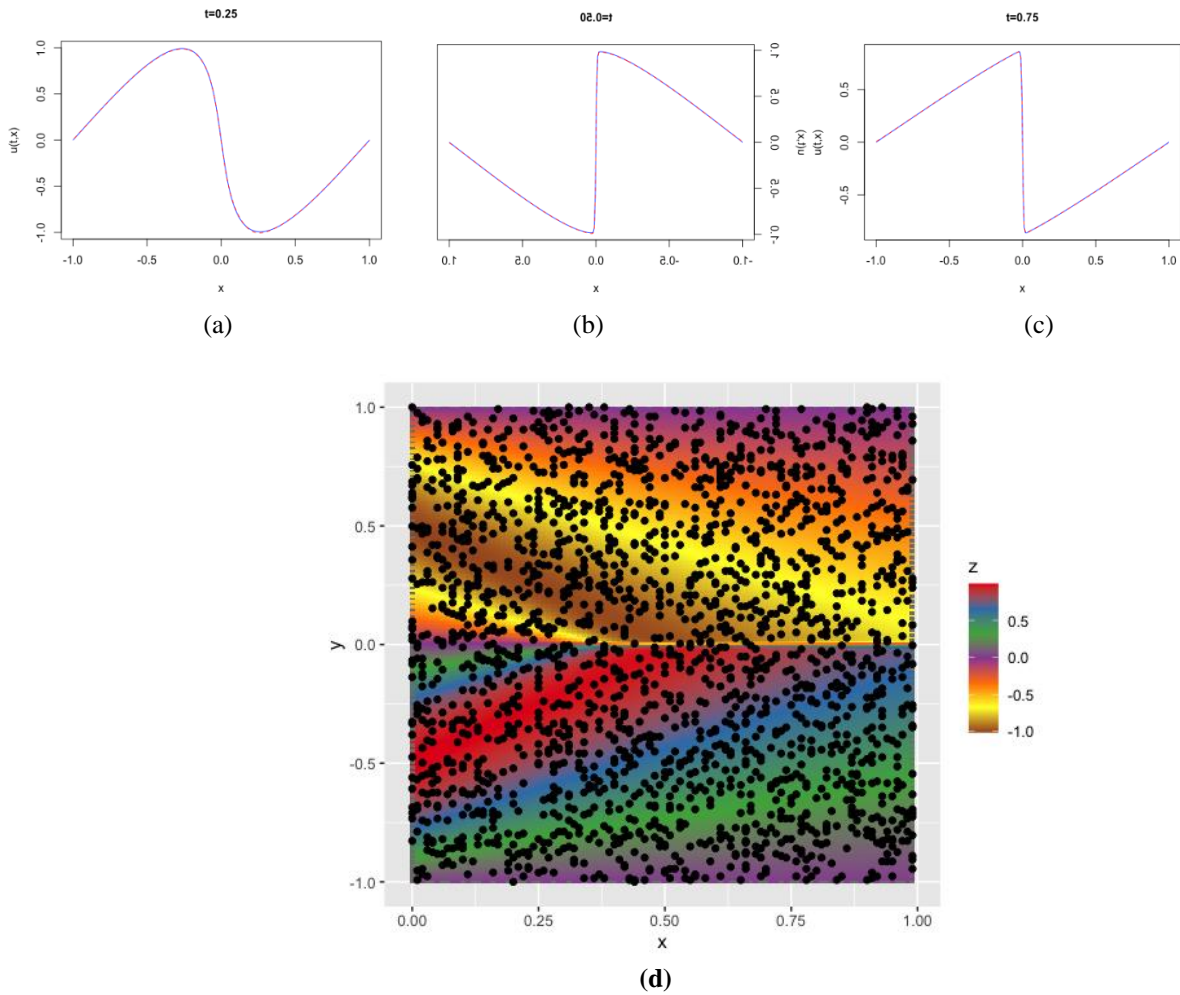
Figure 5: Burgers' equation: Exact and predicted solutions comparisons for (a) t = 0.25 (b) t = 0.50 (c) t = 0.75 and (d) predictions are given by a physics neural network of *u(t, x)* with the training data

Table 1. Correct and predicted parameters of Burgers' equation

Correct PDEs	$u_t + uu_x - 0.0031831u_{xx} = 0$
Identified PDEs (clean data)	$u_t + 0.995469uu_x - 0.0033095u_{xx} = 0$
Identified PDEs (%1 noise)	$u_t + 1.000711uu_x - 0.0031104u_{xx} = 0$

3. CONCLUSION

PINNs were first introduced by Karniadakis and his team Raissi et al. [3-5] as an innovative alternative to numerical solutions for PDEs. PINNs utilize a simple deep feed-forward neural network approach and employ automatic differentiation techniques Baydin et al. [13] to effectively address PDEs.

In this study, we have demonstrated how to apply the PINNs approach within the R programming language, leveraging the reticulate and torch packages. As far as our current knowledge extends, this study stands as the inaugural implementation of PINNs in the R programming language. Initially, we showcased the solution of a basic differential equation problem, specifically $y' - y = 0$ with conditions $y(0) = 1$ and $y(1) = e$, employing the reticulate package. We also plotted the total error, boundary error, and residual error, while additionally comparing the exact solution with predictions in a graphical representation. Our observation confirmed that the PINNs method adeptly predicts the exact solution. Finally, we calculated the MSE for the test data, resulting in an MSE of $3.571406 \times 10-4$.

Subsequently, we presented a practical approach for addressing Burgers' equation using PINNs through the PyTorch package. In this example, we contrasted the exact parameters with the predicted parameters of Burgers' equation, considering both noisy and noiseless data. Our exploration of Burgers' equation affirmed the PINNs approach's capacity to accurately estimate PDE parameters. Furthermore, we designed interactive solutions for PINNs via the shiny app and the torch package, which can be accessed on the GitHub page under shiny.R.

To the best of our knowledge, this article constitutes the pioneering effort in implementing the PINNs approach within the R programming language. In our future endeavors, we aspire to adapt additional implementations of the PINNs approach to R and develop a dedicated R package for this purpose.

ACKNOWLEDGEMENTS

CONFLICT OF INTEREST

The author stated that there are no conflicts of interest regarding the publication of this article.

CRediT AUTHOR STATEMENT

Melih Ağraz: Formal analysis, Writing - original draft, Visualization, Investigation, Supervision, Conceptualization.

REFERENCES

[1]   Lagaris I, Likas A, Fotiadis D. Artificial neural networks for solving ordinary and partial differential equations. IEEE Transactions on Neural Networks, 1998; 9(5): 987–1000. doi: 10.1109/72.712178.

[2]   Cheng T, Lewis FL, Abu-Khalaf M. A neural network solution for fixed-final time optimal control of nonlinear systems. Automatica, 2007; 43(3): 482–490. doi: https://doi.org/10.1016/j.automatica.2006.09.021. URL https://www.sciencedirect.com/science/article/pii/S0005109806004250.

[3]   Raissi M, Perdikaris P, Karniadaksi GM. Physics-informed neural networks: A deep learning framework for solving forward and inverse problems involving nonlinear partial differential equations. Journal of Computational Physics, 2019; pages 686–707.

[4]   Raissi M, Perdikaris P, Karniadaksi GM. Physics informed deep learning (part i): Data-driven solutions of nonlinear partial differential equations. arXiv preprint. arXiv:1711.10561. 2017a.

[5]   Raissi M, Perdikaris P, Karniadaksi GM. Physics informed deep learning (part ii): Data-driven discovery of nonlinear partial differential equations. arXiv preprint. preprint arXiv:1711.10566. 2017b.

[6]   Soetaert K, Petzoldt T, Setzer RW. Solving differential equations in R: Package deSolve. Journal of Statistical Software, 2010; 33(9): 1–25. doi: 10.18637/jss.v033.i09.

[7]   Soetaert K, Meysman F. R-package reactran : Reactive transport modelling in r. 2010.

[8]   Soetaert K. rootSolve: Nonlinear root finding, equilibrium and steady-state analysis of ordinary differential equations. R package 1.6. 2009.

[9]   Paszke A, Gross S, Massa F, Lerer A, Bradbury J, Chanan G, et al. Pytorch: An imperative style, high-performance deep learning library. In: Wallach H, Larochelle H, Beygelzimer A, d'Alché-Buc F, Fox E, Garnett R, editors. Advances in Neural Information Processing Systems 32. Curran Associates, Inc.; 2019. pages 8024–8035.

[10]   Abadi M, Agarwal A, Barham P, Brevdo E, Chen Z, Citro C, et al. TensorFlow: Large-scale machine learning on heterogeneous systems, 2015. URL https://www.tensorflow.org/. Software available from tensorflow.org.

[11]   Markidis S. The old and the new: Can physics-informed deep-learning replace traditional linear solvers? Frontiers in big Data, 2021; 4: 669097.

[12]   Cai S, Wang Z, Wang S, Perdikaris P, Karniadakis G. Physics-informed neural networks (pinns) for heat transfer problems. Journal of Heat Transfer, 2021; 143. doi: 10.1115/1.4050542.

[13]   Baydin A, Pearlmutter B, Radul A, Siskind J. Automatic differentiation in machine learning: A survey. Journal of Machine Learning Research, 2018; 18: 1–43.

[14]   Kingma D, Ba J. Adam: A method for stochastic optimization. International Conference on Learning Representations, 2014.

[15]   Zhang D, Lu L, Guo L, Karniadakis G. Quantifying total uncertainty in physics-informed neural networks for solving forward and inverse stochastic problems. Journal of Computational Physics, 2019; 397. doi: 10.1016/j.jcp.2019.07.048.

[16]   Pang G, Lu L, Karniadakis G. fpinns: Fractional physics-informed neural networks. SIAM Journal on Scientific Computing, 2019; 41: A2603–A2626. doi: 10.1137/18M1229845.

[17]   Jagtap A, Kharazmi E, Karniadakis G. Conservative physics-informed neural networks on discrete domains for conservation laws: Applications to forward and inverse problems. Computer Methods in Applied Mechanics and Engineering, 2020; 365: 113028. doi: 10.1016/j.cma.2020.113028.

[18] Meng X, Li Z, Zhang D, Karniadakis G. Ppinn: Parareal physics-informed neural network for time-dependent pdes. Computer Methods in Applied Mechanics and Engineering, 2020; 370: 113250. doi: 10.1016/j.cma.2020.113250.

[19] Jagtap A, Karniadakis G. Extended physics-informed neural networks (xpinns): A generalized space-time domain decomposition based deep learning framework for nonlinear partial differential equations. Communications in Computational Physics, 2020; 28: 2002–2041. doi: 10.4208/cicp.OA2020-0164.

[20] Pang G, D'Elia M, Parks M, Karniadakis G. npinns: Nonlocal physics-informed neural networks for a parametrized nonlocal universal laplacian operator. algorithms and applications. Journal of Computational Physics, 2020; 422: 109760. doi: 10.1016/j.jcp.2020.109760.

[21] Kharazmi E, Zhang Z, Karniadakis GE. hp-vpinns: Variational physics-informed neural networks with domain decomposition. Computer Methods in Applied Mechanics and Engineering, 2021; 374.

[22] Shukla K, Jagtap AD, Karniadakis GE. Parallel physics-informed neural networks via domain decomposition. Journal of Computational Physics, 2021; 447: 110683.

[23] Yang L, Meng X, Karniadakis GE. B-pinns: Bayesian physics-informed neural networks for forward and inverse pde problems with noisy data. Journal of Computational Physics, 2021; 425: 109913.

[24] Lu L, Jin P, Pang G, Zang H, Karniadakis G. Learning nonlinear operators via deeponet based on the universal approximation theorem of operators. Nature Machine Intelligence, 2021; 3: 218–229. doi: 10.1038/s42256-021-00302-5.

[25] Raissi M, Karniadakis GE. Hidden physics models: Machine learning of nonlinear partial differential equations. Journal of Computational Physics, 2018; 357: 125–141.

[26] Basdevant C, Deville M, Haldenwang P, Lacroix J, Ouazzani J, Peyret R, et al. Spectral and finite difference solutions of the burgers equation. Computational Fluid Dynamics. 1986; pages 23–41.

[27] Ushey K, Allaire J, Tang Y. reticulate: Interface to 'Python', 2022. URL https://rstudio.github.io/reticulate/, https://github.com/rstudio/reticulate.

[28] Wickham H, Chang W. Ggplot2: Create Elegant Data Visualisations Using the Grammar of Graphics, 2016. URL URLhttps://CRAN.R-project.org/package=ggplot2.

[29] Falbel D, Luraschi J. torch: Tensors and Neural Networks with 'GPU' Acceleration, 2022. URL https://torch.mlverse.org/docs,https://github.com/mlverse/torch.

[30] Liu DC, Nocedal J. On the limited memory bfgs method for large scale optimization. Mathematical Programming, 1989; 45: 503–528.

[31] Ruder S. An overview of gradient descent optimization algorithms. arXiv preprint arXiv:1609.04747. 2016.

[32] Agraz, M. Evaluating single multiplicative neuron models in physics-informed neural networks for differential equations. Scientific Reports, 2024, 14(1), 19073.

RESEARCH ARTICLE

PREDICTION OF NO$_x$ AND FUEL FLOW OF COMMERCIAL HIGH BYPASS AIRCRAFT ENGINES BASED ON CSA-SVR MODEL

Rıdvan ORUÇ [1, *]

[1] Department of Transportation Services, Civil Aviation Vocational School, Agri Ibrahim Cecen University, Agri, Türkiye
rdvan0465@gmail.com   0000-0002-9856-2989

Abstract	Keywords
Due to the negative effects of emissions caused by fossil fuels used by aircraft engines on the environment and human health, and the fact that fuel consumption is a high cost input for airlines, the aviation community has many studies on both issues. In order to overcome these problems, much space has been devoted to modeling, prediction and optimization studies on emissions and fuel consumption in the literature. Within the scope of this study, a model was created to predict the NOx emission values and fuel flow of high by-pass turbofan engines, which are also used in today's commercial air transportation. 165 different turbofan data taken from the International Civil Aviation Organization (ICAO) emission databank were used for modeling, and the specified parameters were modeled according to the by-pass ratio (BPR), overall pressure ratio (OPR) and rated thrust input parameters. In this context, the Cuckoo search algorithm-support vector regression (CSA-SVR) method for the Landing and Take-off (LTO) cycle, which includes the idle, take-off (T/O), climb out (C/O) and approach (App) phases, was used for the first time in the literature for the above-mentioned purpose. As a result of the error analysis methods, the minimum R^2 value for 4 phases in FF estimation was found to be 0.972763. This value for NO$_x$ was 0.6745 in the idle phase. However, the fact that this value was found to be 0.861497, 0.884984 and 0.792779 for T/O, C/O and App, respectively, shows the success of the model in estimating actual data.	

1. INTRODUCTION

Although situations such as the continuous development of technology, industrialization and the constant increase in transportation networks are important developments for humanity, they also bring certain problems. One of these problems is air pollution. It should not be forgotten that this situation, which has a negative impact on the environment and human health, may also be caused by natural factors (volcanic factors, wild fire, etc.) in addition to the anthropogenic factors mentioned above. Transportation, one of the anthropogenic factors, has a significant share in air pollution. Emissions resulting from air, land, sea and rail transportation are also partially responsible for climate change, stratospheric ozone depletion and acid deposition [1,3].

The speed that aviation provides to its customers, especially in international transportation, compared to other types of transportation, causes its rapid growth. As a matter of fact, research predicts that despite the negative effects of Covid-19, air transportation will grow between 3.6% and 3.8% on an annual basis between 2019 and 2041 [4,5]. Increasing air traffic will also increase total fuel consumption and fuel-related emissions. In order to overcome the mentioned problems, aircraft/engine manufacturers are trying to produce more efficient aircraft/engines, relevant authorities are developing different

procedures and methods to make aircraft stay in the air and on the ground shorter, and also; they have brought solutions such as turning to alternative fuels (Hydrogen) [6–10].

Research shows that aircraft engines account for approximately 2% of global greenhouse gas emissions due to the fossil fuel they use. However, with increasing air traffic, this value is estimated to be around 3% in 2050. Among transportation modes, approximately 10% of global greenhouse gas emissions originate from aircraft engines. In this context, being able to use fuel efficiently and reduce emissions is very important for economic and environmental sustainability [11,12]. Namely; According to International Air Transport Association (IATA) data, fuel costs (271 billion USD) constituted a very large percentage of airline operating costs, approximately 32%, in 2023 [13].

Emissions caused by aircraft engines spread to the environment within and above the troposphere layer of the atmosphere. These are nitrogen oxides (NO_x), carbon dioxide (CO_2), various sulfur oxides (SO_x), water vapor (H_2O), carbon monoxide (CO), various non-methane hydrocarbons (NMHC), other gases and particles [1, 14]. Within the scope of this study, NO_x-related estimation was made. Aviation NO_x emissions have adverse effects on local air quality and human health. NO_x emissions change the levels of methane (CH_4) and atmospheric ozone (O_3), two important greenhouse gases, and thus also affect the climate [15]. In addition, the impact of aviation among all anthropogenic sources in NO_x production is approximately 3% [1]. In this regard, considering the future development of aviation, studies on NO_x are important.

Due to the importance of reducing emissions, there are many studies in the literature on emission estimation, modeling and optimization for different aircraft engines in aviation. Metaheuristic methods are frequently used for this purpose. The basis for this lies in the success of these methods in challenging modeling and optimization problems in many different fields. Modeling work for 51 different mixed-flow turbofan engines can be given as an example of the mentioned studies. A multiple regression model was created for the engines specified within the scope of the study. Afterwards, it was aimed to increase the model accuracy by using the simulated annealing and genetic algorithms (GA) methods. The data used are data published by the International Civil Aviation Organization (ICAO). Model input values are by-pass ratio (BPR), overall pressure ratio (OPR) and fuel flow (FF), which have significant effects on engine performance. Using the 3 specified input values, rated thrust, different exergetic parameters and NO_x emission index (EI) values were predicted. As a result of the analysis, the coefficient of determination (R^2) value was found to be approximately 0.862 for NO_x EI [16]. In another study on the subject, certain exergy parameters were calculated for the take-off phase. Additionally, models estimating emission values and calculated exergy parameters were created. SVR and long short-term memory (LSTM) methods were used to model 171 different high BPR turbofan engines. In the study where FF was also modeled for the take-off phase, HC, NO_x and CO EI parameters were estimated. ICAO data was used for modeling and model input values were determined as rated thrust, BPR, OPR and combustion type. The study stands out as the first study on modeling the emission index and exergetic environmental parameters of high-bypass turbofan engines using the specified methods. The fact that the R^2 values of the models are very close to 1 shows the accuracy of the study [17]. Apart from emissions, there are also many studies on fuel consumption modeling alone. The basis for this lies in the fact that fuel consumption has a significant share in the operating expenses of airlines and is the main source of emissions. Trani et al. (2004) created an aircraft fuel consumption model using the Fokker F-100 aircraft performance manual and the artificial neural network (ANN) method [18]. Other studies on the subject were conducted by Baklacioglu (2015) and Baklacioglu (2016). In his first study, the author created a fuel flow rate model for commercial aircraft for the climbing flight profile using the GA method. True airspeed (TAS) and altitude were used as input values [19]. In the other study, a model was created for the B737-800 aircraft by using ANN and GA methods together. The goal is to create a model that predicts actual data for climb, cruise and descent based on TAS and altitude inputs [6]. Moreover, Ridvan and Baklacioglu conducted two different studies on climb and descent flight profiles, respectively, using CSA and particle swarm optimization (PSO) method. The data set used in the study

is flight data recorder (FDR) data of B737-800, one of the most used aircraft in medium-haul commercial air transportation. TAS and altitude, which directly affect flight performance and therefore fuel consumption, were used as model input values. Actual data were predicted with high accuracy in both fuel flow rate models [20, 21].

As a result of the literature research, to the author's knowledge, there is no study using the CSA-SVR method on NO_x emissions and fuel flow for the landing and take-off (LTO) cycle of turbofan engines with high BPR. This study stands out in this context as it is the first in this field. BPR, rated thrust and OPR, which have a significant impact on engine performance, were used as model input values. The created model predicts FF and NO_x with high accuracy according to the input values specified for the LTO cycle, which includes the idle, take-off, climb out and approach phases. In the study, data sets taken from the ICAO emission databank for 165 different high-bypass turbofan engines were used [22]. Although the input parameters and number of engines used are high, the prediction success is quite high, which shows the accuracy of the study. The fact that the engines are used in today's commercial air transportation shows the up-to-dateness of the study; Moreover, modeling for 4 different phases is important for the breadth of the scope.

2. CUCKOO SEARCH ALGORTIHM

Although CSA is a relatively new algorithm, it is frequently used in many areas. The most important reasons for this are that changing the parameters in the algorithm does not have much effect on the solution quality, CSA explores the search space more efficiently by using Lévy flights instead of standard random walks, and the risk of getting stuck in local minima is low. Research shows that the performance of the CSA method is better than GA and PSO, two of the most used metaheuristic methods. The main inspiration for the algorithm is brood parasitism, which is the reproductive strategy of some cuckoo species. CSA is built on 3 basic rules given below [20, 23, 24].

- Each cuckoo lays one egg in a randomly selected nest at one time.
- The best nests with high-quality eggs will be passed on to future generations.
- In CSA, the number of nests is fixed and the egg laid will be found by the host bird with a probability between 0 and 1. If the host bird notices the cuckoo egg, it will either get rid of it or leave its current nest to build a new nest [20,25].

CSA uses a combination of local and global random walk. The extent to which the algorithm's global and local search capabilities will be used is determined by the switching factor (p_a). Local random walk is shown in equation 1.

$$x_i^{t+1} = x_i^t + \alpha s \otimes H(p_a - \in) \otimes (x_j^t - x_k^t)$$

(1)

where x_i^t is the current solution and x_i^{t+1} indicates the new solution. From the other terms s and α are step size and step size scaling factor, respectively. While H(u) denotes the heaviside function, x_j^t and x_k^t are two randomly selected different solutions. Finally, $\in$ refers to a random number drawn from a uniform distribution, while the symbol $\otimes$ is the entry-wise product. The global random walk is specified in the equations below.

$$x_i^{t+1} = x_i^t + \alpha L(s, \lambda),$$

(2)

and

$$L(s, \lambda) = \frac{\lambda \Gamma(\lambda) sin(\pi\lambda / 2)}{\pi} \frac{1}{s^{1+\lambda}} ,(s >> s_0 > 0)$$

(3)

The global random walk uses Lévy flights. Therefore, λ is the Lévy flight parameter and the function Γ is a constant given for λ. One of the other terms, αL(s, λ) is the transition probability [20,23,25–27].

3. SUPPORT VECTOR REGRESSION

SVR is a high-dimensional and non-linear mapping machine learning method with low computational complexity that gives very good results in challenging optimization problems [28,29]. The general equations for SVR are shown below:
Consider a series of training points, $\{(x_1, d_1), (x_2, d_2), \ldots, (x_i, d_i)\}$, $x \in R^n$ ve $y \in R$. x are the input values and d expressions are used to specify the output values. The main goal is to define a regression function such as y=f(x) that accurately predicts the outputs d_i corresponding to a new set of input-output samples expressed as (x_i, d_i). The linear regression function (in feature space) is shown below:

$$f(x) = \omega\phi(x) + b$$
$$\phi : R^n \to F, \omega \in F$$

(4)

where $\Phi(x)$ is the high-dimensional feature space mapped non-linearly from the input space x. Other terms ω and b are coefficients. These coefficients can be estimated by minimizing the basic problem of SVR as follows:

$$\min R(\omega, \xi, \xi^*) = \frac{1}{2}\omega^T\omega + C\sum_{i=1}^{N}(\xi + \xi^*)$$
$$s.t. \quad d_i - f(x_i) \leq \varepsilon + \xi^*$$
$$f(x_i) - d_i \leq \varepsilon + \xi$$
$$\xi, \xi^* \geq 0, i = 1,2,3....,N, \varepsilon \geq 0$$

(5)

where slack variables ξ and $\xi*$ are used to measure the error of the up and down sides, respectively, and C is the regulator. This basic optimization problem is a linearly constrained quadratic programming problem that can be solved by introducing Lagrangian multipliers and applying Karush-Kuhn-Tucker (KKT) conditions for solving the dual problem:

$$\min R(\alpha, \alpha*) = \sum_{i=1}^{N}d_i(\alpha_i - \alpha_i^*) - \varepsilon\sum_{i=1}^{N}d_i(\alpha_i + \alpha_i^*)$$
$$-0.5\sum_{i=1}^{N}\sum_{j=1}^{N}(\alpha_i - a_i^*)(\alpha_j - \alpha_j^*)K(x_i, x_j)$$
$$s.t.\sum_{i=1}^{N}(\alpha_i - \alpha_i^*) = 0$$
$$0 \leq \alpha, \alpha^* \geq C, i = 1,2,3,....,N$$

(6)

Where $K(x_i, x_j)$ is used to denote the kernel function, and the value of this function is equal to the product $\Phi(x_i)$ and $\Phi(x_j)$. Additionally, in equation 6, the terms α and $\alpha*$ associated with the constraints are used to express the Lagrangian multipliers. The kernel function used for SVR modeling in the study is the Radial basis function (Gaussian). The equation used for this is expressed below [17,29–31]:

$$K(x_i, x_j) = e^{-\gamma\|x - x_i\|^2}$$

(7)

4. RESULT AND DISCUSSION

The aim of the study is to create a model that will predict NO_x, which has a very negative impact on the environment and human health, and FF, which is one of the largest cost inputs of airline operating expenses and is actually the source of emissions. For modeling, 165 different high-bypass turbofan

engines taken from the ICAO emission databank and frequently used in today's commercial air transportation were used. The most commonly used engines today were used in the analyses. CFM56-5B/7B engines and their variants are some of them. These engines are used in aircraft such as A320 and B738, which are frequently preferred in commercial air transportation. Moreover, GE90, CF6, LEAP 1A/1B, GEnx-1B/-2B etc. engines and their variants were used. The areas of use of these engines are again the most preferred aircrafts such as B777, B747, A320 Neo, B737 Max, B787 respectively. The above engines are only a few of the engines used in the analyses. Some of the mentioned engines can be used in other aircrafts in addition to the above aircrafts. In the model, NO_x and FF were estimated according to 3 different input values (BPR, OPR and Rated Thrust) and 4 different phases (Idle, Take-off, Climb out and approach). The large number of engines and input values makes modeling very difficult. To overcome this problem, the CSA-SVR method was used. The basis for this is that the SVR method provides very successful results in complex and challenging problems. However, SVR parameters that affect SVR performance and therefore solution quality need to be adjusted very well. For this, the CSA method was used. Using the CSA method, the SVR performance parameters that would give the best results were found and then modeling was done with SVR. Very good results were obtained as a result of combining the superior features of the two methods. The SVR parameters mentioned are regularization parameter (C), The tube size of e-insensitive loss function (ε) and γ. One of the specified hyper-parameters, C, determines the trade-off cost between minimizing training error and minimizing model complexity. Another important term, γ, is the variance of the Gaussian kernel function. ε is equivalent to the approximation accuracy placed on the training data points [29].

In the CSA-SVR model, the objective function is to find hyper parameters that will minimize the Mean squared error (MSE) value between real values and model values. In this context, the number of nests, or in other words, the number of solutions, for the CSA method was taken as 25, in line with the literature. As a matter of fact, studies on CSA performance show that this parameter gives better results in the range of 15-25. In addition, p_a, which is an important performance indicator for the CSA algorithm and determines the local and global search ability of the algorithm, was taken as 0.25, similar to the literature. This value means that the algorithm allocates 25% of the entire search to local search and the remaining 75% to global search. Performance studies show that p_a values between 0.15 and 0.30 have a positive effect on optimization performance [24]. In the CSA method, the lower limits of the coefficient (C, ε, γ) are determined as 10^{-4} for ε, 10^{-2} for the other two parameters, and the upper limits are 10^{-1} for ε and 10^4 for the other parameters. A low value of ε is important for the accuracy of the method. Therefore, ε differs in value from the other two parameters. With the idea that expanding the solution range would have a positive effect on the result efficiency, the other two parameters were taken within the ranges mentioned above. Finally, the stopping criterion in the CSA-SVR method was determined as 5000 iterations. The specified value was taken because increasing the number of iterations above this value does not affect the accuracy much and significantly prolongs the solution time.

Although the CSA method is a new metaheuristic algorithm, it can use the search space quite effectively, offer quite different solution suggestions and does not easily get stuck in local minimum. This contributes a lot to giving the best results in the selection of hyperparameters required for SVR. Thanks to these features, it is estimated that it will give better results than grid search, which is one of the most used methods for this purpose. For the SVR part of the CSA-SVR method, the LIBSVM package, which was introduced in 2000, was used. LIBSVM is a widely used and very popular support vector machine (SVM) method [30]. Using a method widely known in the field is important for the accuracy of the results. This article uses a combination of CSA and SVR as a method. The preference of LIBSVM, which allows easy adjustment in hyperparameter selection in SVR usage, provides both the ease of integration of CSA and SVR and the ability to offer different options in hyperparameter selection. Thus, the optimization process can be carried out more effectively, quickly and efficiently. The engines used in the study also cover the engines of the aircraft most frequently used in commercial air transportation today. This means that the scope of this study is quite broad. In addition to the above-mentioned advantages in estimating the specified parameters, the use of the CSA-SVR method for the first time in

the literature will provide a new approach to studies on fuel consumption and emission prediction. In order to measure the accuracy of the model, 80% of the 165 data were taken as train and the remaining 20% as test data. The data is randomly separated. The data ratio is taken as 80% and 20%, similar to the literature. A high ratio of train data such as 70-80% is necessary for an accurate model and a test ratio of 20% was deemed sufficient to evaluate the model performance.The ranges of input values are given in Figure 1-2. In addition, the comparison of real NO_x data and model data is shown in Figure 3-6, and the comparison of real FF data and model data is shown in Figures 7-10.
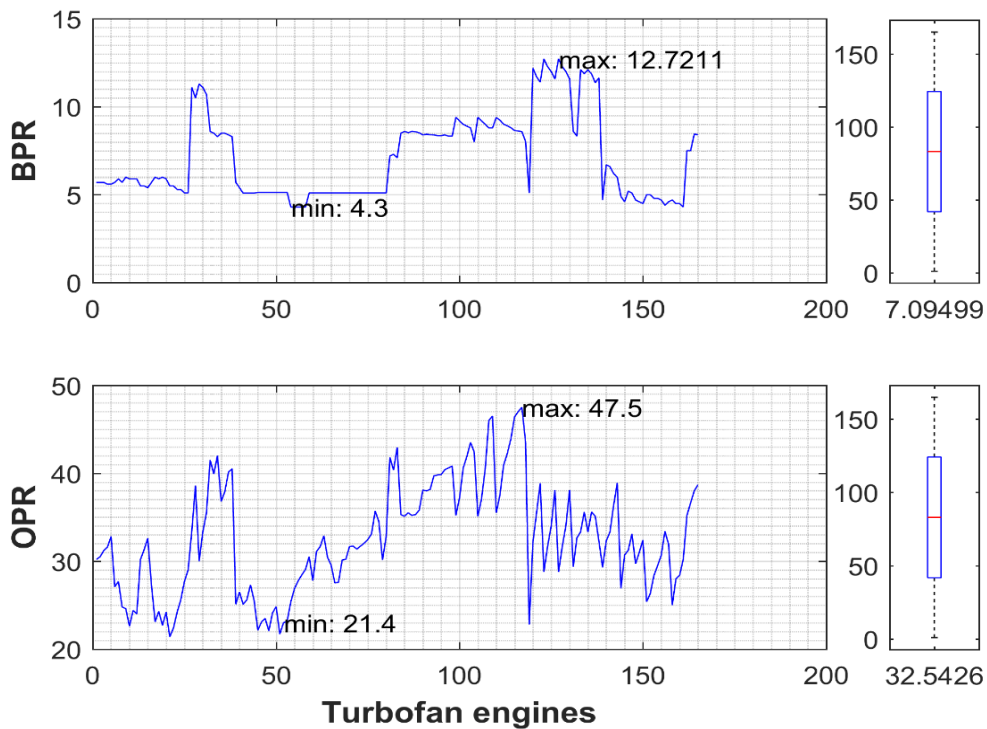
Figure 1. BPR and OPR values of aircraft engines

As can be seen in Figure 2, BPR varies between 4.3 and 12.7211. The average by-pass ratio of turbofan engines is approximately 7.095. At the same time, when the specified figure is examined, the maximum value of OPR is 47.5 and the minimum value is approximately 21.4. The average OPR value is approximately 32.543. In Figure 3, rated thrust values of turbofan engines in kN were given. Unlike BPR and OPR input values, rated thrust varies depending on engine power, so it was shown for 4 different phases.
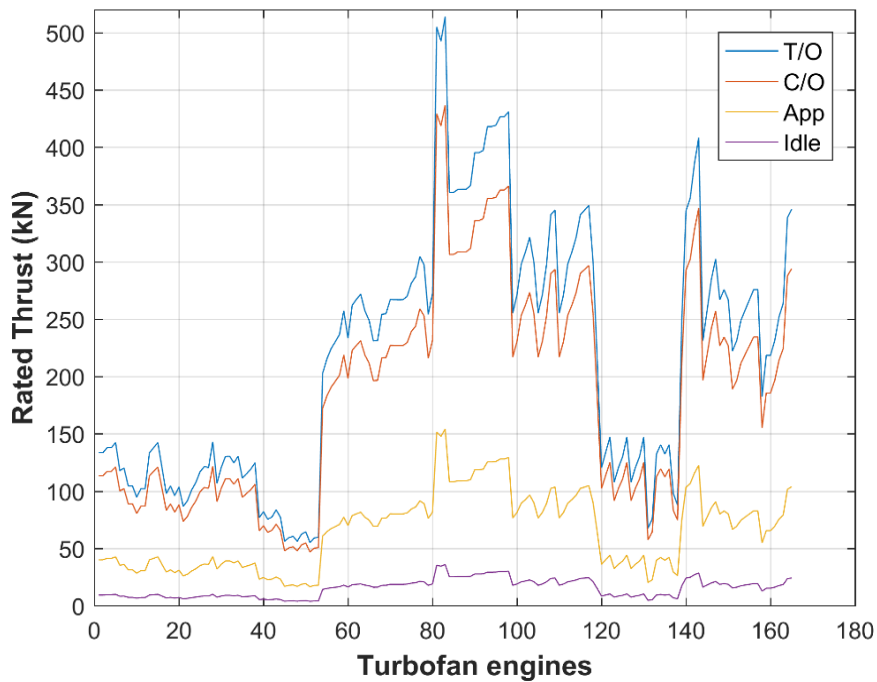
Figure 2. Rated thrust values for 4 different phases

Figure 3-6 shows the comparison of actual data and model NO$_x$ data for 4 different phases. When the specified figures are examined, it is seen that the data are shown separately as train and test data, and the real and model data results largely match in both data sets. The fact that the NO$_x$ values of turbofan engines are quite different reveals a non-linear structure. Despite this, very successful results were obtained with the CSA-SVR model. In the figures shown, it can be seen that the NO$_x$ value is maximum 64.36 (g/kg) for T/O and 6.98 (g/kg) for idle. In addition, the phase with the lowest minimum value is idle (2.86 g/kg), while the phase with the highest value is T/O with 13.51 g/kg. One of the most important reasons for this is the difference in engine power between phases.

Figure 3. Comparison of actual NO$_x$ values and model values for the T/O phase

Figure 4. Comparison of actual NO$_x$ values and model values for the C/O phase

Figure 5. Comparison of actual NO$_x$ values and model values for the app phase

Figure 6. Comparison of actual NO$_x$ values and model values for the idle phase

FF modeling was also performed within the scope of the study. Comparison of model results and actual data is shown in Figures 7-10. It can be seen from the figures that the FF model is in good agreement with the real data, as is the case with the NO$_x$ data. In addition, the phase with the highest FF is T/O and the phase with the lowest is idle.
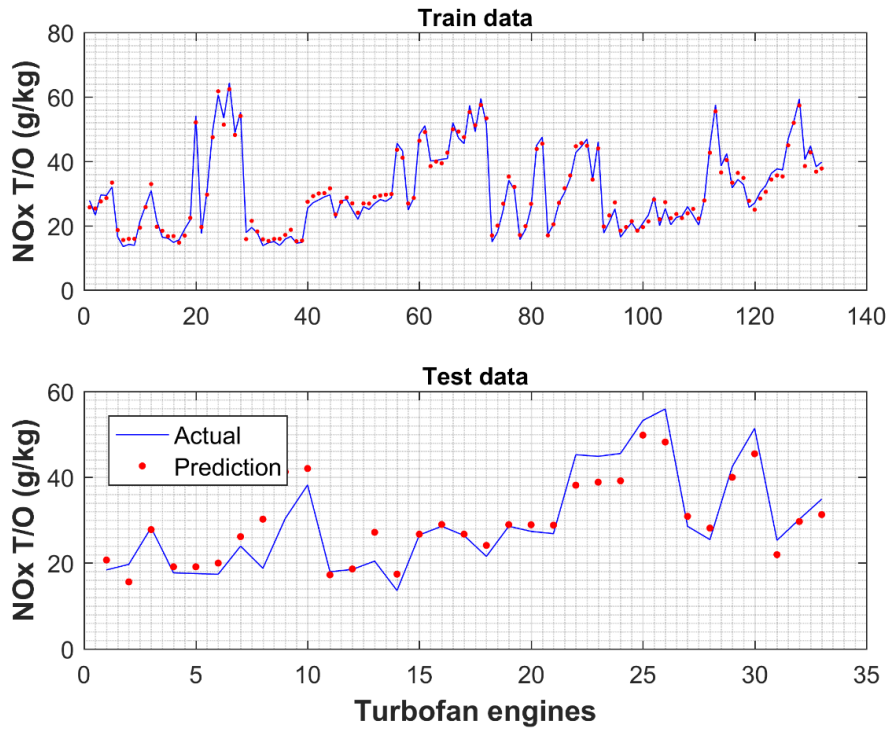

Figure 7. Comparison of actual FF values and model values for the T/O phase
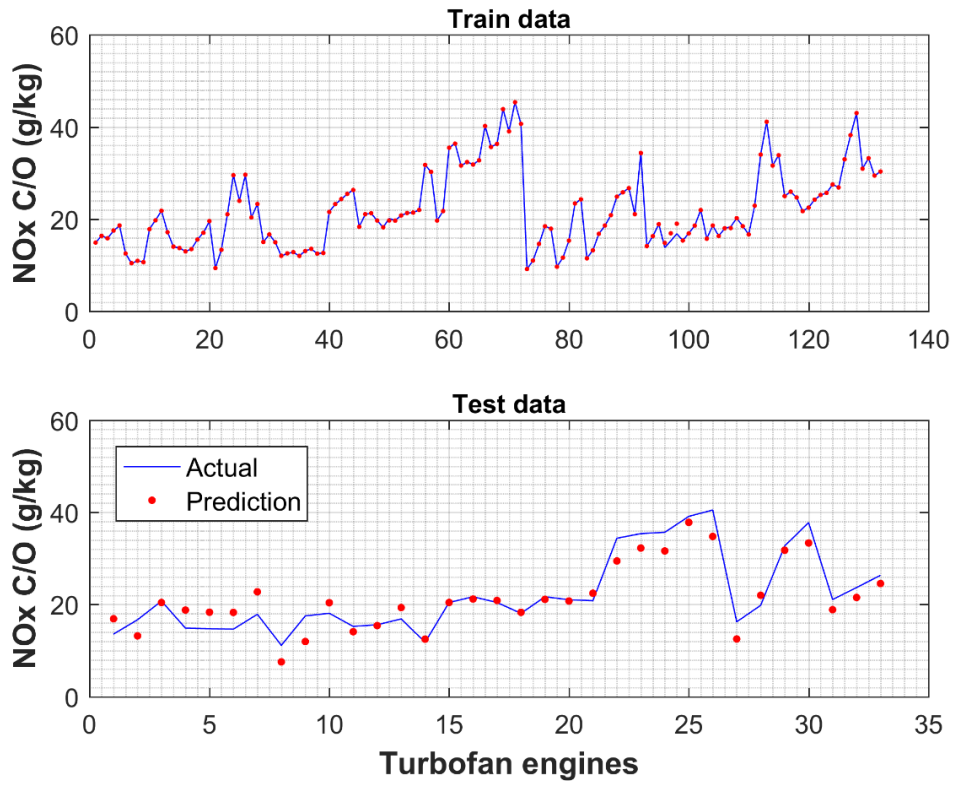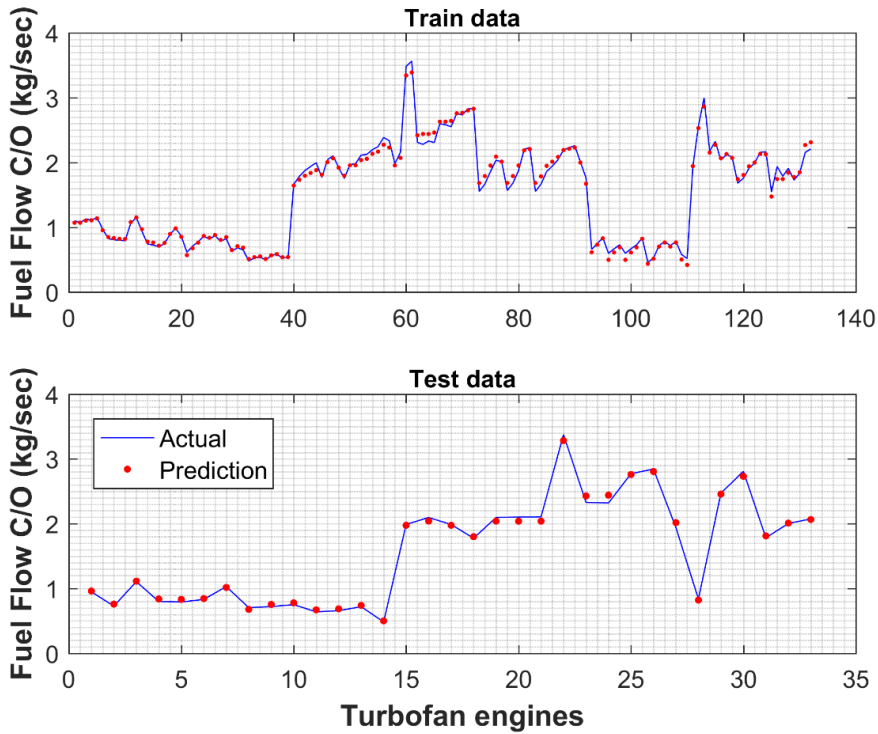

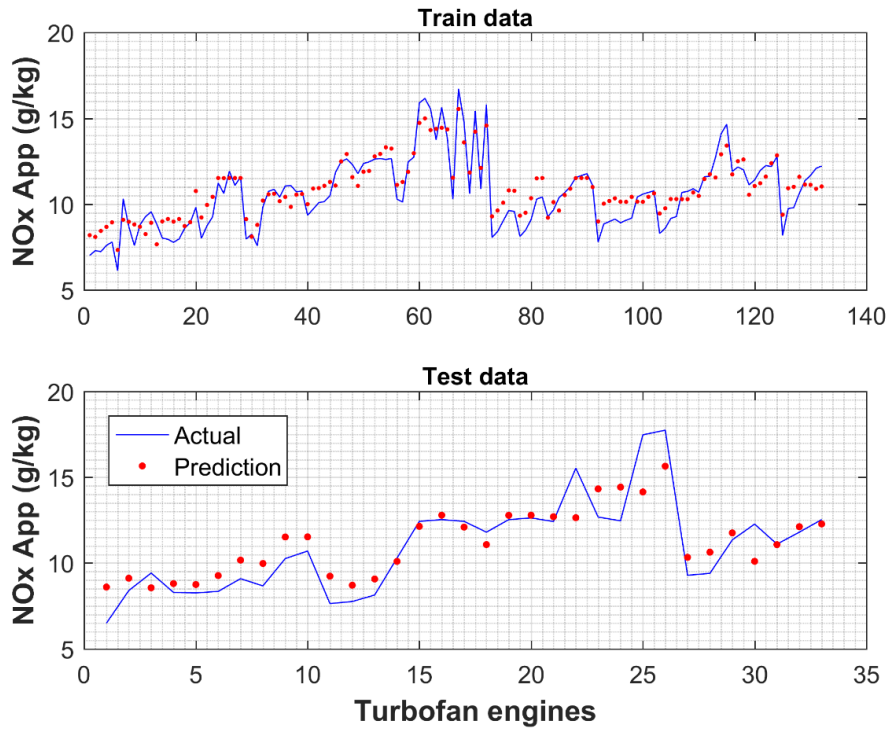**Figure 8.** Comparison of actual FF values and model values for the C/O phase

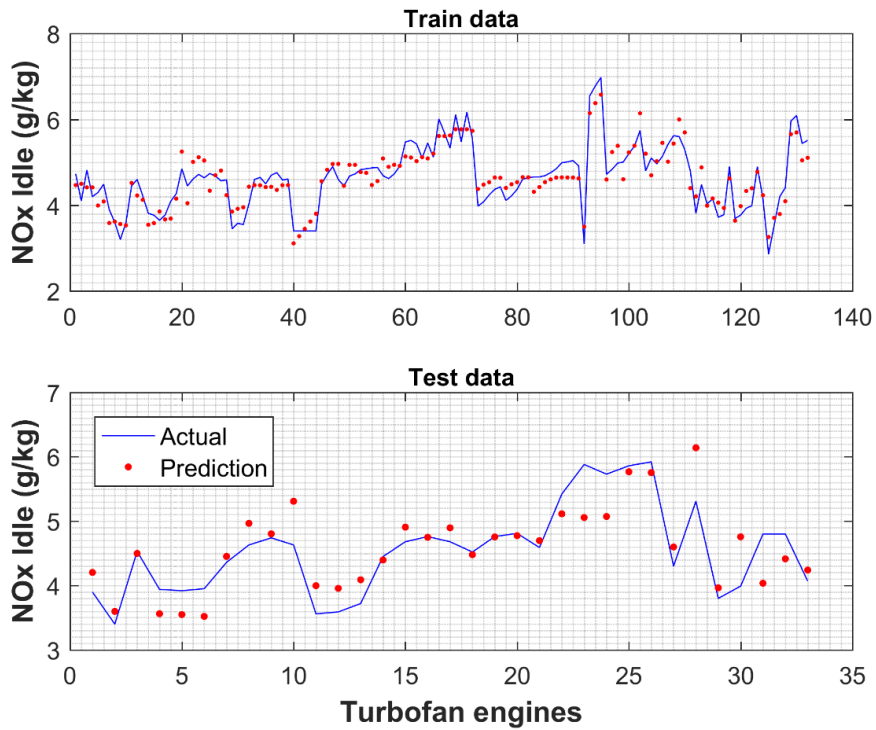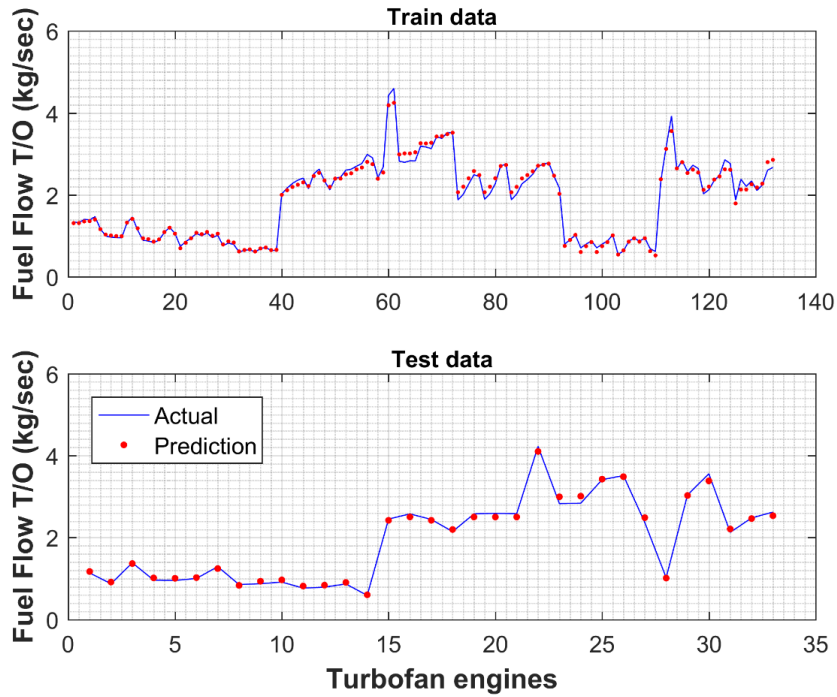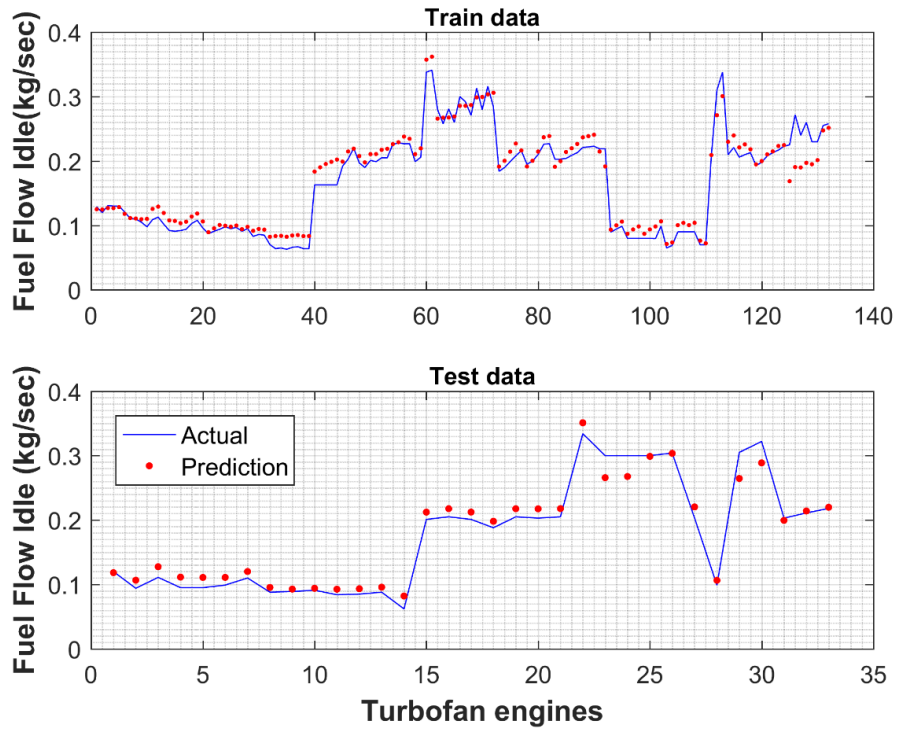**Figure 9.** Comparison of actual FF values and model values for the app phase

Figure 10. Comparison of actual FF values and model values for the idle phase

SVR performance parameters, in other words CSA model coefficients, were shown in Table 1, and model error rates were shown in Table 2. In Table 2, error rates are given in terms of MSE and Coefficient of Determination (R^2). The R^2 value being close to 1 indicates that there is a good relationship between the data set. In this context, values close to 1 indicate the accuracy of the model.

Table 1. SVR performance parameter values according to NO_x and FF models

		ε	γ	C
NO_x	T/O	0.0201	2131.7276	8167.9149
	C/O	0.0001	2477.6724	1120.2005
	App	0.0120	5041.9103	9451.5192
	Idle	0.04	614.1491	10000
FF	T/O	0.0001	0.01	10000
	C/O	0.0001	0.01	10000
	App	0.0001	0.01	9559.3102
	Idle	0.0196	0.01	10000

Table 2. Model error values

		Train		Test	
		MSE	R^2	MSE	R^2
NO_x	T/O	2.79205	0.986192	19.7715	0.861497
	C/O	6.72358×10^{-2}	0.999061	8.6542	0.884984
	App	0.768855	0.86489	1.68079	0.792779
	Idle	8.83527	0.842976	15.6282	0.6745
FF	T/O	1.01026	0.988502	0.568287	0.994988
	C/O	0.406476	0.992692	0.221538	0.996991
	App	7.32728×10^{-2}	0.986911	4.804×10^{-2}	0.994013
	Idle	3.23715	0.948679	2.59692	0.972763

5. CONCLUSION

The fact that emissions caused by aircraft engines have a significant impact on the environment and human health has caused the aviation community to carry out many studies on the subject. In addition, the fact that fuel consumption is one of the biggest cost items of airline companies increases the importance of this problem and has led to many studies on both subjects in the literature.

Within the scope of this study, a model was created to predict the NO_x emission values and fuel flow of turbofan engines with high by-pass ratio, which are also used in today's commercial air transportation. 165 different turbofan data taken from the ICAO emission databank were used for modeling. The two mentioned parameters were modeled based on BPR, OPR and rated thrust input data. Actual data for 4

different phases were estimated with the CSA-SVR method. The important findings obtained within the scope of the study are listed below:

1. The fact that this study is the first to use the CSA-SVR method on modeling NO_x emissions and fuel flow for the LTO cycle of turbofan engines with high by-pass ratio shows the originality of the method.
2. The use of BPR and OPR design parameters, which have significant effects on engine performance, and rated thrust, which is another important engine performance indicator, as input data shows the accuracy and reliability of the study.
3. For the SVR part of the CSA-SVR method, the LIBSVM package, which was introduced in 2000, was used. LIBSVM is a widely used and very popular support vector machine (SVM) method. Using a method that is widely known in the field is important for the reliability of the results.
4. The fact that today's commercial air transportation engines are used for modeling and the number of engines is quite high, 165, also shows the timeliness and accuracy of the study.
5. As a result of the error analysis methods, the fact that R^2 values are close to 1 in estimating NO_x and FF values, which have a very non-linear structure according to engine types, is another indicator that shows accuracy. Namely; minimum R^2 value for 4 phases in FF estimation was found as 0.972763. This value for NO_X was 0.6745 in the idle phase. However, this value is 0.861497, 0.884984 and 0.792779 for T/O, C/O and App, respectively, and this shows that the values are close to 1.
6. In future studies, different emission parameters will be estimated using different metaheuristic methods.

According to the results obtained, the parameters of bypass ratio, rated thrust and overall pressure ratio affect fuel consumption and NO_X values for different flight phases. Sensitivity analyses can be performed to measure the degree of effect of these parameters. Since the accuracy is high in this method, similar approaches can be applied for different emission indices (HC, CO etc.). Moreover, algorithms such as PSO and GA, which are frequently compared with CSA, can be integrated into the SVR method in emission modeling studies and compared.

CONFLICT OF INTEREST

The author stated that there are no conflicts of interest regarding the publication of this article.

CRediT AUTHOR STATEMENT

Rıdvan Oruç: Formal analysis, Writing - original draft, Visualization, Investigation, Supervision, Conceptualization.

REFERENCES

[1]   Kesgin U. Aircraft emissions at Turkish airports. Energy, 2006;31(2–3).

[2]   Fan Y Van, Perry S, Klemeš JJ, Lee CT. A review on air emissions assessment: Transportation. J Clean Prod, 2018;194.

[3]   Aygun H. Exergo-sustainability behavior of high by-pass turbofan engine of a passenger aircraft during main flight phases. Energy Sources, Part A Recover. Util. Environ. Eff, 2021; doi: 10.1080/15567036.2021.1947421.

[4]   Airbus. Global Market Forecast 2022 [Internet]. 2022 [cited 2023 Apr 13]. Available from:

https://www.airbus.com/en/products-services/commercial-aircraft/market/global-market-forecast

[5]   Boeing. Commercial Market Outlook 2022–2041 [Internet]. 2022 [cited 2023 Apr 13]. Available from: https://www.boeing.com/commercial/market/commercial-market-outlook/index.page

[6]   Baklacioglu T. Modeling the fuel flow-rate of transport aircraft during flight phases using genetic algorithm-optimized neural networks. Aerosp Sci Technol, 2016;49:52–62.

[7]   Baklacioglu T. Predicting the fuel flow rate of commercial aircraft via multilayer perceptron, radial basis function and ANFIS artificial neural networks. Aeronaut J, 2021;125(1285):453–71.

[8]   Khandelwal B, Karakurt A, Sekaran PR. Hydrogen powered aircraft : The future of air transport. Prog Aerosp Sci, 2013;60:45–59.

[9]   Oruc R, Baklacioglu T, Turan O, Aydin H. Modeling of environmental effect factor and exergetic sustainability index with cuckoo search algorithm for a business jet. Aircr Eng Aerosp Technol, 2022

[10]   Oruc R, Baklacioglu T. Propulsive modelling for JT9D-3, JT15D-4C and TF-30 turbofan engines using particle swarm optimization. Aircr Eng Aerosp Technol. 2020;92(6):939–46.

[11]   Atilgan R, Turan O, Altuntas O, Aydın H, Synylo K. Environmental impact assessment of a turboprop engine with the aid of exergy. Energy, 2013;58:664–71.

[12]   Aydin H, Turan O, Midilli A, Karakoc TH. Exergetic and exergo–economic analysis of a turboprop engine: a case study for CT7–9C. Int J Exergy, 2012;11(1):69–88.

[13]   IATA. Fuel Fact Sheet [Internet]. 2024 [cited 2024 Mar 26]. Available from: https://www.iata.org/en/iata-repository/pressroom/fact-sheets/fact-sheet---fuel/

[14]   Aygun H, Dursun OO, Toraman S. Machine learning based approach for forecasting emission parameters of mixed flow turbofan engine at high power modes., Energy, 2023; 271. doi: 10.1016/j.energy.2023.127026.

[15]   ICAO. Impacts of Aviation NOx Emissions on Air Quality, Health, and Climate [Internet]. 2022 [cited 2024 Mar 26]. Available from: https://www.icao.int/environmental-protection/Documents/EnvironmentalReports/2022/ENVReport2022_Art18.pdf

[16]   Ucar UU, Aygun H, Tanyeri B. Optimized modeling of energy and environmental metrics of mixed flow turbofan engine used regional aircraft. J Therm Anal Calorim, 2023

[17]   Dursun OO, Toraman S, Aygun H. Deep learning approach for prediction of exergy and emission parameters of commercial high by-pass turbofan engines. Environ Sci Pollut Res, 2023;30:27539–27559.

[18]   Trani AA, Wing-Ho FC, Schilling G, Baik H, Seshadri A. A neural network model to estimate aircraft fuel consumption. In: Collection of Technical Papers - AIAA 4th Aviation Technology, Integration, and Operations Forum, ATIO. Chicago, Illinois: AIAA; 2004. p. 6401.

[19]   Baklacioglu T. Fuel flow-rate modelling of transport aircraft for the climb flight using genetic algorithms. Aeronaut J, 2015;119(1212):173–83.

[20]   Oruc R, Baklacioglu T. Modelling of fuel flow-rate of commercial aircraft for the climbing flight using cuckoo search algorithm. Aircr Eng Aerosp Technol, 2020;92(3):495–501.

[21]   Oruc R, Baklacioglu T. Modeling of fuel flow-rate of commercial aircraft for the descent flight using particle swarm optimization. Aircr Eng Aerosp Technol, 2021;93(2):319–26.

[22]   EASA. ICAO Aircraft Engine Emissions Databank [Internet]. [cited 2022 Nov 23]. Available from: https://www.easa.europa.eu/en/domains/environment/icao-aircraft-engine-emissions-databank

[23]   Yang XS. Nature-Inspired Optimization Algorithms. Nature-Inspired Optimization Algorithms, 2014.

[24]   Yang XS, Deb S. Engineering optimisation by cuckoo search. Int J Math Model Numer Optim, 2010

[25]   Joshi AS, Kulkarni O, Kakandikar GM, Nandedkar VM. Cuckoo Search Optimization- A Review. Mater Today Proc, 2017;4(8):7262–9.

[26]   Gandomi AH, Yang XS, Alavi AH. Cuckoo search algorithm: A metaheuristic approach to solve structural optimization problems. Eng Comput, 2013;29(1):17–35.

[27]   Yang XS, Deb S. Cuckoo search via Lévy flights. In: 2009 World Congress on Nature and Biologically Inspired Computing, NABIC 2009 - Proceedings. IEEE; 2009. p. 210–4.

[28]   Huang S, Tian L, Zhang J, Chai X, Wang H, Zhang H. Support Vector Regression Based on the Particle Swarm Optimization Algorithm for Tight Oil Recovery Prediction. ACS Omega. 2021;6(47):32142–32150.

[29]   Wu J, Zhou J, Gao Y. Support vector regression based on particle swarm optimization and projection pursuit technology for rainfall forecasting. In: 2009 International Conference on Computational Intelligence and Security. Beijing, China: IEEE; 2009. p. 227–330.

[30]   Chang CC, Lin CJ. LIBSVM: A Library for support vector machines. ACM Trans Intell Syst Technol, 2011;2(3).

[31]   Zhao S, Wang L. No Title. In: 2010 Third International Joint Conference on Computational Science and Optimization, 2010. p. 484–7.

RESEARCH ARTICLE

THE OPTIMIZATION OF RAILWAY FASTENER DEFECT DETECTION VIA ACTIVATION FUNCTION ADAPTATIONS

Ridvan OZDEMIR [1, 2], Mehmet KOC [3] *

[1] Eti Makine, Eskisehir, Turkey.
[2] Institution of Graduate Schools, Bilecik Seyh Edebali University, Bilecik, Turkey
ridvan.ozdemir@etimakine.com.tr - 0000-0002-8599-1709

[3] Department of Computer Engineering, Faculty of Engineering, Eskisehir Technical University, Eskisehir, Turkey
mehmetkoc@eskisehir.edu.tr - 0000-0003-2919-6011

Abstract

Manual control of rail defect detection is slow and costly. Deep learning methods can detect some of these defects to a certain extent. However, existing systems produce too many false positives due to environmental factors, resulting in labor and cost losses. One of the most important components in railway systems is the fastener, and their failure can lead to severe accidents. In this study, we developed a deep learning-based method that is designed to remain robust against foreign objects and environmental conditions when detecting railway fasteners. By employing various activation functions and expanding the training dataset through data augmentation techniques, our method significantly reduces false alarms. The best-performing activation function in our tests achieved an F1-score of 0.99 and a mean average precision (mAP) of 100%. Testing on a dataset provided by TCDD Railway Research & Technology Centre (DATEM) confirms the efficacy of our approach, demonstrating a notable decrease in unnecessary work and associated costs.

1. INTRODUCTION

Railway transportation has a critical role in both passenger and freight transportation since it is economical and safe. The importance of high-speed trains in passenger transportation is increasing day by day due to the comfort and speed they provide. The increasing use of rail transportation also makes the detection and maintenance of railroad faults more critical. In the past, manual fault detection and control operations were both costly and slow. With the development of technology, these manual processes can now be performed much faster using vision and artificial intelligence-based algorithms. Vision-based methods are widely adopted for railway fastener detection because of their precision and ease of integration with existing monitoring systems. Other techniques, such as acoustic and laser-based methods, have also been explored in some studies. [1, 2]. However, the defect detection models used have not yet reached the desired level. Single-Stage Object Detection (SSD) is the general name for object detection methods that perform object detection and classification simultaneously within a single neural network architecture and are effective in real-time applications. The main advantages of SSD are its simplicity, speed, and suitability for detection of objects with different sizes. In this study, the SSD model You Look Only Once v4 (YOLOv4) is used to detect defects in fasteners that are critical for railway safety. The performance of the SSD model is analyzed using different activation functions. Activation functions directly affect the performance of the model due to the nonlinearity they add to the

---

model. [3]. This feature distinguishes them from simple linear models and enables them to provide successful results for challenging real-world problems.

In 2019, Lin et al. published a paper in which they mentioned that railway fasteners are one of the most important components of the railway, and their damage control is done manually. They trained the YOLOv3 model with 20 km of GoPro images and achieved 89% and 95% precision and recall, respectively [4]. In 2020, Qi et al. stated in their article that real-time detection of defects in railway fasteners would be a significant improvement in this field. They also noted that this task is challenging due to the memory and processor limitations of embedded maintenance systems. With the MYOLOv3-Tiny model they developed, the accuracy value reached 99.33% and the memory consumption was reduced by 43% compared to the YOLOv3-Tiny model [5]. Güçlü et al. introduced a novel method utilizing fuzzy logic and YOLOv4 in their study. They achieved a success rate of 99.25% in classifying faulty fasteners on the test dataset [6]. In 2021, Liao et al. investigated the effects of activation functions on the learning process with benchmarks and successfully detected surface defects with the hybrid model they developed, achieving an of 98.64% mAP value in their study [7]. Şener et al. propose an AI-based model using the Tensorflow library and deep learning approaches to identify problems in railway tracks with an overall accuracy of 92.2% [8]. Ozdemir and Koc used a semi-supervised deep learning strategy with a student-teacher model and YOLOv4 to detect various defects encountered in railways [9]. They used a new dataset from the Turkish State Railways (TCDD), which contains five different defects, including fastener faults. Their method automates the process of adding appropriately pseudo-labeled images to the training dataset, enhancing model performance, and lowering the labor-intensive task of manual labeling. Sevi et al. proposed a deep learning-based approach to classify defects in railway fasteners by generating defective data from images of healthy rail fasteners. They used CNN, VGG16, and ResNet50 models to classify fastener defects, achieving a 100% accuracy rate with the proposed method [10]. He et al. added a SE attention mechanism, replaced the backbone with a lightweight MobileNet-V2 network, and included Mixup data augmentation to improve the Yolov4 model for track fastening service status detection [11]. As compared to the conventional Yolov4 model, their results demonstrated a 67.39% increase in processing speed and an 83.2% MAP increase in detection accuracy. Yılmazer et al. aimed to detect three different fault classes, including missing fasteners, along with the state of healthy sleepers, with the model's accuracy determined to be 95% in the performed tests. [12].Zengzhen Mi et al. found that their improved version of the YOLOv4 model outperformed YOLOv3, YOLOv4, YOLOv5, YOLOv6, Faster RCNN, and SSD models, achieving an F1 score of 0.925 compared to YOLOv6's 0.914 [13]. In our work, we use the original YOLOv4 model to evaluate the impact of different activation functions on railway fastener detection.

The dataset provided by TCDD was obtained using a track inspection system called VCUBE. There were many false positives in the detections made by V-CUBE, with the precision value being about 11%; this means that only 301 out of 2730 detections were true. The false positives (FPs) may occur due to the ballasts on the fasteners and other environmental conditions, resulting in very low performance. This study, focusing on fastener defects, was conducted to address this problem. Additionally, the effects of activation function selection and data augmentation on the model's performance were analyzed.

2. MATERIALS and METHODS

2.1. Dataset

One of the most critical factors in the success of deep learning models is the dataset [14]. The more accurate and consistent the labels and tags in the dataset used to train the model, and the higher the class diversity, the more successful the model will be. The dataset in this study, which was created using railroad images provided by TCDD, was obtained using a track inspection system. These images were

analyzed, and the marking and labeling were done carefully. After analyzing all the images, the following three classes were created:

- **Sleeper**: Placed under the rails and used to support the rails. It stabilizes the rails by distributing the load under the rails and ensures the contact of the rails with the ground.
- **Fastening OK**: Fasteners are used to attach rails and rail components. These parts connect the rails to the bearings and substructure and ensure that the track is safe and stable. Various types of fasteners can be used to ensure that the rails are held in place and secured. These systems increase the life of the track by absorbing vibrations and carrying the loads of the rails. Fastening systems typically consist of rail clips, screws, wedges, and other hardware.
- **Fastening NOK**: If the fastener is deformed for any reason, or if it rotates and loses contact with the rail, the safety of the rail line is compromised. Fasteners in the images under this condition are labeled as "Fastening NOK".

Labeled sample images of the Sleeper, Fastening OK, and Fastening NOK classes are shown in Figure 1.
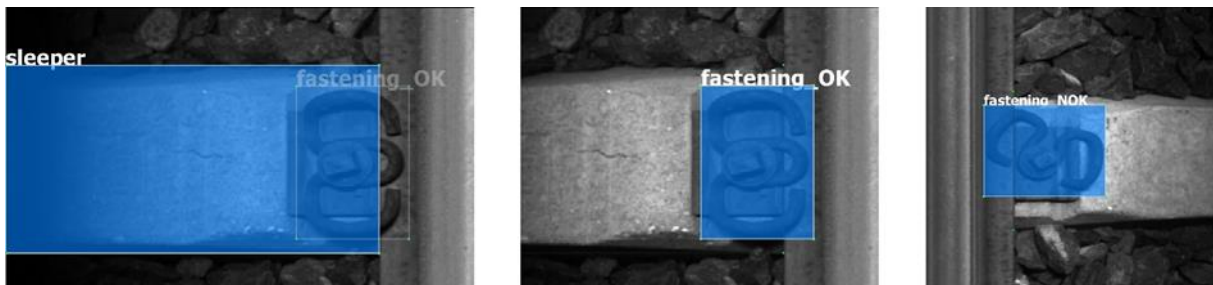
Figure 1. Examples of Sleeper, Fastening OK and Fastening NOK Classes

After analyzing the railroad images received from TCDD, approximately 89% of the classifications were found to be incorrect. For example, Figure 2 shows images that were initially classified as incorrect in the dataset but were actually correct. By analyzing all images, those that were truly defective were identified and separated from the non-defective ones, as demonstrated in Figure 3.
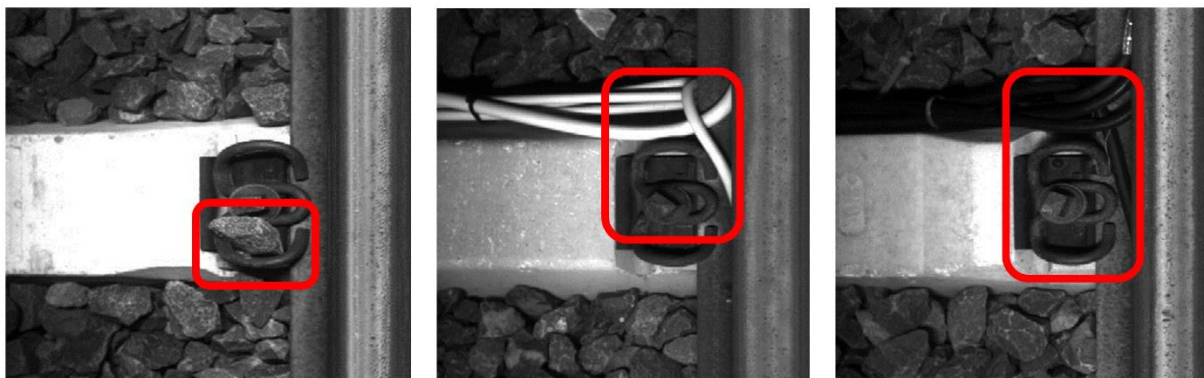
Figure 2. Normal images that are labeled as defective
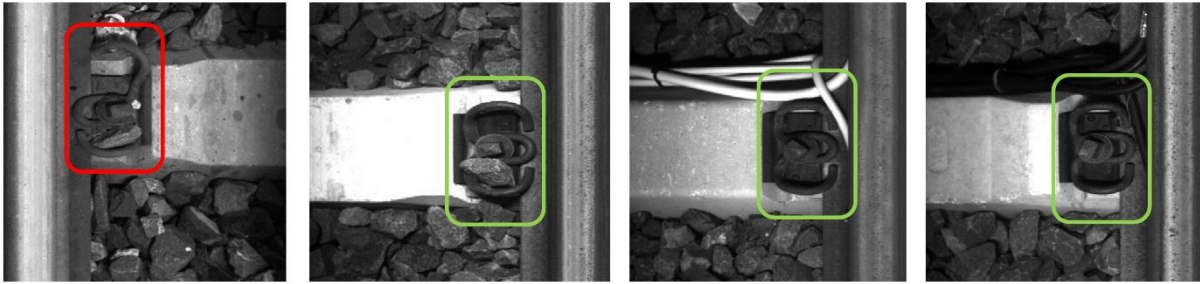
Figure 3. Checking for images that are labeled as defective

Training, validation, and test datasets were then created from the acquired images, which were labeled in YOLO format using the labelImg program. In addition to labeling the fasteners, the sleepers in the images were also labeled, creating a dataset that facilitates the detection of missing fastener defects if needed. The numbers of images in the training, validation, and test datasets, along with the number of classes in these images, are provided in Table 1.

Table 1. Number of Images in Training, Validation, and Test Datasets

Dataset	image	sleeper	fastening_OK	fastening_NOK
Training	812	812	571	241
Validation	100	100	68	32
Test	100	100	72	28

The use of data augmentation techniques, specifically adjustments in contrast and orientation, expanded the training dataset to four times its original size by increasing the number of images. The augmented training dataset has 3248 images which contains 3248 sleepers, 2284 fastening_OK, and 964 fastening_NOK samples.

2.2. YOLOv4

YOLOv4 is an object detection algorithm that provides advantages such as high accuracy, speed, and scalability [15]. In this study, the YOLOv4 detection algorithm is used to detect the defects of railway fasteners with high accuracy and reduce the number of false positives.

The architecture of YOLOv4 generally consists of Backbone, Neck, Head sections. The tasks of these sections are briefly described below:
- **Backbone**: In YOLOv4, it is based on CSPDarknet53, a pre-trained deep learning model. CSPDarknet53 [16] is a Convolutional Neural Network (CNN) based architecture and includes a series of convolution and pooling layers to transform the image into smaller feature maps.
- **Neck**: This section processes the output from the backbone network and contains several convolution and scaling layers that combine and compress feature maps at different scales. Typically, a neck consists of several paths from the bottom up and several paths from the top down. In the neck part of the architecture of YOLOv4, SPP (Spatial Pyramid Pooling) add-on module and PANet path aggregation were chosen. PAN (Path Aggregation Network) in this section [17] is a network that performs the operations of merging and expanding feature maps. SPP [18] layer contains max-pooling outputs with 1×1, 5×5, 9×9, 13×13 kernel sizes and adds imaginary connections, so the model can be trained shorter time also had a higher performance.
- **Head:** The head section is the dense prediction layer. It contains bounding boxes and the class of each box is estimated. The models implemented in YOLOv3 are used here. Thanks to the

mechanism that YOLOv4 has, the model is able to recognize both small and large objects with the same level of accuracy.

A figure summarizing the structure of the YOLOv4 algorithm is shown in Figure 4. Yolov4 uses a composite loss function which is made up of three components: (*i*) Bounding box regression loss ($\mathcal{L}_{loc}$) improves the overlap, center distance, and aspect ratio consistency to ensure that predicted bounding boxes in the object detection tasks are accurately aligned with the ground truth. (*ii*) Confidence loss ($\mathcal{L}_{conf}$) penalizes incorrect object evaluations by using binary cross-entropy to determine the model's confidence about whether the bounding box contains an object. (*iii*) Classification loss ($\mathcal{L}_{clc}$) quantifies how well a model can classify an object inside a bounding box. The total loss is the weighted sum of these three loses:

$$\mathcal{L} = \lambda_{loc}\mathcal{L}_{loc} + \lambda_{conf}\mathcal{L}_{conf} + \lambda_{cls}\mathcal{L}_{cls} \tag{1}$$

where λ_{loc}, λ_{conf}, and λ_{cls} are the corresponding weight coefficients.
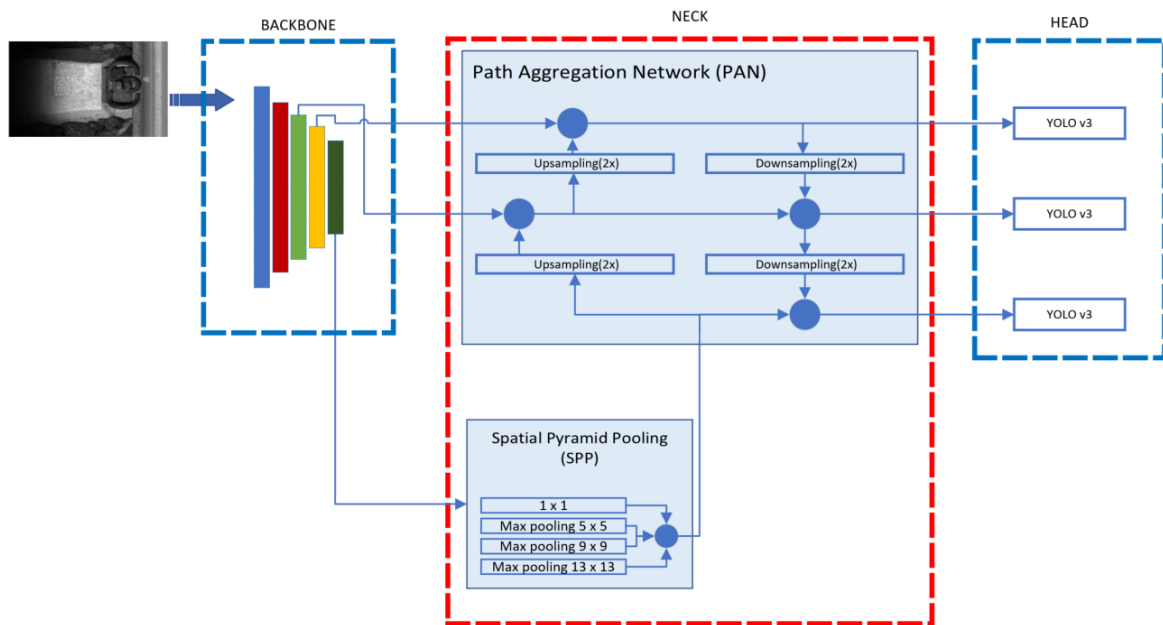
Figure 4. YOLOv4 Architecture [19]

2.3. Activation Functions

Some activation functions commonly used in the literature are selected to investigate the learning performance of the model and their performances are compared on the test dataset. The activation functions are designed to optimize the training of the model, deal with gradient vanishing/exploding problems, and improve the learning process. The ideal activation function may differ based on the model and application. Figure 5 depicts some of the most frequent activation functions used to train deep learning models.
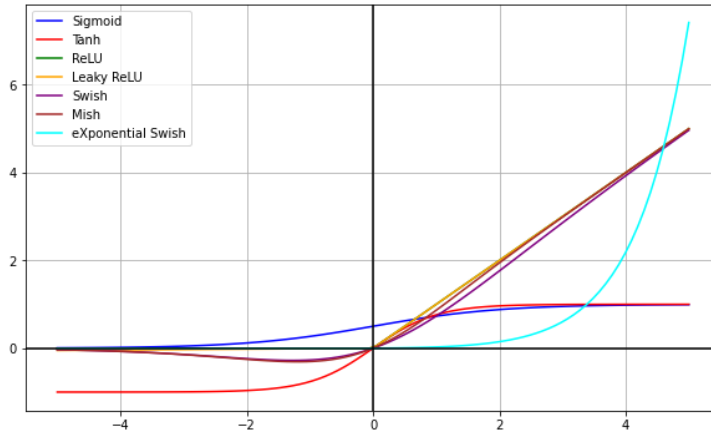
Figure 5. Comparison of Activation Functions

In this study, the activation functions Leaky ReLU (Rectified Linear Unit), Swish, x-Swish (Exponential Swish) and Mish were employed during the model training process. Each of these activation functions is described in detail below:

Leaky ReLU: It multiplies the input by a small slope value when the input is negative. This means that $x < 0$ when the Leaky ReLU is multiplied by α. Adding a small slope to negative inputs that are zero is intended to increase the model's ability to learn.

$$f(x) = \begin{cases} x & x \geq 0 \\ \alpha x & x < 0 \end{cases} \tag{2}$$

Swish: It applies the sigmoid function to the input and then multiplies the input by the result. The Swish function produces a smooth version of the sigmoid as the value of x increases. Swish has smoother derivatives, which can make training more stable.

$$f(x) = x\ \sigma(x) = \frac{x}{1 + e^{-x}} \tag{3}$$

x-Swish (eXponential Swish): x-Swish has been proposed to improve the Swish function. x-Swish aims to improve the performance of Swish by adding an additional scaling factor.

$$f(x) = \beta x \sigma(x) = \frac{\beta x}{1 + e^{-x}} \tag{4}$$

Mish: Mish is a nonlinear function that multiplies the input by the hyperbolic tangent (tanh) function of x. Mish has a smoother curve than other activation functions, especially Swish and ReLU.

$$f(x) = x\tanh(\ln(1 + e^x)) \tag{5}$$

Mish*: Mish* activation function is combined with both the Mish activation function and the SAM (Spatial Attention Module) module. This can help the model to focus on important regions in the feature map. The mathematical formulation of this special function may vary depending on the application context, but in general it includes mish activation function and spatial attention features. Mish* aims to achieve better performance in tasks such as object detection by combining the spatial attention feature with the Mish function. Unlike the Mish activation function, the plug-in modules have not only SPP, but also SAM, and the head part uses the linear activation function instead of the logistic one.

3. EXPERIMENTS

To compare the performance of the fault detection model developed with the YOLOv4 object detection algorithm trained on our custom railway fastener dataset, we conducted 10 different experiments using various activation functions. In these experiments, the YOLOv4 model is trained using hyperparameters with an input size of 352 × 352 pixels, a batch size of 64, and a mini-batch size of 32. The learning rate is set at 0.001 and the momentum at 0.949. The training is conducted over 12,000 iterations with the Adam optimizer. The experiments are conducted on a desktop PC operating Windows 11, equipped with an Intel i7-11700 CPU at 2.50GHz, an RTX3060 Ti GPU, and 16GB of RAM.

Evaluation Metrics:

The evaluation of detection accuracy involves the utilization of metrics such as Precision, Recall, F_1-score, Intersection over Union (IoU), and mean average precision (mAP), which are delineated as follows:

$$\text{Precision} = \frac{TP}{TP + FP} \tag{6}$$

$$\text{Recall} = \frac{TP}{TP + FN} \tag{7}$$

$$F_1 - \text{score} = 2 \times \frac{\text{Precision} \times \text{Recall}}{\text{Precision} + \text{Recall}} \tag{8}$$

$$\text{IoU} = \frac{TP}{TP + FP + FN} \tag{9}$$

$$\text{mAP} = \frac{1}{C} \sum_{i=0}^{C} AP_i \tag{10}$$

Here C represents the total number of categories within the image dataset. TP, FN, and FP denote true positive, false negative, and false positive, respectively. In this study, the prediction anchor box is classified as true positive (TP) if its Intersection over Union (IoU) value equals or exceeds a predefined threshold, denoted as T, which is set at 0.5.

Table 2. Comparison of Activation Function Performances

Activation	F_1-score	recall	precision	IoU	mAP
leaky	0.99	0.99	0.98	93.07	98.62
swish	0.86	0.93	0.80	75.80	99.20
x-swish	0.92	0.95	0.90	87.13	97.97
mish	**0.93**	**1.00**	**0.87**	**81.83**	**99.24**
mish*	0.98	0.99	0.98	92.57	98.70

To investigate the effects of activation functions on the performance of the model, Swish, x-Swish, Mish, and Mish* activation functions were selected one at a time instead of Leaky ReLU and the model was trained on the training dataset. As a result of this training, performance comparisons were made on the test dataset with the models obtained using different activation functions. The results of these tests were compared with the overall performance indices in Table 2, and the class-based performance results are shown in Table 3 on the dataset. With the Mish activation function detecting 27 out of 28 defective fasteners, it achieved the best result, marking an improvement of 3.57% and attaining an F_1-score of 0.93. Although the best result was obtained in the detection of faulty fasteners, the overall performance was degraded due to the high number of false positives in the "sleeper" and "fastening_OK" classes.

Table 3. Class Based Performance of Activation Functions

	Sleeper			Fastening_OK			Fastening_NOK		
activation	**AP**	**TP**	**FP**	**AP**	**TP**	**FP**	**AP**	**TP**	**FP**
leaky	100.00	100	0	99.67	72	4	96.18	26	0
swish	100.00	89	36	99.12	70	7	98.49	26	2
x-swish	100.00	94	11	99.01	71	6	94.89	26	5
mish	**100.00**	**100**	**24**	**100.00**	**72**	**6**	**97.73**	**27**	**1**
mish*	100.00	100	0	99.67	72	5	96.43	26	0

To improve the performance of the error detection model, the number of images in the training dataset was increased using data augmentation methods including flipping, contrast reduction, and contrast enhancement. In this way, a training data set was obtained that is more adaptable to changing light conditions at different times of the day, when the weather is cloudy or sunny. As a result of these operations, the number of images was increased, and the training dataset was expanded to four times its original size. With the extended training dataset, the models with leaky ReLU, Swish, X-Swish, Mish, and Mish* activation functions were retrained. The performance of the new models was compared on the test dataset. The results were compared with the overall performance indices listed in Table 4 and on a class-by-class basis in Table 5. Analysis of the tables shows that the models trained with both the Swish and Mish* activation functions successfully detected all defective images. However, the model trained with the Mish* activation function outperformed the Swish-activated model on the F1-score index, achieving 0.99 compared to 0.93. This superiority is attributed to the Swish model producing more false positives and its failure to detect some true positives in the "sleeper" and "fastening_OK" classes. As a result, Mish* was found to be the most successful function.

Table 4. Comparison of Activation Function Performances on an Extended Training Dataset

Activation	F_1-score	recall	precision	IoU	mAP
leaky	0.99	0.99	0.98	92.93	100.00
swish	0.93	0.95	0.90	84.48	100.00
x-swish	0.93	0.93	0.93	87.16	99.96
mish	0.97	0.98	0.96	90.51	99.94
mish*	**0.99**	**1.00**	**0.99**	**93.51**	**100.00**

Table 5. Class Based Performance of Activation Functions

	Sleeper			Fastening_OK			Fastening_NOK		
Activation	**ap**	**TP**	**FP**	**ap**	**TP**	**FP**	**ap**	**TP**	**FP**
leaky	100.00	100	0	100.00	72	4	100.00	26	0
swish	100.00	94	14	100.00	68	5	100.00	28	1
x-swish	100.00	87	13	100.00	72	2	99.88	27	0
mish	100.00	96	5	99.94	72	4	99.88	27	0
mish*	**100.00**	**100**	**0**	**100.00**	**72**	**3**	**100.00**	**28**	**0**

4. CONCLUSION

The ballasts on the fasteners and other environmental factors cause a lot of false positives (FPs) in the current system that generates the dataset for TCDD, which leads to poor defect detection performance. YOLOv4 models incorporating Leaky ReLU, Swish, x-Swish, Mish, and Mish* activation functions were trained on this new dataset, which was organized considering the environmental conditions. When evaluating the performance of the 'Railway Fastener Fault Detection Module' on the test dataset, it was

initially observed that one faulty fastener was missed. However, following the implementation of data augmentation improvements, all faulty fasteners were successfully detected. This module achieved an improvement of 1% in recall and precision values and 1.38% in mAP by using different activation functions compared to the initial setup. Consequently, many false positives were avoided, unnecessary work loss was prevented, and productivity was increased.

ACKNOWLEDGMENTS

CONFLICT OF INTEREST

The authors stated that there are no conflicts of interest regarding the publication of this article.

CRediT AUTHOR STATEMENT

Ridvan Ozdemir: Methodology, Software, Validation, Data Curation, Writing – Original Draft, Visualization, Conceptualization. **Mehmet Koc:** Writing – Review & Editing, Supervision, Resources, Conceptualization.

REFERENCES

[1]   Dinhobl G, Petz M, Kümmritz S, Hutterer H. On Measurement of Railway Noise: Usability of Acoustic Camera. In: Degrande G, Lombaert G, Anderson D, de Vos P, Gautier P-E, Iida M, Nelson JT, Nielsen JCO, Thompson DJ, Tielkes T, Towers DA, editors. Noise and Vibration Mitigation for Rail Transportation Systems. Cham: Springer International Publishing, 2021, pp. 234–241.

[2]   Assali P, Viguier F, Pollet N. Contribution of Terrestrial Laser Scanning for monitoring and inspection of railway infrastructure. In Proceedings of the World Congress on Railway Research; 2013 Nov 25-28; Sydney, Australia. 2013.

[3]   Szandała T. Review and comparison of commonly used activation functions for deep neural networks. In: Bio-inspired Neurocomputing 903, Bhoi AK, Mallick PK, Liu CM, Balas VE, editors. Studies in Computational Intelligence, vol. 903. Singapore: Springer Singapore, 2021, pp. 203–224.

[4]   Lin Y-W, Hsieh C-C, Huang W-H, Hsieh S-L, Hung W-H. Railway track fasteners fault detection using deep learning. In: 2019 IEEE Eurasia Conference on IOT, Communication and Engineering, 2019, pp. 187–190.

[5]   Qi H, Xu T, Wang G, Cheng Y, Chen C. MYOLOv3-Tiny: A new convolutional neural network architecture for real-time detection of track fasteners. Computers in Industry; 2020; 123: 103303.

[6]   Güçlü E, Aydin İ, Şahbaz K., Akin E, Karaköse M. Detection of defects in railway fasteners using YOLOv4 and fuzzy logic (article in Turkish with an abstract in English). Railway Engineering 2021; 14: 249-262.

[7]   Liao X, Lv S, Li D, Luo Y, Zhu Z, Jiang C. YOLOv4-MN3 for PCB surface defect detection. Applied Sciences 2021; 11(24):1-17.

[8]   Şener A, Ergen B, Toğaçar M. Fault detection from images of railroad lines using the deep learning model built with the tensorflow library. Turkish Journal of Science & Technology 2022; 17(1): 47-53.

[9]   Ozdemir R, Koc M. On the enhancement of semi-supervised deep learning-based railway defect detection using pseudo-labels. Expert Systems With Applications 2024; 251: 124105.

[10]   Sevï M, Aydın İ, Karaköse M. Classification of railway fasteners by deep learning methods (article in Turkish with an abstract in English). European Journal of Science and Technology 2022; 35: 268-274.

[11]   He J, Wang W, Yang N. Research on track fastener service status detection based on improved YOLOv4 model. Journal of Transportation Technologies; 14: 212-223.

[12]   Yılmazer M, Karaköse M, Aydın İ, Akın E. Multiple fault detection in railway components with mask R-CNN deep neural network (article in Turkish with an abstract in English) Cukurova University Journal of the Faculty of Engineering 2022; 37(4); 1103-1111.

[13]   Mi Z. Research on steel rail surface defects detection based on improved YOLOv4 network. Frontiers in Neurorobotics 2023; 17: 1-11.

[14]   Alzubaidi L, Zhang J, Humaidi AJ, Al-Dujaili A, Duan Y, Al-Shamma O, Santamaria J, Fadhel MA, Al-Amidie M, Farhan L. Review of deep learning: concepts, CNN architectures, challenges, applications, future directions 2021; 8(1); 1-74.

[15]   Bochkovskiy A, Wang C-Y, Liao H-YM. YOLOv4: Optimal speed and accuracy of object detection. arXiv preprint 2020; 2004.10934.

[16]   Wang C-Y, Liao H-YM, Wu YH, Chen P-Y, Hsieh J-W, Yeh I-H, CSPNet: a new backbone that can enhance learning capability of CNN. In Proceedings of the IEEE/CVF Conference on Computer Vision and Pattern Recognition (CVPR) Workshops; 2020; pp. 390-391.

[17]   Liu S, Qi L, Qin H, Shi J, Jia J. Path aggregation network for instance segmentation. In Proceedings of the IEEE Conference on Computer Vision and Pattern Recognition; 2018; pp. 8759-8768.

[18]   He K, Zhang X, Ren S, Sun J. Spatial pyramid pooling in deep convolutional networks for visual recognition IEEE Transactions of Pattern Analysis and Machine Intelligence 2015; 37(9): 1904-1916.

[19]   Getting Started with YOLOv4 - MATLAB & Simulink. Accessed: Feb. 23, 2024. [Online]. Available: https://www.mathworks.com/help/vision/ug/getting-started-with-yolo-v4.html

RESEARCH ARTICLE

MODELING AND PERFORMANCE ANALYSIS OF HIGH BANDWIDTH TRANSIMPEDANCE AMPLIFIERS IN OPTICAL COMMUNICATIONS

Berkay ÇAVUŞ [1, *], Şekip Esat HAYBER [2]

[1] Department of Electrical-Electronic Engineering, Engineering Faculty, Bursa Uludağ University, Bursa, Turkey
berkaycavus@gmail.com - *0009-0007-1184-8807*

[2] Department of Electrical-Electronic Engineering, Engineering Faculty, Bursa Uludağ University, Bursa, Turkey
sehayber@uludag.edu.tr - *0000-0003-0062-3817*

Abstract

This study aims to optimize the performance of optical communication and sensing systems using avalanche photodiodes (APD) and transimpedance amplifiers (TIA). The high gain of APDs at low light levels and TIA circuits' wide bandwidth, low noise, and high-speed characteristics are critical for these applications. In the design process, a T feedback network and various operational amplifiers were used to enhance the performance of the TIA circuit. LTspice simulations examined the effects of white noise on the circuit's current and output voltage and the noise performance under various noise divider values. The impact of changes due to laser distance and dark current were also analyzed. These analyses reveal how the TIA circuit achieves high performance in different applications and demonstrates the effectiveness of noise reduction techniques. The results provide significant insights into the design of TIA circuits used in optical communication and sensing systems.

1. INTRODUCTION

Rapid advances in optical communication technologies in recent years have highlighted the importance of optical receivers, crucial components for converting optical signals into electrical signals in communication and sensing systems [1]. A core component of these receivers, the transimpedance amplifier (TIA), is employed in diverse applications, including optical communication (e.g., 2.5, 10, and 25 Gb/s), mechanical sensors, biosensors, DNA sequencing, impedance spectroscopy, and remote sensing [2,3]. This extensive application range introduces various technical challenges for TIA circuit designers, such as achieving GHz-level bandwidth in communication systems while optimizing noise performance in lower-frequency bioapplications [4,5,6]. Furthermore, low power consumption is essential for bio-implantable applications, highlighting the need for high flexibility and performance optimization in TIA design [5,7].

In critical applications, noise signals can interfere with accurate signal detection, especially in low-light environments. For instance, shallow current signals are produced at photodetector outputs in remote sensing applications such as LIDAR (light detection and ranging) [8,9]. TIA circuits, particularly when paired with avalanche photodiodes (APDs), help address these challenges, enabling efficient signal processing in such conditions [10].

---

*Corresponding Author: berkaycavus@gmail.com

TIA circuits also possess other essential features, including wide bandwidth, fast response time, and adjustable gain for application-specific sensitivity. These features are especially valuable in optical communication, where modern TIAs deliver high performance, critical for energy efficiency [5,11]. Additionally, TIAs support APDs to operate effectively, thereby enhancing the performance of optical communication systems and other optoelectronic applications.

Recently, the significance of APD and TIA circuits has increased in optical communication and sensor technologies, including applications like short-range LIDAR sensors with on-chip APDs fabricated using CMOS technology [12]. Such receivers show significant potential, particularly in indoor monitoring applications [13]. In data computing, dense wavelength multiplexing (DWDM) connections have been studied to overcome electronic connection limitations and meet data traffic demands [14]. Moreover, multi-channel analog front-end circuits have been developed for linear LADAR applications, underscoring the critical role of APD and TIA circuits in advancing optical communication and sensor technologies [12,15].

This study aims to design an optimized TIA circuit for APDs that provides high sensitivity, low noise, high speed capabilities and cost-effective performance to meet the increasing demands in optical communication and sensor technologies, and also contributes to the performance of transimpedance amplifiers (TIAs) by addressing several important issues that are often neglected in the existing literature. Simulation analyses evaluate the ability of the circuit to accurately process signals at different frequencies by considering variables such as laser distance and dark current effects. First, the effects of white noise intensities and feedback capacitor values on the performance of the TIA circuit are modeled and a comprehensive analysis is presented. In addition, performance enhancement is achieved under various operating conditions thanks to the noise reduction techniques integrated into the TIA design. In addition, an innovative approach is demonstrated in the TIA circuit design by using a T feedback network and different operational amplifiers. This study, in which variables such as laser distance and dark current effects are evaluated by simulation analyses, examines the ability of the TIA circuit to accurately process signals at various frequencies in detail. These unique contributions make the study stand out from the existing literature and an important step towards meeting the increasing demands in optical communication and sensor technologies at a low cost.

2. MATERIAL AND METHOD

APDs are semiconductor devices that provide high sensitivity and fast response times. Multiplying the electron-hole pairs formed by light photons with the Lavin effect provides substantial signal gains even at low light levels [11]. Excelitas' C30737 series APDs offer high sensitivity, especially at wavelengths between 500 nm and 1000 nm, making them an ideal choice for automotive LIDAR, laser meter, and area scanning applications [16]. When designing a suitable TIA circuit for APDs, attention should be paid to the electrical and optical properties of the APD. This circuit converts the current signal from the APD into a voltage signal [12]. For Excelitas C30737 series APDs, the low bias voltage is necessary for the APD to provide high gain. Additionally, the fast response time (about 200 ps) and low noise level (about 0.1 pA/√Hz) of APD should be considered in TIA circuit design [16]. The wide bandwidth and high sampling rate of the TIA circuit must be compatible with the high cutoff frequency (>1 GHz) of the APD [15].

At wavelengths of 800 nm and 900 nm, the reverse bias voltage directly affects the gain of the APD. For 800 nm, the typical breakdown voltage varies between 120V and 210V, while for 900 nm, this range is between 180V and 260V [16]. The reverse bias voltage should be set at the optimal point higher than these breakdown voltages but before the Lavin effect begins. This provides efficient signal amplification and prevents overheating and device damage [11]. The gain values of the APD also vary depending on the wavelength, so these factors should be considered when choosing the reverse bias voltage [16]. Other essential features to consider in the design of an APD-based TIA circuit include the bandwidth of the

circuit, the sampling rate, and the capacitance of the APD [12]. The capacitance values of Excelitas C30737 series APDs vary depending on the bias voltage, which can affect the bandwidth and noise performance of the TIA circuit [16]. The pulse width of the APD determines the shortest signal duration that can be detected by the system, which is especially critical in applications requiring fast response [15]. The ideal OpAmp selection for TIA circuits depends on the application's requirements. The following OpAmp models are generally preferred for scenarios requiring low noise, speed, and high sensitivity, such as APD applications:

Texas Instruments OPA657, 1.6 GHz gain-bandwidth multiplication, low noise (4.8 nV/√Hz), and 700 V/µs slew rate. In addition to being perfect for high-speed applications and has wide bandwidth [17]. Analog Devices AD8009, 5.175 GHz gain bandwidth multiplication, and 5500 V/µs slew rate. The high slew rate is ideal for high-speed signal processing [18]. Texas Instruments THS3001, 420 MHz, provides bandwidth, low noise, and a 6500 V/µs slew rate. High power output driver and very high rotation speed, compatible with a wide range of loads [19]. Analog Devices LTC6268, with 500 MHz gain bandwidth multiplication and low input bias current in the femtoampere range. High-speed combination with ultra-low input bias current, good compatibility with capacitive loads [20].

At this point, LTC6268 was chosen. The LTC6268 is the operational amplifier in transimpedance circuits designed for APDs. The reasons for this choice stem from the fact that the set of features that the LTC6268 combines are ideal for applications that require high sensitivity and fast response [23]. In addition to these functional advantages, the selection of LTC6268 was also guided by its cost-effectiveness and ease of integration into compact circuit designs. First, the ultra-low input bias current at the femtoampere level enables precise measurements by reducing voltage errors in signals received from high-impedance sensors [20]. Moreover, with its high slew rate of 1.25 V/µs, the LTC6268 can effectively process rapidly changing signals, maintaining integrity under dynamic signal conditions. This model, which comes with a low noise level (4.3 nV/√Hz), makes obtaining clear and sharp signal outputs possible by minimizing noise, especially at low signal levels. Finally, the wide gain bandwidth of 500 MHz delivers the performance required for high-frequency applications, and the LTC6268's compatibility with capacitive loads simplifies the circuit design. These features make the LTC6268 a reliable choice in critical applications such as optoelectronic sensing systems.

The TIA circuit is a circuit with an OpAmp and a feedback resistor. The current input is received from a photodetector or similar sensor. This incoming current is directed to the reverse input of the circuit, where it is converted into a low-impedance voltage signal by the OpAmp using negative feedback. The feedback resistor determines the relationship between output voltage and input current. The larger this resistor, the greater the output voltage the TIA produces. Using the "T feedback network" design for TIA improves the circuit's performance by providing several advantages. The T feedback network is a structure usually consisting of a resistor and two capacitors and when integrated into the OpAmp circuit, provides the following benefits:

- T feedback network is used to extend the bandwidth of the OpAmp. This structure limits the OpAmp's low-frequency gain while providing a flatter gain profile at high frequencies. This helps maintain the signal's integrity, especially in optoelectronic applications that require high-speed processing.
- The T-network allows the OpAmp to handle positive and negative charge capacitances. Thus, it supports the circuit's more stable operation and compatibility with capacitive loads. This stability reduces signal fluctuations and is especially important in applications where dynamic signal changes occur frequently.
- Effectively reduces noise levels and prevents potential emissions. While capacitors help filter unwanted peaks that may occur at high frequencies, the resistor prevents overreactions by slowing down the overall response of the circuit.

- It helps to harmonize the circuit's input and output impedances with other electronic components to which it is connected. This reduces signal loss and provides higher efficiency during data transmission.
- Using the T feedback network allows the OpAmp circuit to operate more comprehensively. This is especially important for sensors operating in various light conditions because the circuit can more accurately process multiple signals.

It should be noted that in designing the T feedback network, the selection of capacitor and resistor values is crucial, as they directly impact bandwidth and noise performance. These values were carefully optimized through iterative simulations to achieve the desired gain and noise reduction levels suitable for high-speed and precision sensing applications. It is integrated with a high-performance OpAmp, such as the LTC6268, which maximizes overall system performance by offering low noise and high stability while increasing the circuit's ability to collect fast data. How accurately TIAs work depends on signal conditioning, linearity, hysteresis, and temperature. Depending on the intended use and environmental conditions, adding extra circuit elements, such as noise-reducing filters, may be necessary for higher accuracy. Active filter techniques or passive filters containing resistors and capacitors can be used on the circuit output to eliminate unwanted signals. A unique amplifier, the TIA, corrects minimal currents in the reverse direction. The designed circuit is shown in Figure 1.
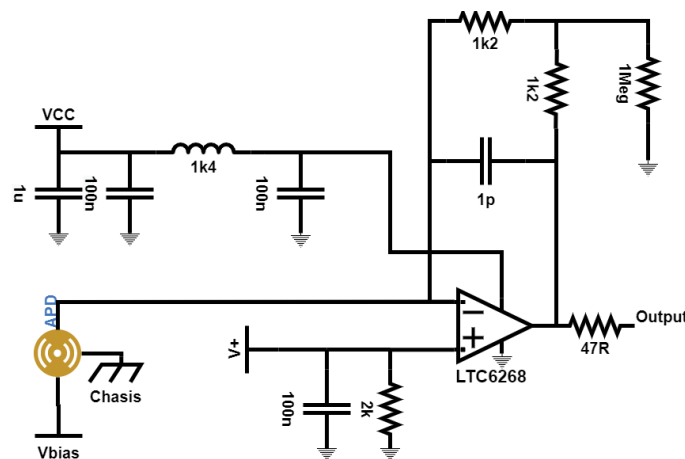
Figure 1. TIA circuit design.

A Ferrite bead is a circuit element whose impedance increases at high frequency. The value "1k4" indicates that the ferrite bead has an impedance of 1.4 kΩ at high frequency. Ferrite bead absorbs high-frequency noise and converts energy into heat, effectively blocking frequencies in the range of 100 kHz to several hundred MHz. In this design, frequencies around 98 kHz and 326 kHz are specifically targeted, as they often correspond to noise generated by switching power supplies (SMPS) and other industrial sources. By filtering out these frequencies, the ferrite bead reduces the impact of switching harmonics and external electromagnetic interference (EMI) on the circuit. This prevents high-frequency noise on the feed line from reaching the operational amplifier. Capacitors are usually added parallel to an operational amplifier's supply leg to further enhance noise suppression. For instance, the combination of 100 nF and 1 uF capacitors in this circuit helps to target different noise bands, with the 100 nF capacitor focusing on higher frequencies (such as 100 kHz and above) and the 1 uF capacitor addressing lower-frequency noise components. This is to filter out high-frequency noise in the feed line. Capacitors direct this noise to the ground by creating a low impedance path at high frequency. Capacitors of different values are used to filter noise in different frequency ranges, effectively isolating sensitive components from noise within the 98 kHz to 326 kHz band, which is commonly associated with external RF interference and switching noise. The block diagram of the designed system is shown in Figure 2.

Figure 2. Block diagram of the system.

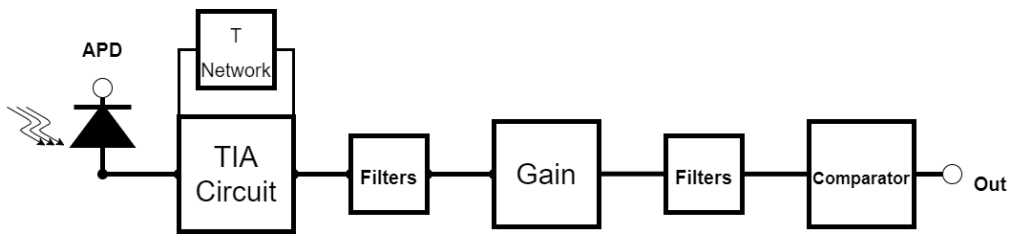Additionally, the APD was supplied with reverse voltage. The use of this reverse bias voltage plays a critical role in maximizing the performance of the APD. Reverse bias reduces the internal capacitance of these detectors, speeding up their response time and increasing their internal gain through the pulse multiplying effect. These features are essential, especially in high-speed and precise optical detection applications. Thus, the combination of reverse bias application and T feedback network enables more accurate and faster processing of signals received from APD or photodiodes, significantly improving the overall system performance.

However, when we try to sample the output voltage obtained only with TIA with the help of MCU, we cannot get sufficient resolution. Therefore, we must add a gain stage to this circuit design to increase the voltage of this output. Operational amplifiers are essential signal-processing components in electronic circuits and typically perform signal amplification functions. The gain factor of an OpAmp is determined by the passive components included in the circuit and acting as a feedback network. In this phase of the study, a non-inverting configuration was used. On the other hand, a non-inverting gain circuit is a configuration in which the input signal is applied to the positive terminal of the amplifier, and the output is realized as a copy of the input signal with the same phase and amplitude. The following equation determines the voltage gain, A_v of this circuit configuration:

$$A_v = 1 + \left(R_f/R_{in}\right) \tag{1}$$

Here, A_v is the voltage gain, R_f is the feedback resistor, and R_{in} is the input resistance. This signal can be routed to an operational amplifier gain circuit to increase the gain of the signal obtained from a TIA output. Feedback and input resistors must be carefully selected in this integration process to achieve predetermined gain values. In this case, our gain is $A_v=11$.
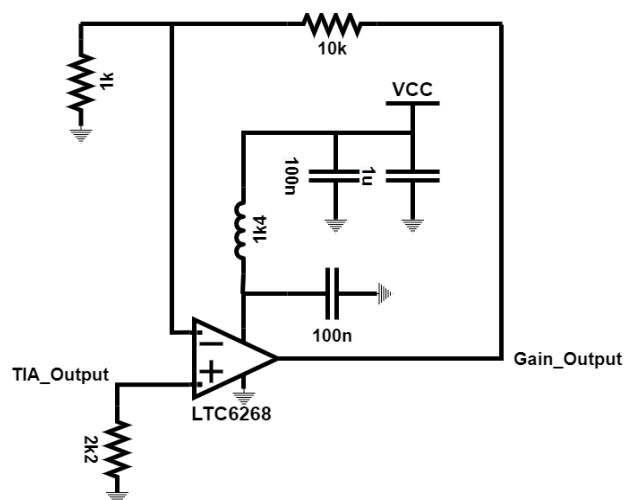

Figure 3. Gain circuit design.

This flyback converter circuit is selected to provide the -60V reverse bias voltage required for driving the APD and is ideal for applications requiring isolated power conversion. In this design, the FQP30N06L MOSFET is driven by a PWM signal to achieve high-speed switching on the primary winding of the transformer. The FQP30N06L was chosen for its low on-resistance and high switching speed, which enhance the converter's efficiency and make it suitable for high-frequency operation. The PWM control circuit ensures accurate timing of the MOSFET switching, providing a stable and continuous output voltage. The transformer not only enables voltage conversion but also adds isolation to improve circuit reliability. On the output side, the Schottky diode (MBR), with its low forward voltage drop and fast recovery time, allows unidirectional current flow with minimal losses at high frequencies. The 150 μF capacitor filters out voltage ripples to establish a stable Vbias output. The 1k and 1R resistors are added to optimize MOSFET operating conditions, limit excessive current, and ensure load stability. In this design, limitations such as the MOSFET's thermal tolerance, the leakage inductance of the transformer, and diode losses have been considered. Additionally, components are selected for their low ESR and high-speed characteristics to ensure efficient operation with minimal losses at high frequencies.
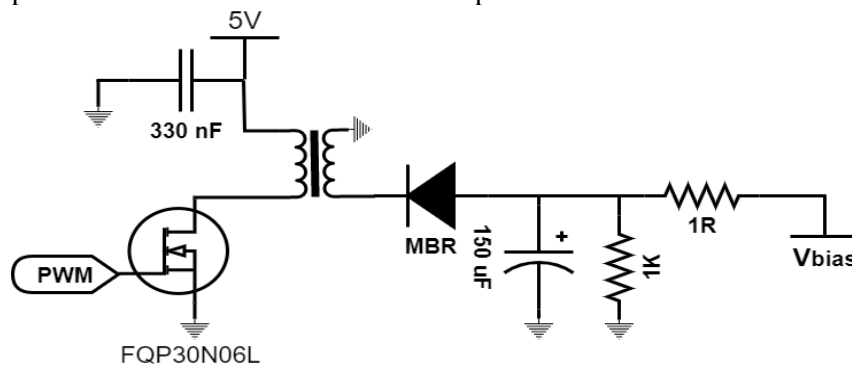
Figure 4. Reverse voltage circuit design

3. SIMULATION RESULTS AND DISCUSSIONS

LTspice v17.1.8 simulation software from Analog Devices was used to analyze the circuit comprehensively. The designed circuit consists of several stages: TIA, gain, and reverse feed. First, the reverse feed stage will be simulated, and its characteristics will be examined.

3.1. Modeling Bias Voltage

The parameters of the circuit analyzed in LTSpice are as follows:
.param D=0.15: This defines the service factor of the converter. The service factor represents the ratio of the time a cycle is "on" to the total cycle time. In this case, 15% of the cycle is set to be "on."
.param Fs=200k: This determines the switching frequency of the converter. In this case, the converter switches at a frequency of 200 kHz.

.param Vin= 24: This determines the input voltage of the converter. In this case, the input voltage is set to 24V.

.step param X 10u 150u 10u: This command defines a parameter sweep for parameter "X." The "X" value varies in steps of 10 microfarads (10u) from 10 microfarads (10u) to 150 microfarads (150u). This could represent a capacitor connected in parallel with the converter, and LTSpice simulates this range to see how it copes with these changes.

Figure 5. Flyback converter circuit PWM response.

The duty cycle (D) and switching frequency (Fs) are key parameters that must be carefully adjusted to ensure efficient operation of the flyback converter. D = 0.15 indicates that the MOSFET is on for 15% of the cycle, allowing the transformer to store and release energy without reaching magnetic saturation. If D = 0, the MOSFET never turns on, resulting in no outp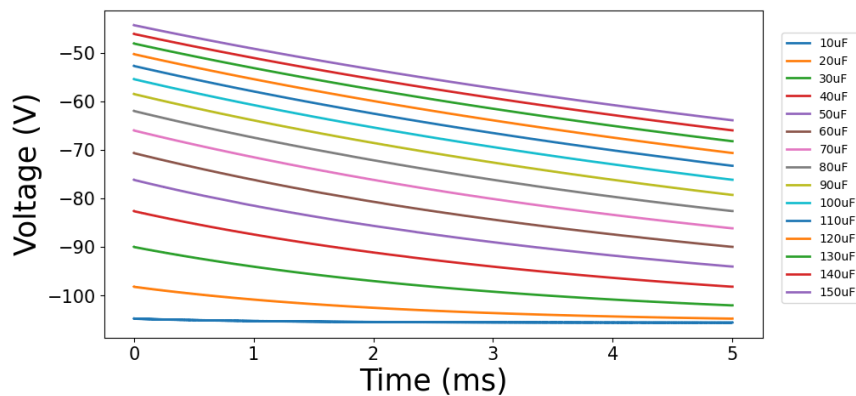ut voltage; if D = 1, the MOSFET remains continuously on, leading to overheating and saturation in the transformer. The Fs value of 200 kHz determines how many times per second the MOSFET switches. While higher frequencies provide faster response times, they also increase heat dissipation and switching losses in the MOSFET and transformer. At lower Fs values, a higher D is possible as the transformer has more time to reset its magnetic field; however, at higher Fs values, a lower D is preferable. This combination optimizes efficiency and achieves stable output voltage. The balance between duty cycle and switching frequency is essential to manage limitations such as transformer saturation, MOSFET heating, and output voltage stability. The Vin and X parameters are critical factors that directly impact the performance and stability of the converter. With Vin set to 24V, the input voltage enables efficient operation; however, excessively high Vin values can cause overheating in components like the MOSFET and transformer, while lower Vin values may limit output power, risking insufficient voltage. The X parameter, representing capacitance connected in parallel to the output, is swept in simulation from 10 µF to 150 µF. As capacitance increases, output ripple decreases, providing a more stable output voltage; however, very high capacitance can slow the circuit's response time and lead to excessive current draw during transients. A balanced choice of these parameters is crucial for ensuring output voltage stability, fast response capability, and thermal durability of the components.

As can be seen from the graph, the response of the circuit driven by the 150 µF capacitor is ideal for TIA. When analyzing the TIA circuit, it will be assumed that the required reverse bias voltage will be given ideally.

3.2. Distance Dependent Iapd Current Modeling

The current falling on the APD varies inversely with the distance of the laser signal. In this project, a 905 nm, 30 mW, 5 V DC IR laser unit with 0-15 kHz TTL modulation (18×45 mm) is used. The 905 nm wavelength falls within the APD's maximum sensitivity range of 500-1000 nm, ensuring high efficiency. Additionally, the 30 mW laser power is sufficient to generate a high photocurrent from the APD; if the laser power were lower, the photocurrent from the APD would decrease, negatively affecting the signal-to-noise ratio, making 30 mW an optimal choice. When the laser illuminates the APD, the current passing through the photodiode depends on the laser's power, the APD's sensitivity, and gain. APDs achieve high gain by multiplying the carriers produced by each photon of incident light. This multiplication process allows currents ranging from nanoamperes to microamperes, depending on the light intensity on the device's surface.

Given the APD's responsivity value of 60 A/W and the laser's output power of 30 mW (i.e., 0.030 W), the APD's high responsivity, combined with high gain, allows even small amounts of incident light to be converted into a high photocurrent. Therefore, the APD is designed to operate with high sensitivity even at low light levels. However, at higher laser powers and gain factors, limitations such as overheating and saturation should be considered, as the APD's thermal capacity could become a limiting factor under these high-power conditions. With these values, we can calculate the current passing through the APD. With these values, we can calculate the current passing through the APD.

$$I = \text{Responsivity} \times \text{Light Power} \tag{2}$$

$$I = 60 \times 0.030 = 1.8 \text{ mA} \tag{3}$$

In this case, the current flowing through the APD will be approximately 1.8 mA. This shows how the light from the laser is detected by the APD and how much photocurrent this light produces. The distance measurement of the laser can also be made from here. To calculate how the photocurrent produced by laser light on a photodiode varies with the distance of the laser from the photodiode, we must consider the light's propagation properties and geometry. As the distance increases, the light coming from the light source decreases as its area expands. This can be explained by the fact that light intensity decreases inversely proportional to the square of the distance (inverse square law).

Calculation:
- Initial Conditions,
- Laser Power, P=30 mW
- APD Responsivity, R=60 A/W
- Current at First Distance, I=1.8 mA

Current-Distance Relationship:
- In the first case, when the laser is very close to the APD, 1.8 mA is obtained with the equation $I=R \times P$.
- As the laser moves away, the effective area of light falling on the APD decreases. As the distance increases by d units, the light intensity decreases by $1/d^2$.

New current (I_d), at distance d:

$$I_d = I + d^2 \tag{4}$$

Here, I is the starting current (1.8 mA), and d is the ratio of the distance of the laser from the APD to the starting distance. This analysis measures the designed circuit's response according to the laser distance. The focal point of the laser we use here is 10 cm. In other words, it is at the maximum current that the APD can see. Here, we will examine how the current through the APD (Iapd) responds to distance changes. Using the LTspice simulation, we will observe how the buffer output, that is, the circuit output, changes step by step by increasing or decreasing the distance of the laser from the APD. This analysis will help us understand the sensitivity of the APD to light sources at various distances and the long-distance sensing capability of our system. Using the ".step" command, this study will enable us to model scenarios encountered in practical applications.

```
.step param IAPD 0u 1.8m 200u
PULSE(0 {IAPD} 0 0.9n 0.9n 20n 200n)
```

In the PULSE command, a PWM signal is defined, starting from 0 µA and going up to 1.8 mA. It has a rise and fall time of 0.9 ns. Additionally, PW is 20 ns, and PRI is 200 ns.

The IAPD parameter is a sweep parameter used to define the APD's output current, varying from 0 µA to 1.8 mA in steps of 200 µA. This range is tested in simulations to observe how different light intensities and gain levels affect circuit behavior under varying conditions. The upper limit of 1.8 mA is set to prevent the APD from overloading or exceeding its thermal capacity, ensuring stable operation. The PULSE command applies a PWM signal to the APD output current, starting at 0 µA and reaching up to the limit defined by IAPD. With a rise and fall time of 0.9 ns, optimized for the Excelitas C30737 APD's rapid response, this setting preserves signal integrity at high frequencies, allowing the APD to handle fast laser pulses efficiently. The pulse width (PW) of 20 ns determines the duration for which the APD signal remains at its peak, suitable for applications requiring quick response. The period (PRI) of 200 ns sets the signal repetition rate, producing a new pulse every 200 ns, which enables the APD to process high-speed incoming signals and maintain the characteristics of the laser pulse in the output. Together, these parameters are optimized to allow the APD to operate effectively under different light conditions and high-speed scenarios, although considerations like thermal noise and heating at high frequencies may impose limitations on performance.
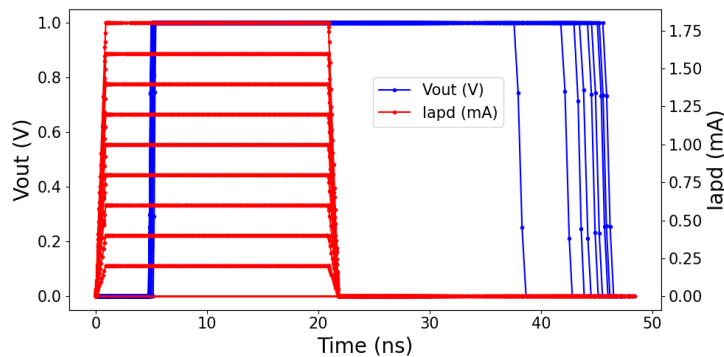
Figure 6. Relationship between 22 ns PW and laser distance

The graph in Figure 6 shows the current coming to the APD according to the laser distance and, accordingly, the voltage in the buffer at the output of the circuit. It is observed that when a 22 ns PW signal is sent, the current takes different values, and therefore, the output voltage in the buffer changes. The blue line shows the voltage (V) and progresses at a constant value on the time (ns) axis. The red line shows the current (mA) and fluctuates at different levels on the time axis. It is observed that the current takes different values and changes in direct proportion to the distance of the laser. As the current increases (for example, as the laser approaches the APD), the current value increases and vice versa. While the output voltage at the buffer is expected to remain at a constant value when a 22 ns PW signal is sent, it sometimes varies for longer or shorter periods than this period. This is due to the circuit's response to different current levels.

Figure 7. Iapd response of the TIA

As the distance of the laser from the APD increases, the current value decreases, and as the distance decreases, the current value increases. The initial current is given as 1.8 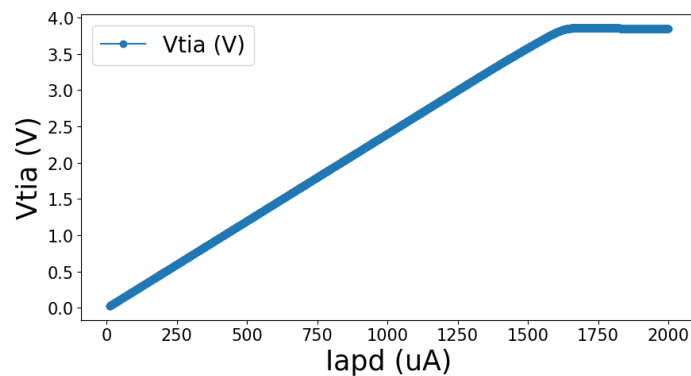mA, and the graph shows that the current varies at different distances. The change in current directly affects the output voltage in the buffer. More significant fluctuations in the output voltage are observed, especially at higher current values (when the laser is close to the APD). This shows that the circuit's responses to current levels differ and cannot provide a constant output voltage against these changes. If we do the DC analysis of Iapd,

.dc Iapd 0 2m 10u

The .dc Iapd 0 2m 10u command is used to perform a DC analysis of the APD current (Iapd). This command varies the Iapd value from 0 µA to 2 mA in 10 µA steps. This range is chosen to simulate the intensity of laser light received by the APD at different distances and to understand how current variations affect the output voltage. The 0 µA starting value represents a scenario where the laser light does not reach the APD or is very distant, while the 2 mA upper limit approximates the maximum detection range of the APD, simulating the highest current level when the laser is very close to the APD. This upper limit is also chosen to be close to the ±2 mA input current limit of the LTC6268 op-amp, ensuring the stability and safety of the op-amp. The 10 µA step analysis allows for capturing fine details of the relationship between the distance of the laser to the APD, the resulting current, and the output voltage, particularly observing how the circuit responds to higher current values (closer distances). This DC sweep analysis provides a detailed evaluation of how current changes affect the circuit's voltage output, revealing the circuit's capability to maintain a stable voltage under varying light conditions.

In the graph in Figure 7, as the input current, that is, the current passing through APD, increases, the output voltage of the TIA circuit reaches DC saturation. After 1.7 mA, the output voltage settles at 3.7 V. This coincides with the characteristics of APD. The maximum current passed by the APD is calculated as 1.8 mA and is related to the power of the pulsed laser. According to the analysis, APD saturates at small distances and focal points from the focal point of APD. Therefore, in such cases, PW measurement is performed incorrectly.

3.3. PW and PRI Analysis

PW is the duration of the laser pulse and is usually measured in nanoseconds or microseconds. Pulse width affects the pulse's energy and, therefore, its level of detectability. Pulse width can directly affect data transmission speed and resolution. PRF refers to the number of pulses sent in one second, measured in Hz. PRF determines the system capacity and data transmission rate. High PRF provides fast data transmission but is limited to shorter sensing distances because the inter-pulse time is shortened. PRI is the time interval between two consecutive laser pulses. PRI helps determine the detection distance and speed of the target defined by the system. When long distances need to be detected, longer PRI values are generally used.

In optical communications, especially in applications such as LIDAR, these parameters determine how quickly and effectively laser pulses can detect targets and data transmission efficiency. For example, faster scanning can be done in a LIDAR system using high PRF, which is advantageous in rapidly changing conditions such as moving vehicles. However, higher PRF may result in shorter-range detection because the system may not receive a response quickly enough before sending the next pulse. Conversely, long PRI allows the detection of greater distances but reduces the speed of data collection. Therefore, setting these parameters appropriately depending on the system requirements is critical. Balanced optimization of these parameters in pulse laser systems in optical communication is essential for maximum efficiency and performance.
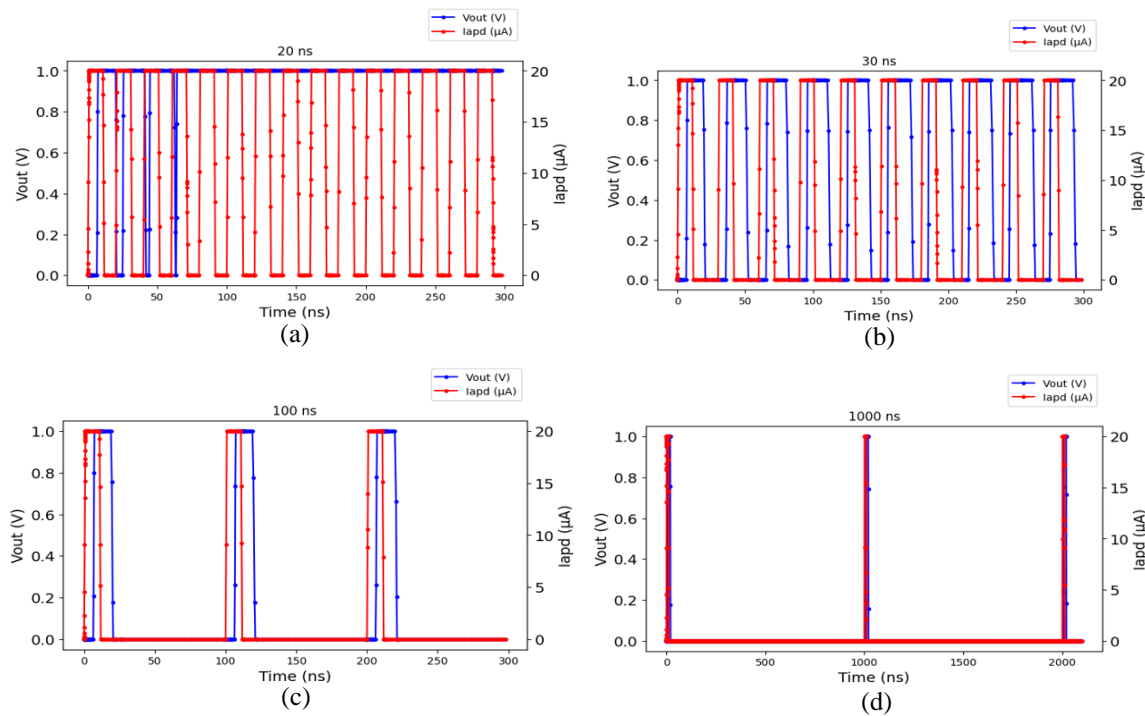
Figure 8. Pulse reputation interval, (a) 20; (b) 30; (c) 100; (d) 1000 ns

The PULSE command parameters, PW (Pulse Width) and PRI (Period), were carefully selected to determine the stable and unstable operating limits of the TIA circuit. The PW value is set to 10 ns, which is suitable for high-speed applications where the TIA circuit needs to detect laser signals quickly. However, if the PW value is too short, it may hinder the signal processing by not allowing enough energy to accumulate within the circuit. The PRI value, on the other hand, allows the circuit to complete its energy processing and prepare for the next pulse. By using different PRI values, such as 20 ns, 30 ns, 100 ns, and 1000 ns, a range was established in which the TIA circuit shows instability at lower PRI values and stability at higher ones. At a PRI of 20 ns, distortions in the output signal were observed due to insufficient time for the circuit to stabilize, whereas a PRI of 30 ns resulted in more regular and periodic pulses. With longer PRI values of 100 ns and 1000 ns, the circuit produced completely stable and smooth outputs, with the 1000 ns PRI delivering the most consistent and stable signals. These results reveal that the TIA circuit exhibits instability at short PRI durations but provides reliable performance at higher PRI values. Therefore, the PULSE command parameters were chosen to cover a broad range, from the lower PRI values, where the circuit shows instability, to the higher PRI values, where it produces stable results. This selection established an operational frame within which the circuit can maintain a stable output voltage.

The ".step param PW 5n 155n 50n" command was used to analyze the response of the TIA circuit based on varying pulse width (PW) values. In each simulation step, the PW parameter is set to 5 ns, 50 ns, and 155 ns to observe how the circuit behaves across different operating conditions. The 5 ns PW value represents a very short pulse width, chosen to test the circuit's response under high-speed conditions where signal processing time is limited. At this low PW, the circuit may not have sufficient time to accumulate and process energy, potentially leading to output distortions. The 50 ns PW is an intermediate value that provides a more stable operation, allowing the circuit adequate time for signal processing and reducing output irregularities. This setting represents a transition point between unstable and stable operation. The 155 ns PW represents a high pulse width, giving the circuit ample time to process the signal and produce the most stable and accurate output. This range of PW values, spanning

from 5 ns to 155 ns, was selected to cover the frame in which the TIA circuit transitions from unstable to stable operation, thereby identifying the conditions under which the circuit provides the most reliable output. Through this analysis, the optimal PW range for stable voltage output and the limits of instability at shorter PW values were determined.
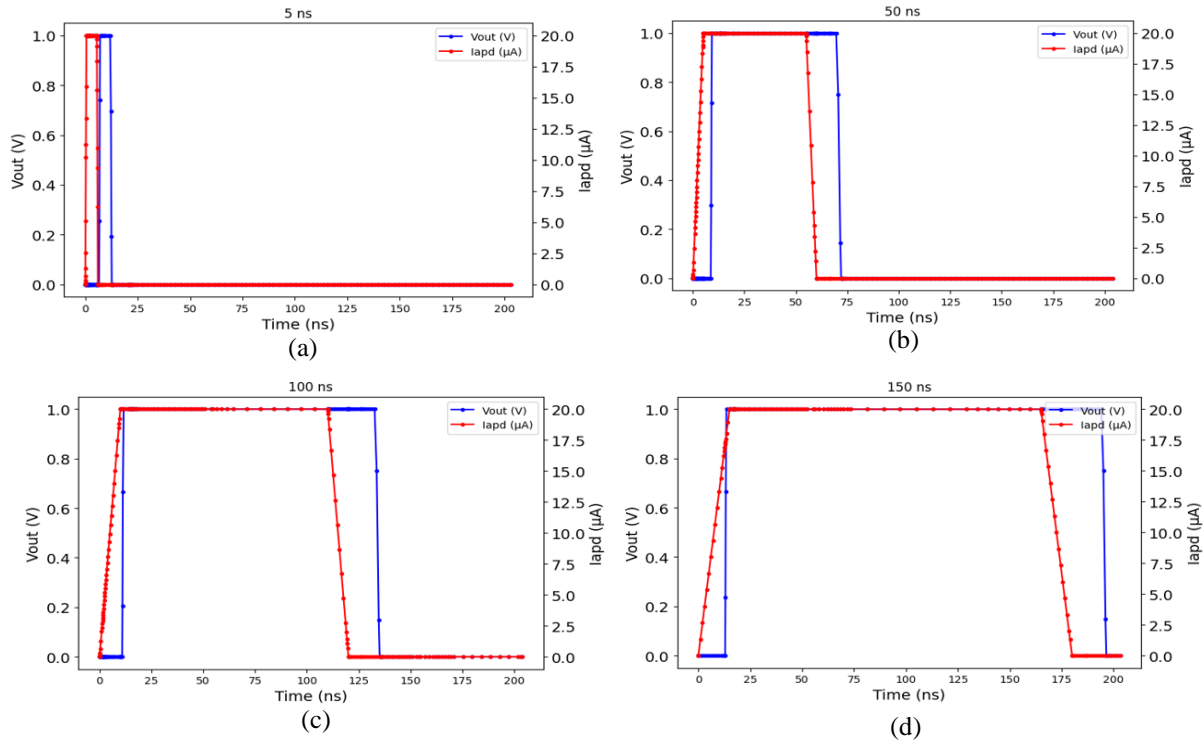
Figure 9. Pulse width, (a) 5; (b) 50; (c) 100; (d) 150 ns

Figure 9 shows the effects of the circuit on the output voltage (Vout) and the current from the APD (Iapd) when the PW parameter is set to 5, 50, 100, and 150 ns. The blue lines in the graphs represent Vout, and the red lines represent Iapd. At 5 ns PW (upper left graph), Vout rises and falls rapidly, and Iapd synchronously exhibits the same behavior without any degradation, indicating a fast circuit response. At 50 ns PW (upper right graph), Vout produces a longer pulse, and Iapd works accordingly correctly. At 100 ns PW (bottom left graph), the Vout signal remains high for more extended and Iapd again rises and falls in line with Vout. At 150 ns PW (bottom right graph), Vout generates the longest pulse width, and even then, the Iapd signal operates smoothly without significant degradation. This analysis allows us to observe the circuit's response at different values of the PW parameter. It shows that the output voltage (Vout) and the current (Iapd) signals from the APD are compatible and stable at each pulse width. As a result, the TIA circuit exhibits stable performance at various pulse widths. It works appropriately even at high frequencies, proving that it is designed to meet high-performance requirements in optoelectronic applications.

3.4. Dark Current Modeling and Analysis
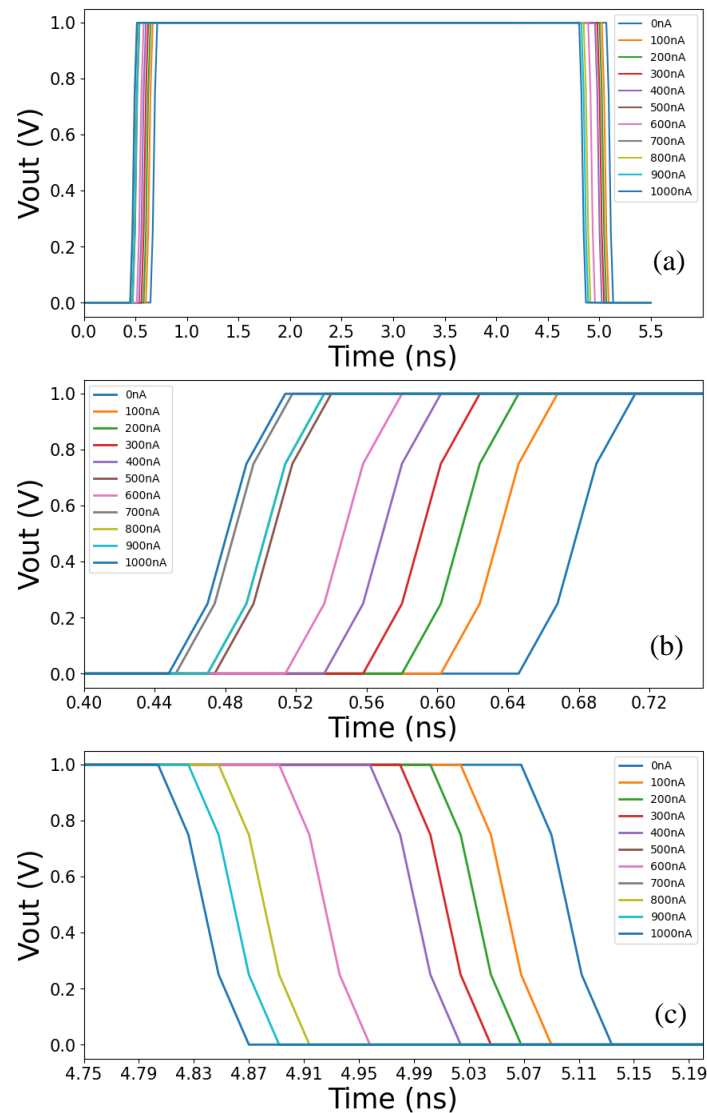
Figure 10. Dark current analysis of the APD, (a) full scale; (b) around 0.5 ns; (c) around 5 ns

The effects of the amount of dark current on the performance of the APD and TIA circuit will be examined in this section. We will analyze the circuit's reaction to these changes by changing the dark current value with the ".step" command on LTspice. Control of dark current is essential to minimize noise and maximize signal integrity, especially at low signal levels. Dark current values range from nanoampere, nA to microampere, μA. Especially in APDs designed for low-light applications, dark current values are tried to be kept lower. Typically, in silicon-based APDs, dark current values can range from a few nA up to 100 nA. However, these values can increase to microamperes at high gain settings or temperatures. The step command sets dark current values between 0 nA and 1000 nA to observe the performance of the APD circuit under both low and high dark current conditions. Dark current in APDs typically ranges from as low as 0.05 nA up to several μA; therefore, a broad range from 0 nA to 1000 nA is included in the simulation. Low dark current values are chosen to test the APD's sensitivity for precise signal detection, while higher values allow examination of potential reductions in signal

sensitivity and possible noise increases. This range provides an operational framework in which the circuit responds with stability and sensitivity at lower levels, while stability is tested at higher levels.

Figure 10 shows the response of the APD and TIA circuits with various dark current values on the time (ns) and voltage (V) axes. The graph shows the voltage changes for different dark current levels (0, 100, 200…,1000 nA). The effect of different dark current levels is observed in the graph. Each colored line represents a specific level of dark current. Voltage values increase and decrease quickly, showing that the circuit responds quickly. The time axis is in ns, indicating that responses occur quickly. As dark current values increase, very slight differences are observed in the voltage curves. While voltage changes are more noticeable, especially at low levels, these changes become less evident at high levels. As dark current levels increase, a slight deviation in the voltage response of the APD and TIA circuits is observed. This shows that dark current can affect the overall performance of the circuit. The circuit's response is quite sensitive for low dark current levels (e.g., between 0nA and 100nA), and a significant voltage change is observed. This highlights the importance of keeping dark current to a minimum at low signal levels. At higher levels (e.g., 900 to 1000 nA), less pronounced changes in voltage response are observed. This suggests that high dark current levels can reduce the circuit's sensitivity and potentially increase noise levels.

3.5. Bode Diagrams of The Circuit

Bode diagrams were generated to analyze the frequency response of various circuit layers. This analysis shows the effect of filter circuits and gain stages throughout the system and their frequency-dependent behavior. Bode diagrams are an excellent tool for understanding frequency-dependent changes critical in circuit design.
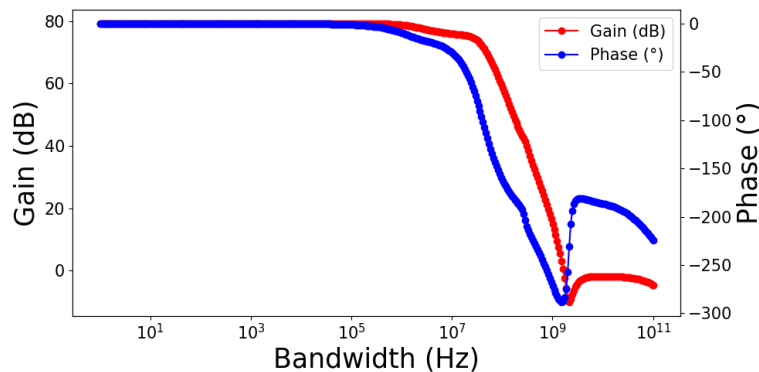

Figure 11. TIA with T-network AC analysis gain and phase graph

Figure 11 shows the gain in dB versus frequency for a TIA equipped with a T-network. In this graph, the gain curve is represented in red. This analysis is essential to understanding the T-network's effect on the TIA circuit's gain performance in different frequency ranges. In the low-frequency region (10 Hz-1 kHz), the gain remains constant at approximately 80 dB. There is no significant change in gain as the frequency increases. This shows that the TIA circuit provides a high and stable gain at low frequencies. In the mid-frequency region (1 kHz-10 MHz), the gain remains constant at approximately 80 dB. There is no decrease in earnings in this range either. It appears that the T-network preserves the gain of the TIA circuit in this frequency range. In the high-frequency region (10 MHz-1 GHz), the gain drops dramatically to 0 dB; after 1 GHz, the gain decreases further. The observed decrease in gain indicates that the performance of the TIA circuit decreases rapidly at very high frequencies. The gain decreases rapidly in the high-frequency region (1 GHz and above), dropping to approximately -10 dB and approaching 0 dB again. It is understood that the TIA circuit has difficulty providing gain in this frequency range, and its performance decreases significantly. However, this decay curve in the graph

shows that the T-network does not entirely lose the gain, or very little, even at very high frequencies, providing an increase of approximately 0 dB.

Figure 11 also shows the change in phase angle versus frequency for a TIA equipped with a T-network. In this graph, the phase curve is represented in blue. This analysis is essential to understand the T-network's effect on the TIA circuit's phase response in different frequency ranges. In the low-frequency region (10 Hz-1 kHz), the phase angle remains constant at approximately 0 degrees. This shows that the TIA circuit can effectively control the signal phase at low frequencies. In the mid-frequency region (1 kHz-10 MHz), the phase angle remains constant at approximately 0 degrees. No phase shift is observed in this range. It appears that the T-network maintains the phase performance of the TIA circuit in this frequency range. The phase angle decreases in the high-frequency region (10 MHz-1 GHz). A negative shift in phase angle is observed in this range. After 1 GHz frequency, the decrease in phase angle becomes more pronounced and decreases to approximately -280 degrees. This suggests that the TIA circuit has difficulty controlling the signal phase at high frequencies. When we look at the phase angle movements in the very high-frequency region (1 GHz and above), it increases rapidly up to -180 degrees. Then, it decreases quickly to approximately -250 degrees at 100 GHz. In this frequency range, the phase shift of the TIA circuit increases significantly. However, this curve in the graph shows that the T-network can partially control the phase shift even at very high frequencies.
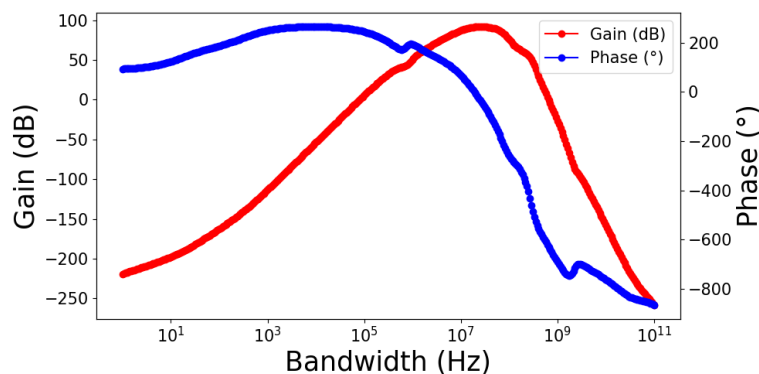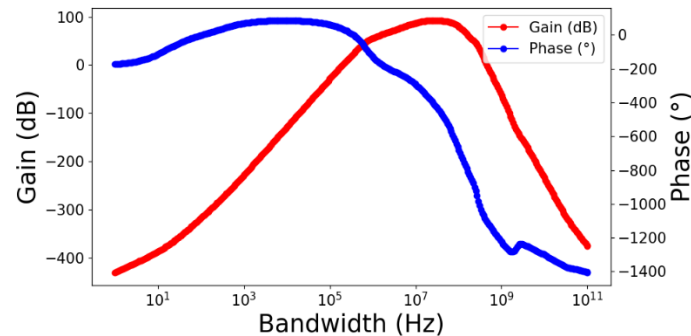

Figure 12. Gain and phase graph of the gain part of the circuit

Figure 12 shows the gain versus frequency of a gain stage in dB. In this graph, the gain curve is represented in red. This graph helps us understand how the circuit performs in different frequency ranges. The gain is meager in the low-frequency region (10 Hz-1 kHz), starting from approximately -200 dB. As the frequency increases, the gain rises slowly. This shows that the circuit cannot provide sufficient gain at low frequencies. The gain increases significantly in the mid-frequency region (1 kHz-10 MHz). In this frequency range, the gain characteristic of the TIA progresses towards optimum signal processing capability. In this region, the circuit's performance improves significantly. The 10 MHz-100 MHz frequency region, the gain reaches its peak and maximum level. The maximum gain is approximately 100 dB. This shows that the circuit provides the highest performance in this frequency range. It appears that it is in this frequency range that it can process signals most efficiently. The gain decreases again in the frequency region of 100 MHz and above. As the frequency increases further, the gain decreases. This means the circuit's performance decreases at very high frequencies and has difficulty providing gain.

Figure 12 also shows the change in the phase angle of a gain stage versus frequency. In this graph, the phase curve is represented in blue. This analysis is essential to understand the phase response of the circuit in different frequency ranges. The phase angle starts at a positive value in the low-frequency region (10 Hz-1 kHz) and increases slowly. As the frequency increases, small increases in phase angle are observed. This shows that the circuit can control the signal phase at low frequencies. The change in

phase angle becomes more evident in the mid-frequency region (1 kHz-10 MHz). The phase angle reaches a maximum of approximately 200 degrees. In this range, the circuit appears to follow the signal phase adequately, and the phase shift is relatively under control. The phase angle decreases to negative values in the high-frequency region (10 MHz-10 GHz). The decrease in phase angle indicates that the circuit has difficulty controlling the signal phase at high frequencies. In this region, the phase shift becomes evident and decreases to approximately -750 degrees. In the high-frequency region (10 GHz and above), the phase angle decreases rapidly and drops to approximately -800 degrees. This shows that at very high frequencies, the phase shift of the circuit is very severe and cannot correctly follow the signal phase.

Figure 13. Gain and phase graph of the comparator part of the circuit

Figure 13 shows the gain of a comparator circuit output versus frequency in dB. In this graph, the gain curve is represented in red. This analysis is essential to understand the gain performance of the circuit in different frequency ranges. The gain is meager in the low-frequency region (10 Hz-1 kHz), starting from approximately -400 dB. As the frequency increases, the gain rises slowly. This shows that the comparator circuit output cannot provide sufficient gain at low frequencies. The gain increases significantly in the mid-frequency region (1 kHz-1 MHz). In this frequency range, the gain rises to approximately 50 dB. In this range, the comparator circuit output appears to reach its optimum signal processing capacity. The gain reaches its peak and maximum level in the 1-100 MHz frequency region. The maximum gain is approximately 100 dB. This shows that the circuit provides the highest performance in this frequency range. It is understood that in this frequency range, the comparator circuit output can process the signals most efficiently. The gain decreases again in the frequency region of 100 MHz and above. As the frequency increases further, the gain decreases. This means the circuit's performance decreases at very high frequencies and has difficulty providing gain.

Figure 13 also shows the change in the phase angle of a comparator circuit output against frequency. In this graph, the phase curve is represented in blue. This analysis is essential to understand the phase response of the TIA circuit at different frequency ranges. The phase angle starts at a negative value in the low-frequency region (10 Hz-1 kHz) and decreases slowly. As the frequency increases, small changes in the phase angle are observed. This shows that the circuit can control the signal phase at low frequencies. The change in phase angle becomes more evident in the mid-frequency region (1 kHz-10 MHz). The phase angle increases to approximately 0 degrees. In this range, the comparator circuit output follows the signal phase properly, and the phase shift is relatively under control. In the high-frequency region (10 MHz-10 GHz), the phase angle decreases again and drops to negative values. The decrease in phase angle indicates that the circuit has difficulty controlling the signal phase at high frequencies. In this region, the phase shift becomes evident and decreases to approximately -1300 degrees. The phase angle decreases rapidly in the high-frequency region (10 GHz and above) and drops to approximately -1400 degrees. This shows that at very high frequencies, the phase shift of the comparator circuit output is very severe and cannot correctly follow the signal phase.

3.6. Modeling and Analysis of Noise

In this analysis, different noise divider (ND) values were chosen to observe the impact of noise on circuit performance. These values were incrementally reduced from high noise levels to low noise levels, creating a framework that spans from erroneous circuit responses to stable performance. ND values of 5000, 7000, 9000, and 10000 were selected, and measurements were taken at these levels. These values were chosen to understand how noise affects the circuit, at which levels it adversely impacts performance, and where acceptable results are achieved. High ND values (such as 100000) were used to minimize the effects of noise and observe the circuit's performance under ideal conditions. To analyze the impact of noise on the circuit, white noise at 2 terahertz was applied and scaled by a specific factor. This design framework aims to assess the circuit's sensitivity to both low and high noise levels, thereby evaluating the effectiveness of suitable noise reduction techniques.

In the last heading, we will examine the effects of the noise added to the system on the output of the circuit depending on distance changes. This analysis will enable us to model the impact of possible noise sources on circuit performance in real-world conditions and evaluate the effectiveness of various noise reduction techniques. In this study, which we carried out using LTspice, we examined the noise effects on the circuit's input current and output voltage under various white noise intensity values. The PRI value was kept constant using the pulse signal created with the "PULSE(0 20u 0 0.9n 0.9n 10n 40n)" command. To add noise, the expression "V = (white(2e12 * time) / ND)" was used, and noise divider (ND) values were determined as 5000, 7000, 9000, and 10000, and measurements were taken for these values. White noise was at a frequency of 2 terahertz and was added to the current source by scaling with different noise divider values. Mathematically, the standard deviation of this noise is calculated by multiplying the power density of the white noise by time and scaling by a particular factor.

$$\sigma_{noise} = \sqrt{PSD \times \Delta f \times t} \tag{5}$$

$$\sigma_{noise} = \frac{1}{GB} \times \sqrt{2 \times 10^{12} \times t} \tag{6}$$

In Equation (5) above, PSD is the power spectral density, and Δf is the frequency bandwidth. σ_{noise} is the standard deviation of the noise. For noise divider values, the standard deviations of white noise at a given time were calculated in Table 1.

Table 1. Standard deviation values according to ND (noise divider) values

| ND	σ_{noise}
5000	282.8
7000	202.0
9000	157.1
10000	141.4
20000	70.7
30000	47.1
40000	35.4
100000	14.1

These calculations show the standard deviation of white noise at a specific time instant (1 second). As can be seen, as the noise divider value increases, the standard deviation of white noise decreases, and the noise effect remains at lower levels. This provides more regular and stable results at high noise divider values. Additionally, an analysis was made according to these ND values, and the results were observed. LTspice commands used:

PULSE(0 20u 0 0.9n 0.9n 10n 40n) generates a pulse signal with a peak value of 20 µA. PW is 10 ns, and the period is 40 ns.

V = (white(2e12 * time) / ND), adds white noise. The expression "white(2e12 * time)" creates white noise at a frequency of 2 terahertz, and the ND value scales this noise.

I = I(Iapd) + V(NOISE) adds white noise to the stream from the APD. The expression represents the noise voltage V(NOISE).

As seen in Figure 14, severe distortions were observed at the output of the circuit at low noise divider values (5000 and 7000), and the desired smooth pulses could not be obtained. Voltage and current graphs are irregular and highly affected by noise. The output showed more regular and periodic pulses at higher noise divider values (9000 and 10000), but there was still a significant noise effect. It continued to show more regular and periodic pulses at the noise divider values of 20000 and 30000, but a completely clean output signal could not be obtained. Likewise, voltage and current graphs are irregular and highly affected by noise. When we further increase the noise divider values (40000 and 100000), we finally see that the output signal shows more regular and periodic pulses. These results show that the circuit does not show the desired performance at low noise divider values, and severe distortions occur. However, more stable and smooth results are obtained at high noise divider values. The output signal exhibits more regular and periodic pulses at the noise divider values of 40000 and 100000. This indicates that higher noise divider values significantly improve the circuit's performance, reducing the impact of white noise. With the addition of white noise, changes in the system's performance became more evident, and the sensitivity of the TIA circuit to noise was analyzed. This analysis highlights the need to consider noise effects when designing and implementing the TIA circuit to achieve optimal performance.
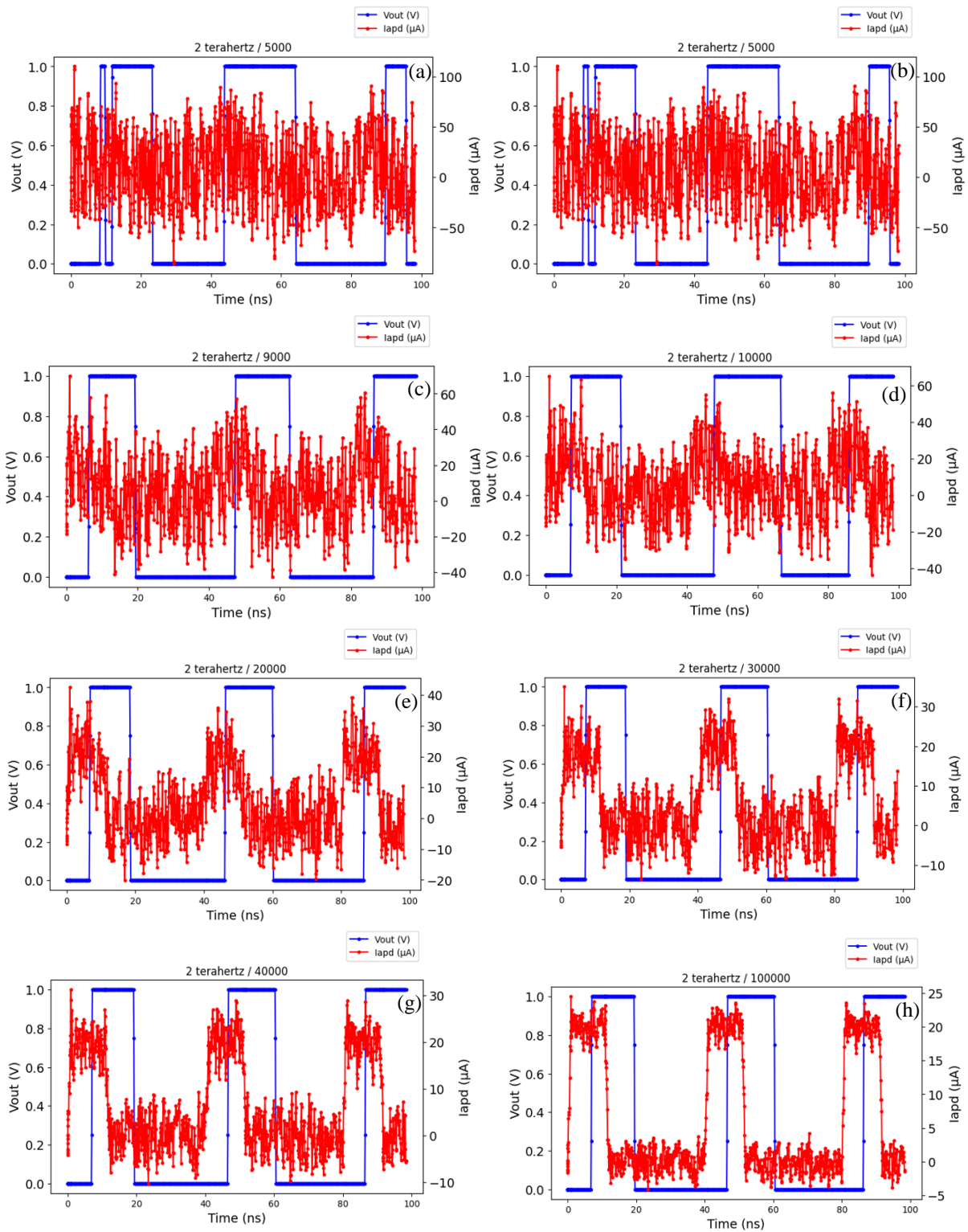
Figure 14. TIA's white noise response, (a) 2 THz/5000; (b) 2 THz/7000; (c) 2 THz/9000; (d) 2 THz/10000; (e) 2 THz/20000; (f) 2 THz/30000; (g) 2 THz/40000; (h) 2 THz/100000.

3.7. Feedback Capacitor Analysis

In this section, the reactions of the circuit output according to the values of the feedback capacitor in the TIA circuit have been analyzed. This analysis was performed using the .step param TC 1p 5p 1p command. In this analysis, different feedback capacitor values in the TIA circuit were used to observe their effects on the circuit output. The ".step param TC 1p 5p 1p" command was employed to vary the capacitor value between 1 pF and 5 pF in 1 pF steps, allowing for an analysis of the circuit's response. These values were chosen to examine how the TIA circuit responds across a range of low to high capacitance levels. Low capacitor values provide a faster response time but may reduce output stability, while higher capacitor values make the circuit more stable but slow down its response time. Thus, the feedback capacitor values were selected within a broad range to identify the stable and unstable operating limits of the circuit. This framework enables the determination of optimal feedback capacitance values for achieving the best output performance in the circuit.
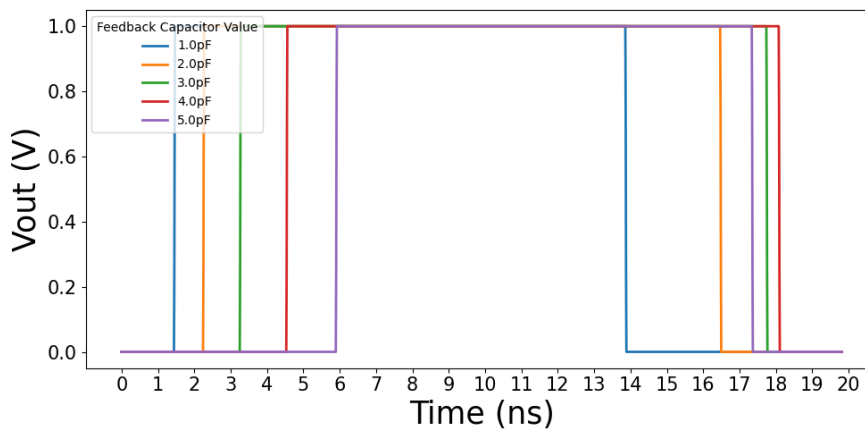
Figure 15. T-network capacitor response

Within the feedback capacitor analysis scope, the feedback capacitor's value in the T-network was calculated parametrically, and the input and output pulse widths (PW) were examined using these values. The colored lines in the graph in Figure 15 show the voltage changes corresponding to each capacitor value. These results demonstrate how the feedback capacitor value affects the pulse width and, thus, the system performance. The graph shows voltage changes on the time axis for different feedback capacitor values (1.0 pF, 2.0 pF, 3.0 pF, 4.0 pF, and 5.0 pF). It was observed how the pulse width changed for each capacitor value. According to the analysis results, narrower output pulses are obtained with lower feedback capacitor values (1 pF), while the output pulse width increases with higher capacitor values (5 pF). This shows that optimizing the feedback capacitor value is critical for system performance. By selecting the appropriate value of the feedback capacitor, the TIA circuit can achieve the desired performance. This study highlights the effect of feedback capacitor value on pulse width and provides an essential basis for determining the optimal capacitor value. This analysis applied a 0.9 ns rise, 0.9 ns fall, and a 10 ns wide pulse to the input, resulting in a total PW of 12 ns. In this case, a 12 ns pulse width at the output was provided with a 1 pF feedback capacitor, and the suitability of this capacitor for the circuit was measured.

The capacity of the TIA circuit to convert weak signals from APDs into electrical signals with high accuracy has been successfully demonstrated. A high-performance TIA circuit is designed for optical communication and sensing systems, providing wide bandwidth, high gain, and low noise performance. It has been observed that the circuit can produce stable and regular pulses at high PRI values. At low PRI values, serious deteriorations in circuit performance were observed, and the desired smooth pulses

could not be obtained. It has been determined that at low noise divider values, the performance of the circuit is negatively affected by the noise effect, and the output signals are irregular. It has been found that optimization of the feedback capacitor plays a critical role in pulse width and system performance.

The developed TIA circuit offers promising results for high-performance optical communication and sensing systems applications. This circuit seems to be used primarily in applications requiring high sensitivity, low noise, and wide bandwidth. Optimizing and testing the design in various real-world conditions will provide an essential basis for future research. The findings of this study provide vital information for the development of optical communication and detection systems and contribute to technological advances in this field. In the design and applications of the TIA circuit, parameters such as optimization of the feedback capacitor value, effects of white noise, and correct selection of PRI values are critical. These findings provide a promising roadmap for developing high-performance TIA circuits in optoelectronic systems. Future studies may further improve the performance of the TIA circuit by examining and optimizing these parameters in more detail and enabling its integration into broad application areas.

4. CONCLUSION

The bias voltage was modeled using a flyback converter circuit in LTSpice with the following parameters: duty cycle of 15%, switching frequency of 200 kHz, and input voltage of 24 V. The circuit's response driven by a 150 μF capacitor was ideal for the TIA circuit. The current through the APD was modeled based on the distance of the laser signal. Using a responsivity value of 60 A/W and a laser power of 30 mW, the current was calculated to be 1.8 mA. The current decreased with increasing distance according to the inverse square law. The effects of pulse width (PW) and pulse repetition interval (PRI) on the circuit's output were analyzed. Measurements were taken for PRI values of 20, 30, 100, and 1000 ns. More stable pulses were observed at higher PRI values. The pulse widths analyzed were 5, 50, 100, and 150 ns, showing stable performance at all values. The effect of dark current on the APD and TIA circuit was examined by varying the dark current values from 0 to 1000 nA. Voltage changes were more noticeable at lower dark current levels, indicating the circuit's sensitivity to dark current. The gain and phase response of the TIA circuit with a T-network was analyzed using Bode diagrams. The gain remained constant at approximately 80 dB from 10 Hz to 10 MHz but decreased significantly at higher frequencies. The phase response remained steady at approximately 0 degrees from 10 Hz to 10 MHz, then decreased to -280 degrees at 1 GHz and to -250 degrees at 100 GHz. The impact of white noise on the circuit's performance was analyzed by adding noise with different noise divider values of 5000, 7000, 9000, 10000, 20000, 30000, 40000, and 100000. Higher noise divider values resulted in more stable and periodic pulses, reducing the noise effect on the circuit. The value of the feedback capacitor in the TIA circuit varied from 1 pF to 5 pF to analyze its effect on the pulse width and system performance. Lower feedback capacitor values resulted in narrower output pulses, while higher values increased the pulse width. This showed the importance of optimizing the feedback capacitor value for system performance.

CONFLICT OF INTEREST

The authors stated that there are no conflicts of interest regarding the publication of this article.

AUTHORSHIP CONTRIBUTIONS

Berkay ÇAVUŞ: Circuit Modeling, Circuit Design, Methodology, Visualization, Writing – original draft. **Şekip Esat HAYBER:** Supervision, Writing – review & editing.

REFERENCES

[1]   Agrawal GP. Optical Communication: Its History and Recent Progress, in Nonlinear Fiber Optics, 6th ed., Academic Press, 2020, 180.

[2]   Romanova A and Barzdenas V. A Review of Modern CMOS Transimpedance Amplifiers for OTDR Applications, Electronics, 2019; vol. 8, no. 10, 1073.

[3]   Grieshaber D, MacKenzie R, Vörös J and Reimhult E. Electrochemical Biosensors - Sensor Principles and Architectures, Sensors, 2008; vol. 8, no. 3, 1400-1458.

[4]   Analog Devices, Stabilize Your Transimpedance Amplifier, Analog Devices Resources, 2021.

[5]   Shahdoost S, Bozorgzadeh B, Medi A and Saniei N. Design of low-noise transimpedance amplifiers with capacitive feedback, Analog Integrated Circuits and Signal Processing, 2014; vol. 80, no. 1, 89-99.

[6]   Texas Instruments, Transimpedance Amplifier Noise Considerations, Technical Articles, 2021.

[7]   Lim B and Park SI. Fully Implantable Low-Power High Frequency Range Optoelectronic Devices for Dual-Channel Modulation in the Brain, Sensors, 2020; vol. 20, no. 13, 3639.

[8]   Bakar AAA, Chellappan K and Chang TG. Surface Electromyography Signal Processing and Classification Techniques, Sensors, 2013; vol. 13, no. 9, 12431-12466.

[9]   Wang Y, Li X, Xu D and Yao J. Gluing Atmospheric Lidar Signals Based on an Improved Gray Wolf Optimizer, Remote Sensing, 2023; vol. 15, no. 15, pp. 3812.

[10]   Li B, Wang W, Yang Y and Li Z, Waveguide-Integrated Ge/Si Avalanche Photodiode with Vertical Multiplication Region for 1310 nm Detection, Photonics, 2023; vol. 10, no. 7, 750.

[11]   Ruskowski J, Ligges M and Grabmaier A. Analytical Evaluation of Signal-to-Noise Ratios for Avalanche- and Single-Photon Avalanche Diodes, Sensors, 2021; vol. 21, no. 8, 2887.

[12]   Joo J-E, Lee M-J and Park SM, A CMOS Optoelectronic Receiver IC with an On-Chip Avalanche Photodiode for Home-Monitoring LiDAR Sensors, Sensors, 2021; vol. 21, no. 13, 4364.

[13]   Caminiti ML and Di Lazzaro V. Markerless Radio Frequency Indoor Monitoring for Telemedicine: Gait Analysis, Indoor Positioning, Fall Detection, Tremor Analysis, Vital Signs and Sleep Monitoring, Sensors, 2022; vol. 22, no. 21, 8486.

[14]   Zdravecký N, Ovseník Ľ, Oravec J and Lapčák M. Performance Enhancement of DWDM Optical Fiber Communication Systems Based on Amplification Techniques, Photonics, 2022; vol. 9, no. 8, 530.

[15]   Zheng H, Ma R and Zhu Z. A Wideband Low-Noise Linear LiDAR Analog Front-End, IEEE Transactions on Circuits and Systems I: Regular Papers, 2019; vol. 66, no. 8, 3065-3072.

[16]   Excelitas Technologies. (2020). C30737 Series Avalanche Photodiodes.

[17]   Texas Instruments. (2020). OPA657 Datasheet.

[18]   Analog Devices. (2018). AD8009 Datasheet.

[19]   Texas Instruments. (2019). THS3001 Datasheet.

[20]   Analog Devices. (2021). LTC6268 D
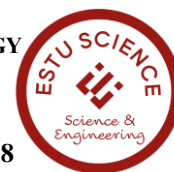
RESEARCH ARTICLE

EFFECT OF DIFFERENT CALCINATION TEMPERATURES ON SYNTHESIZED HYDROXYAPATITES FROM WASTE EGGSHELL

Nur BAYRAM [1], Sedef DİKMEN [2, *], Semra MALKOÇ [3,]

[1] Department of Advanced Technologies, Graduate School of Sciences, Eskişehir Technical University, Eskişehir, Türkiye
nurbayram96@hotmail.com- 🆔 0000-0003-4431-387X

[2] Department of Physics, Science Faculty, Eskişehir Technical University, Eskişehir, Türkiye
sdikmen@eskisehir.edu.tr - 🆔 0000-0002-6164-4710

[3] Department of Environmental Engineering, Faculty of Engineering, Eskişehir Technical University, Eskişehir, Turkiye
satik@eskisehir.edu.tr- 🆔 0000-0002-8092-411X

Abstract

ABSTRACT

About 94% of waste eggshells are composed of calcium carbonate ($CaCO_3$), which allows for the generation of calcium oxide (CaO), which can be utilized to synthesize hydroxyapatite (HAp). This study uses chemical precipitation and calcination methods to synthesize natural HAp from eggshell waste. In the first stage, the powdered eggshell was calcined at 900 °C to convert the calcium carbonate ($CaCO_3$) in the eggshell into calcium oxide (CaO), the precursor particles of HAp, before being subjected to chemical precipitation. To obtain HAp, the calcined eggshell powder was mixed with deionized water, and the suspension, whose pH was adjusted to 8.5 using phosphoric acid, was allowed to age. The precipitates obtained in the second stage were calcined at various temperatures (500 °C, 700 °C, 900 °C, 1000 °C, and 1100 °C) to produce hydroxyapatite (HAp) with the highest purity. The HAp samples synthesized at these calcination temperatures were characterized using several techniques: phase analysis through X-Ray Diffraction (XRD), chemical analysis via X-Ray Fluorescence (XRF) and microscopy, and thermal analysis using differential thermal analysis and thermogravimetric analysis (DTA-TG). XRD patterns show that the most suitable calcination temperature for HAp is 900 °C, and samples calcined at 900 °C, 1000 °C and 1100 °C contain peaks belonging to biphasic HAp and β-tricalcium phosphate (β-TCP) phase. The chemical analysis results show that HAp samples are mostly composed of Ca, P and O elements. The calculated Ca/P ratio for HAp samples recalcined at 900 °C is 1.73, which is close to the expected stoichiometric ratio of 1.67. HAp recalcined at 900 °C exhibited characteristic peaks at 571, 632, 962, 1046 and 1090 cm^{-1}. The intensities of most of the bands belonging to phosphate vibrations of HAp increased at calcination temperatures of 900 °C and above. As a result, the study showed that HAp can be synthesized from eggshell waste by using the precipitation and calcination methods together.

1. INTRODUCTION

Hydroxyapatite (HAp) is a calcium phosphate compound with the chemical formula $Ca_{10}(PO_4)_6(OH)_2$. It belongs to the apatite family, similar to the mineral structure of bones and teeth. Due to this similarity, it is highly biocompatible. HAp can bond with hard tissues, accelerating bone formation in diseased or damaged areas and preventing adverse effects caused by the immune system. Because of this, hydroxyapatite is used in various applications such as orthopedics, dental implants, and controlled drug

release systems [1]. It can be obtained from natural sources as well as synthesized chemically. Natural hydroxyapatite is derived from animal scales, bones, minerals, and shells [2]. The molar ratio of calcium and phosphate in hydroxyapatite (HAp) is 1.67. However, natural HAp is not stoichiometric and can have varying calcium and phosphorus content. There are several methods to obtain HAp, including chemical precipitation [3], sol-gel [4], hydrothermal synthesis [5], and mechano-chemical methods [6]. Currently, the most preferred method is chemical precipitation due to its low processing temperature, simplicity, high yield, and product quality [7, 8]. Panda et al. produced hydroxyapatite (HAp) from fish scales using calcination and alkaline heat treatment [9]. Janus et al. and Haberko et al. used pig bone for HAp synthesis and combined calcination with alkaline heat treatment in the synthesis process [10, 11]. Jaber et al. synthesized HAp from natural camel bone using the calcination method [12]. Pal et al. synthesized HAp from late calcarifer fish bone using the calcination method [13]. The use of seashells such as cockles [14], clams [13], and mussels [15] for processing HAp has shown promising results, with successful synthesis of HAp reported. Santhosh and Prabu synthesized HAp from seashells using chemical precipitation [16]. In addition to seashells, eggshells containing calcium carbonate ($CaCO_3$) have also been used as a calcium precursor for HAp synthesis. Goloshchapov et al. synthesized HAp using eggshells through calcination and chemical precipitation [17], while Okur and Koyuncu, and Patel et al. used eggshells for HAp synthesis through the precipitation method [18, 19].

Approximately 94% of the eggshell comprises calcium carbonate ($CaCO_3$), which makes it a valuable source for hydroxyapatite synthesis. The remaining percentage contains trace amounts of elements such as magnesium, sulphur, potassium, and sodium [18-20]. HAp obtained from eggshells has environmental, industrial, and biomedical applications and can be used as an adsorbent in cosmetics and water treatment systems [21].

Chicken eggshells, which are widely used in the food industry and by consumers every day, are often discarded as waste. With the global egg production totalling 70 million tons, and roughly 11% of the egg's weight being shell, approximately 8 million tons of eggshells are wasted each year [22].

This research uses chemical precipitation and calcination methods to obtain hydroxyapatite from waste eggshells, which helps reduce the environmental impacts of improper waste disposal. In the initial stage, calcium carbonate ($CaCO_3$) in eggshells was converted to calcium oxide (CaO) at 900 °C, creating the precursor particles of hydroxyapatite (HAp). During the synthesis stage, CaO combined with deionized water to form $Ca(OH)_2$. Finally, hydroxyapatite synthesis was completed by adding H_3PO_4 to the medium. The synthesized hydroxyapatite was subjected to different calcination temperatures (500 °C, 700 °C, 900 °C, 1000 °C, and 1100 °C) to determine the effect of temperature on HAp formation. For the purpose of characterizing the HAp samples synthesized from eggshells at these calcination temperatures, various analysis and imaging techniques were used. These included phase analysis (XRD; X-Ray Diffraction), chemical analysis (XRF; X-Ray Fluorescence), molecular structure analysis (FTIR; Fourier Transform Infrared Spectroscopy), imaging of the components in the structure (SEM; scanning electron microscope), and thermal analysis (TGA).
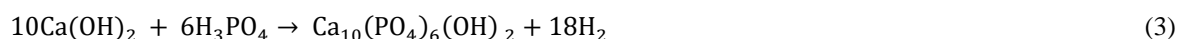
2. EXPERIMENTAL SECTION

2.1 Materials

A local company provided the eggshells for the experiments. The eggshells were washed with tap water, rinsed with deionized water, and left to air dry in the laboratory for one day. Afterwards, they were placed in an oven (Nuve FN 500) at 80 °C for 2 hours to remove any remaining moisture. The dried eggshells were then crushed using a Retsch mortar mill and sieved through a 250-micron sieve to prepare them for hydroxyapatite synthesis.

Orthophosphoric acid (H_3PO_4; Tekkim, 85%) was used as the phosphate source for the hydroxyapatite synthesis. During all experimental procedures, ultrapure water was utilized. A high-temperature furnace (Carbolite RHF 1400) was utilized for the calcination processes.

2.2. Synthesis of HAp

The synthesis of hydroxyapatite involved the use of a precipitation method with calcined eggshells [2]. The eggshells in powder form, with a particle size below 250 microns, were heated to 900°C in a high-temperature furnace at a heating rate of 20 °C/min and calcined for 1 hour at this temperature. During this process, CaO formed due to CO_2 being released from the $CaCO_3$ in the eggshell powder (Eq. 1). In the synthesis process, 2.8 g of calcined eggshell was initially added to 50 mL of deionized water. This caused the formation of $Ca(OH)_2$ as described in Eq. 2. Then, a 0.6 M H_3PO_4 solution was added until the pH value of the suspension reached 8.5. The suspension was then left to age for 24 hours. After 24 hours, it was stirred for 30 minutes with a magnetic stirrer and left to age again for another 24 hours. This ageing process resulted in the formation of $Ca_{10}(PO_4)_6(OH)_2$, as shown in Eq. 3. At the end of the ageing period, the calcined eggshells aged with phosphoric acid in the solution were washed with ultrapure water for 2 hours and then dried in an oven at 80°C for one day. Dried hydroxyapatite in powder form was subjected to recalcination at temperatures of 500 °C, 700 °C, 900 °C, 1000 °C, and 1100 °C for two hours to investigate the impact of temperature on various properties.

$$CaCO_3 \rightarrow CaO + CO_2 \tag{1}$$

$$CaO + H_2O \rightarrow Ca(OH)_2 \tag{2}$$

$$10Ca(OH)_2 + 6H_3PO_4 \rightarrow Ca_{10}(PO_4)_6(OH)_2 + 18H_2 \tag{3}$$

2.3. Characterization of HAps

Hydroxyapatite phases were determined using X-ray diffraction (XRD). A Bruker Advance D8 diffractometer with 45 kV anode voltage and 40 mA filament current settings was used. The instrument emitted nickel-filtered Cu Kα radiation at a wavelength of 0.154 nm. The goniometer of the diffractometer scanned the range 20°- 80° at a rate of 0.1°/s with a step size of 0.01°. Chemical analysis and to estimate the Ca/P ratio were performed using XRF (Bruker Tiger S8). Zeiss Ultra Plus FE-SEM instrument was used to visually confirm the synthesis of hydroxyapatite, the system operates in an acceleration voltage range of 5 kV, with the samples previously metalized with a gold layer and fixed on a carbon support. Molecular structure analysis of FT-IR spectra was obtained using Perkin Elmer Spectrum 100. Mass loss of the samples in nitrogen (N_2) environment was also measured using TGA (Netzsch STA 449 F3).

3. RESULTS

3.1. XRD Analysis of HAps

Figure 1(a) shows the XRD analysis of eggshell in powder form and calcined eggshell subjected to calcination process at 900 °C for 1 hour. Figure 1(b) shows the XRD patterns of the samples synthesized at 500 °C, 700 °C, 900 °C, 1000 °C and 1100 °C for 2 hours after reacting with H_3PO_4.
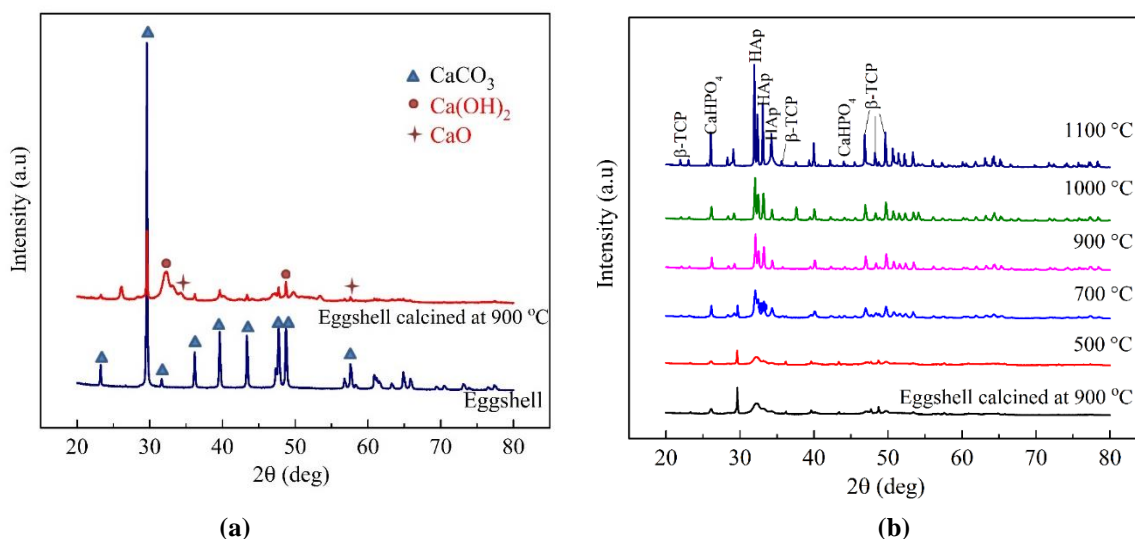
Figure 1. **(a)** Eggshell and eggshell calcined at 900 °C for 1 hour; **(b)** XRD patterns of hydroxyapatite samples sintered at different temperatures (500 °C, 700 °C, 900 °C, 1000 °C and 1100 °C) after synthesis with H_3PO_4.

The XRD patterns of the eggshell reveal that all peaks indicate the presence of calcium carbonate ($CaCO_3$). The highest peak for $CaCO_3$ is observed at an angle of 29.6°. After 1 hour of calcination, it is observed that some of the peaks for $CaCO_3$ have completely disappeared, while some remain in small amounts. The calcination process transforms the $CaCO_3$ in the eggshell to CaO, which is the precursor for HAp synthesis [23]. According to a study by Kamalanathan et al., the characteristic peak in the XRD results of $CaCO_3$ occurs at approximately $2\theta=29°$ [24].

After blending the calcined eggshell powder with H_3PO_4, the material was subjected to calcination at various temperatures. At a calcination temperature of 900 °C, it was observed that the peak intensity increased. The peaks obtained at this temperature completely overlapped with the peaks at 28.9°, 32.0°, 32.9°, and 34.3° according to card number ICDD 00-003-0747. XRD analysis shows that the optimal calcination temperature for HAp is 900 °C. HAp samples calcined at 900, 1000, and 1100°C exhibit peaks corresponding to biphasic HAp and β-tricalcium phosphate (β-TCP) phase. The peak generated at 900°C and higher calcination temperatures were even more intense and well-defined. It can be concluded that the material's crystallinity increases with higher calcination temperatures [23]. In a study conducted by Patel et al., clean and dry eggshells were taken and dried at 100°C for two days. Later, the eggshells were calcined at different temperatures (600°C, 800°C, 1000°C, and 1200°C) for three hours. The calcination process degraded $CaCO_3$ to yield CaO, producing $Ca(OH)_2$ with excess water. Afterwards, the $Ca(OH)_2$ reacted with phosphoric acid to yield TCP, which then reacted with CaO in a closed container at 1050°C for three hours, producing highly crystalline HAp powders [18]. In addition to the hydroxyapatite peaks, weak peaks are occurred at 25.8°, 34.5°, and 44.1° at 1100°C. These peaks are attributed to monetite ($CaHPO_4$) phase. The dominance of hydroxyapatite ($Ca_{10}(PO_4)_6(OH)_2$) is not observed in the HAp recalcined at 1100°C. Similar results were obtained by Agbaika et al. [25].

Ramirez-Gutierrez et al. indicated that the hydroxyapatite (HAp) obtained from pig bone exhibited intense peaks at high temperatures [26]. At high temperatures, HAp starts to decompose, leading to the formation of β-TCP as a new substance. Weak peaks are observed at 2θ angles of 21.9°, 35.4°, 44.1°, 46.8°, and 48.4° beginning at 900°C, corresponding to the presence of β-TCP [27]. Sun et al. and Hosseinzadeh et al. reported that the formation of β-TCP occurred at calcination temperatures of 750°C and 850°C for HAp, respectively [28, 29].

3.2. XRF Analyses of HAps

Chemical analysis determined the weight percentages of the elements in the eggshell and hydroxyapatite samples that were heated at different temperatures. The value presented in Table 1 indicates the transformation of the eggshell, which has a $CaCO_3$ structure after the calcination process, into CaO due to the loss of CO_2. Additionally, the weight percentages of CaO and P_2O_5 obtained from the recalcination of hydroxyapatite samples—produced by treating the calcined eggshell with H_3PO_4 at different temperatures, provide characteristic data [25]. The Ca/P ratio calculated from XRF results equals 1.73 for HAp recalcined at 900 °C, the closest value to 1.67. From XRF analysis, this ratio increases at calcination temperatures above 900 °C. At temperatures higher than 900 °C, other phases (such as monetite) affect the amount of hydroxyapatite, thus increasing the expected stoichiometry ratio. The main difference between synthetically produced HAp and natural HAp produced from animal-derived materials is that natural HAps have a higher Ca/P ratio than synthetic HAps. The stoichiometric ratio of synthetic HAps is closer to 1.67. Additionally, other researchers have noted Ca/P ratios that exceed the stoichiometric value [2, 25].

Table 1 Chemical composition of samples includes eggshell, eggshell calcined at 900°C for 1 h, and HAps heated at different temperatures.

Chemical composition	Eggshell (wt. %)	Eggshell calcined at 900 °C (wt. %)	HAp samples heated at different temperatures (wt.%)				
			500 ºC	700 ºC	900 ºC	1000 ºC	1100 ºC
CaO	90.75	96.81	64.01	63.52	62.25	64.09	66.17
P_2O_5	2.45	0.60	33.90	34.37	35.89	34.01	31.71
MgO	0.84	0.69	0.65	0.66	0.56	0.47	0.72
Na_2O	0.21	0.17	0.07	0.09	0	0	0
SO_3	4.11	0.55	0.30	0.28	0.20	0.37	0.28
K_2O	0.32	0.09	0	0.01	-	-	-
SrO	0.13	0.05	0.03	0.03	0.03	0.03	0.03
SiO_2	0.09	-	0.04	-	-	0	0.05
Fe_2O_3	0.02	-	0.01	0,01	-	0.01	0.04
Cl^-	0.72	0.04	-	-	-	0.02	0.02
Total	**99.64**	**99.00**	**99.01**	**98.97**	**99.00**	**99.00**	**99.02**

3.3. FTIR Analysis of HAps

The FT-IR analysis of the eggshell and the eggshell subjected to calcination at 900 °C for 1 hour is given in Figure 2 (a), and the FT-IR analysis of the samples obtained by the reaction of calcined eggshells with H_3PO_4 after being calcined at the different temperatures for two hours is given in Figure 2 (b).
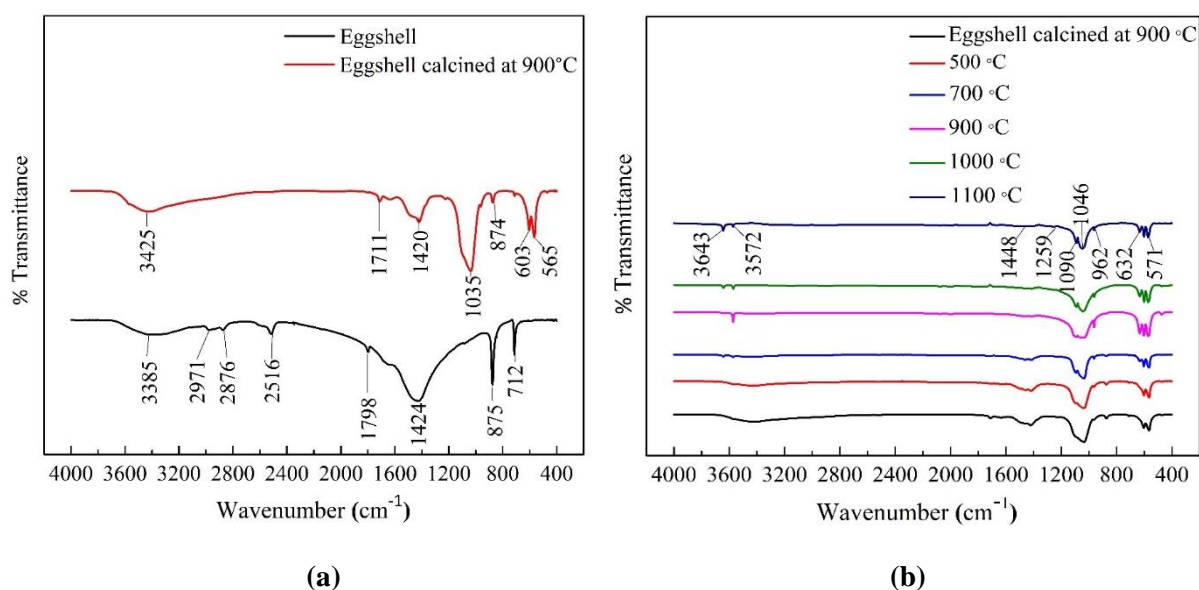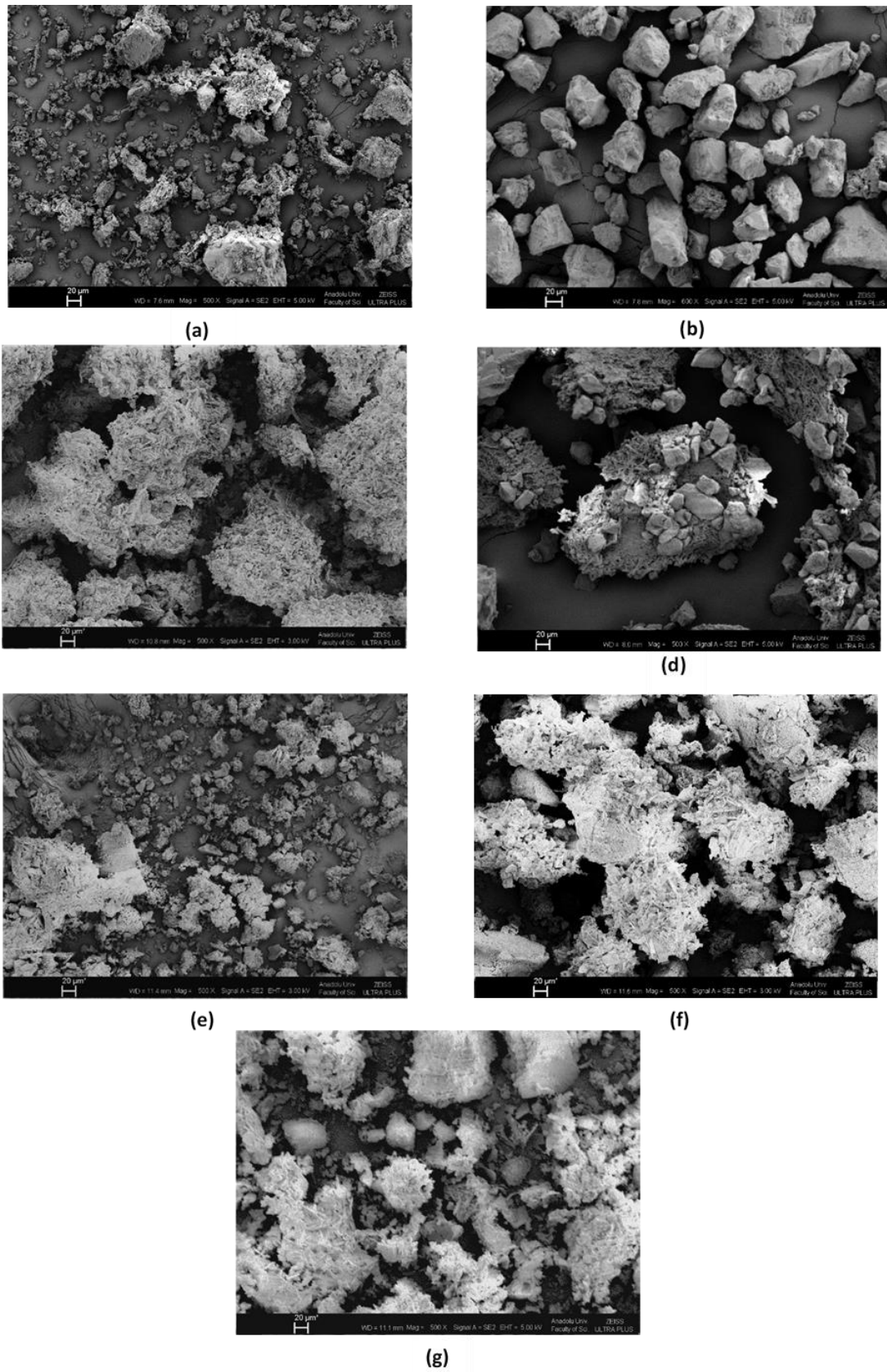
Figure 2. FT-IR analysis of **(a)** eggshell and calcined eggshell at 900 °C for 1 hour; **(b)** HAp samples heated at different temperatures (500 °C, 700 °C, 900 °C, 1000 °C and 1100 °C)

As seen in Figure 2 (a), the bands formed by the eggshell in the presence of the characteristic bands of CO_3^{-2} ion at 1424 and 874 cm^{-1} are occurred to be intense, while the intensity of these characteristic bands decreases as a result of calcination of the eggshell for one-hour [30]. This result also confirms the findings from the X-ray diffraction (XRD) analysis. The characteristic absorption peaks of hydroxyapatite (HAp) observed at 571, 632, 962, 1046, and 1090 cm^{-1} is present in samples that were calcined at temperatures of 700 °C and above. Among these peaks, the absorption peaks at 571 and 632 cm^{-1} are attributed to the v_3 and v_4 bending modes, respectively. The peak at 962 cm^{-1} corresponds to the v_1 symmetric stretching mode, while the absorption bands at 1046 and 1090 cm^{-1} are associated with v_3 asymmetric stretching. For the OH$^-$ group in the crystal structure of HAp, characteristic adsorption bands are observed at 3572 and 3643 cm^{-1} [12, 30].

3.4. SEM Images of HAps

Figure 4 displays SEM images of the eggshell calcined at 900°C for 1 hour and the HAp samples calcined at 500°C, 700°C, 900°C, 1000°C, and 1100°C for 2 hours, respectively. Upon examining the SEM images of the samples, it is evident that the eggshell calcined at 900°C for 1 hour exhibits a more homogeneous structure compared to the original eggshell. In other words, calcination resulted in a microstructure comprising dispersed grains. Following chemical precipitation and a second calcination, an interesting process unfolds. The particles appear to agglomerate, resulting in the formation of larger particles of varying sizes. These spherical agglomerates, predominantly small, occasionally manifest as larger entities, particularly noticeable at 1000 °C. However, upon comparison of images at 900°C, small-sized agglomerates were observed in eggshells, while large agglomerates were observed due to HAp synthesis. Furthermore, HAp exhibited agglomeration, leading to the formation of pores. Exposure of HAp samples to high temperatures is a factor that causes the skeletal structure to bond together [32, 33]. Other research has also found a similarly irregular particle structure of HAp derived from eggshells [17, 34]. Puad et al. also reported that increasing temperature causes particles to agglomerate, thus increasing the particle size. These findings are consistent with the results obtained from XRD and FTIR analyses of the microstructures formed as HAp begins to decompose [2].

Figure 4. SEM images of **(a)** eggshell, **(b)** eggshell calcined at 900 ℃ for 1 hour, HAps calcined at **(c)** 500 ℃, **(d)** 700 ℃, **(e)** 900 ℃, **(f)** 1000 ℃ and **(g)** 1100 ℃

3.5. Thermal Analysis of Eggshell

In Figure 5, the DTA-TG curves for eggshells are presented. In the DTA curve, there is an endothermic peak at 115 ℃, indicating a sudden mass loss, which can be attributed to the removal of water from the eggshell. The TGA curve shows a 3.25% mass loss between 400 and 470 ℃, caused by the desorption of water and other particles from the eggshell. Another strong endothermic peak is observed in the DTA curve at 463 ℃. Starting at 600 ℃, the mass of $CaCO_3$ rapidly decreases, with a continuous loss up to 850 ℃. The wider endothermic curve between 600 and 854 ℃ shows a 16.82% mass loss, which indicates the conversion of calcium carbonate to calcium oxide with the release of carbon dioxide. Beyond 850 ℃, no further mass loss occurs, and the sample stabilizes. Haberko et al. state that the low endothermic effect should plausibly be attributed to the evaporation of water adsorbed on the high surface area of the material, and at higher temperatures, two exothermic effects occurred [11]. Khandelwal and Prakash stated from DTA-TG analysis that a weight loss of about 2% up to 600˚C due to evaporation of absorbed water [33].
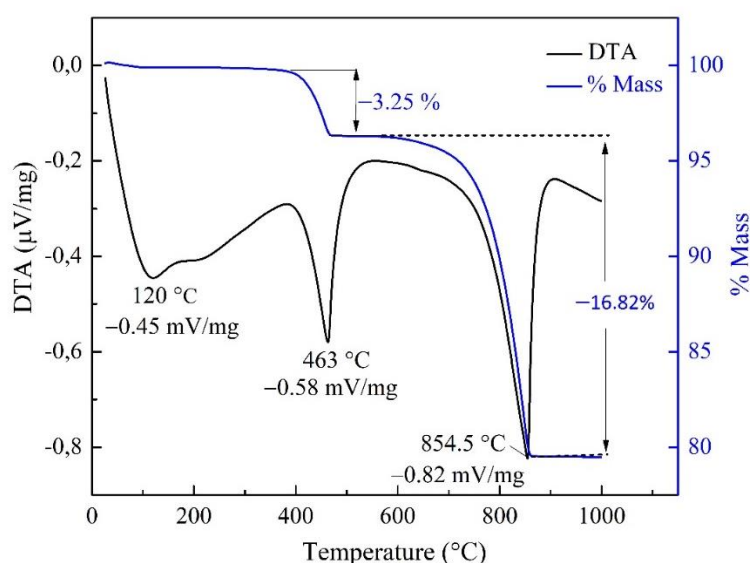
Figure 5. DTA-TG curve of eggshell

4. DISCUSSION AND CONCLUSION

In this study, HAp was synthesized from waste eggshells using chemical precipitation and calcination method and the effect of varying calcination temperatures (500 °C, 700 °C, 900 °C, 1000 °C, and 1100 °C) on the quality of HAp produced was investigated. The analyses were used to characterize the HAp samples synthesized from eggshells at these calcination temperatures. These included phase analysis (XRD), chemical analysis (XRF), molecular structure analysis (FT-IR), changes in the microstructure (SEM). Accordingly, the results can be explained as follows:

I)   The XRD patterns for HAp samples with calcination temperatures of 900°C and above show a well-defined intense peak for the hydroxyapatite phase. XRD results show that the most suitable calcination temperature for HAp is 900 °C, and HAp samples calcined at 900, 1000 and 1100 °C contain peaks belonging to biphasic HAp and β-tricalcium phosphate (β-TCP) phase. In addition to the hydroxyapatite peaks at the highest temperature, weak peaks appeared at 25.8°, 34.5° and 44.1° attributed to monetite ($CaHPO_4$). If the calcination temperature is increased beyond 1100°C, we can expect the monetite phase to completely transform into hydroxyapatite.

II) The XRF results indicate that the HAp samples mainly consist of the elements Ca, P, and O. The calculated Ca/P ratio for the HAp samples recalcined at 900 °C is 1.73, which is close to the expected stoichiometric ratio of 1.67. Based on the XRF analysis, it can be inferred that the sample recalcined at 900 °C approaches the hydroxyapatite phase. However, the presence of the monetite phase, as revealed by the XRD results, also explains why the Ca/P ratio is not exactly equal to 1.67.

III) FT-IR results show that the characteristic bands of calcium carbonate (eggshell) are observed at 1424 and 875cm $^{-1}$. After heating at 900°C for 1 h to form CaO, the precursor of HAp, a decrease in the intensity of these characteristic bands is observed in the FT-IR spectra. When the FTIR spectrum of HAp was examined, the characteristic asymmetric P−O stretching band belonging to PO_4^{-3} in its structure was observed at 1086 cm^{-1} and 1024 cm^{-1}. The symmetric P−O stretching band was determined at 962 cm^{-1}. HAp, obtained in its purest form at 900°C, exhibited characteristic peaks at 571, 632, 962, 1046, and 1090 cm^{-1}. The intensities of most of the bands belonging to the phosphate vibrations of HAp increased at calcination temperatures of 700 °C and above.

IV) In the SEM images, we noticed small clusters in eggshells and larger clusters resulting from the synthesis of HAp. Following chemical precipitation and a second calcination process, the particles formed larger particles of different sizes. These spherical clusters were evident as larger agglomerates at 1000°C. As the HAp samples were subjected to higher temperatures, the skeletal structure became more tightly bonded.

V) The research shows that eggshells can be used as recycling material to produce HAp powder, help with waste management, and keep the environment clean. Further research is expected to be conducted using other waste materials such as seashells (cockles, clams and mussels), fish bones, cattle, chicken bones to synthesize larger amounts of purer hydroxyapatite. Specifically, researchers should investigate different calcination temperatures to determine the optimal temperature for producing the purest hydroxyapatite phase.

VI) Consequently, eggshells could be further synthesized and transformed into valuable Ca-based compounds such as hydroxyapatite (HAp), tri-calcium phosphate (β-TCP), calcite ($CaCO_3$), and calcium hydroxide $Ca(OH)_2$.

ACKNOWLEDGEMENTS

CONFLICT OF INTEREST

The authors stated that there are no conflicts of interest regarding the publication of this article.

CRediT AUTHOR STATEMENT

Nur Bayram: Investigation, Writing − original draft, Visualization. **Sedef Dikmen:** Resources, Validation, Formal analysis. **Semra Malkoç:** Conceptualization, Methodology, Project administration, Resources, Funding acquisition.

REFERENCES

[1]   Metin N. Sintering and characterization of bovine hydroxyapatite. MSc, Istanbul Technical University, Istanbul, Turkey, 2013.

[2]   Pu'ad NM, Alipal J, Abdullah HZ, Idris MI, Lee TC. Synthesis of eggshell derived hydroxyapatite via chemical precipitation and calcination method. Mater Today: Proc 2021; 42: 172–177.

[3]   Mardziah CM, Ramesh S, Tan CY, Chandran H, Sidhu A, Krishnasamy S, Purbolaksono J. Zinc-substituted hydroxyapatite produced from calcium precursor derived from eggshells. Ceram Int 2021; 47(23): 33010-33019.

[4]   Labanni A, Handayani D, Ohya Y, Arief S. Size controlled synthesis of well-distributed nano-silver on hydroxyapatite using alkanolamine compounds. Ceram Int 2020; 46(5): 5850-5855.

[5]   Noviyanti AR, Akbar N, Deawati Y, Ernawati EE, Malik YT, Fauzia RP. A novel hydrothermal synthesis of nanohydroxyapatite from eggshell-calcium-oxide precursors. Heliyon 2020; 6(4): e03655.

[6]   Ferro AC, Guedes M, Mechanochemical synthesis of hydroxyapatite using cuttlefish bone and chicken eggshell as calcium precursors. Mater Sci and Eng 2019; 97: 124-140.

[7]   Kong LB, Ma J, Boey F. Nanosized Hydroxyapatite Powders Derived from Coprecipitation Process. J Mater Sci 2002; 37,1131-1134.

[8]   Kweh SK The production and characterization of hydroxyapatite (HA) powders. J Mater Process Technol 1999; 89(90): 373-377.

[9]   Panda S, Biswas CK, Paul S. A comprehensive review on the preparation and application of calcium hydroxyapatite: A special focus on atomic doping methods for bone tissue engineering. Ceram Int 2021; 47(20), 28122-28144.

[10]   Janus AM, Faryna M, Haberko K, Rakowska A, Panz T, Chemical and microstructural characterization of natural hydroxyapatite derived from pig bones. Mikrochim Acta 2008; 3(161): 349-353.

[11]   Haberko K, Bucko MM, Brzezinska-Miecznik J, Haberko M, Mozgawa W, Tomasz Panz, Pyda A, Zarebskia J. Natural hydroxyapatite-its behaviour during heat treatment. J Eur Ceram Soc 2006; 4-5(26): 537-542.

[12]   Jaber HL, Hammood AS, & Parvin N. Synthesis and characterization of hydroxyapatite powder from natural camelus bone. J Aust Ceram Soc, 2018; 54(1): 1-10.

[13]   Pal A, Maity S, Chabri S, Bera S, Chowdhury AR, Das M, Sinha A, Mechanochemical synthesis of nanocrystalline hydroxyapatite from Mercenaria clam shells and phosphoric acid, Biomed Phys Eng Express 2017; 315010.

[14]   Mohamad Razali NAI, Pramanik S, Abu Osman NA, Radzi Z, Pingguan-Murphy B. Conversion of calcite from cockle shells to bioactive nanorod hydroxyapatite for biomedical applications. J Ceram Process Res 2016; 17: 699-706.

[15]   Shavandi A, Bekhit, AD, Ali A, Sun Z. Synthesis of nano-hydroxyapatite (nHA) from waste mussel shells using a rapid microwave method. Mater Chem Phys 2015; 149(150): 607-616.

[16]   Santhosh S and Prabu SB. Thermal stability of nano hydroxyapatite synthesized from sea shells through wet chemical synthesis. Mater Lett 2013; 97: 21-124.

[17] Goloshchapov DL, Kashkarov VM, Rumyantseva NA, Seredin PV, Lenshin AS, Agapov BL, Domashevskaya EP, Synthesis of nanocrystalline hydroxyapatite by precipitation using hen's eggshell. Ceram Int 2013; 39: 4539-4549.

[18] Patel DK, Kim MH, Lim KT, Synthesis and characterization of eggshell derived hydroxyapatite bioceramics. J. Biosyst. Eng 2019; 44: 128-133.

[19] Okur M, Eslek Koyuncu D. The evaluation of hydroxyapatite synthesized from waste eggshell in the adsorption of Remazol N. Blue RGB dye. Journal of the Faculty of Engineering and Architecture of Gazi University 2020; 351:1-8.

[20] Tsai WT, Yang JM, Lai CW, Cheng YH, Lin CC, Yeh CW. Characterization and adsorption properties of eggshells and eggshell membrane. Bioresour Technol, 2006; 97: 488-493.

[21] Ummartyotin S, Manuspiya H. Eggshell waste: An effective source of hydroxyapatite for photocatalyst. JMMM 2018; 28(1): 124-135.

[22] Oliveira DA, Benelli P, Amante ER. A literature review on adding value to solid residues: eggshells. J. Cleaner Prod. 2013; 46:42-47.

[23] Natasha CY, Tan LT, Bang S, Ramesh CY, Ching, Chandran H Direct conversion of eggshell to hydroxyapatite ceramic by a sintering method. Ceram Int 2016; 42:7824-7829.

[24] Kamalanathan P, Ramesh S, Bang LT, Niakan A, Tan CY, Purbolaksono J, Chandran H, Teng WD. Synthesis and sintering of hydroxyapatite derived from eggshells as a calcium precursor. Ceram Int 2014; 40: 16349-16359.

[25] Agbabiaka OG, Oladele IO, Akinwekomi AD, Adediran AA, Balogun AO, Olasunkanm OG, Olayanju TMA. Effect of calcination temperature on hydroxyapatite developed from waste poultry eggshell. Scientific African 2020; 8: e00452.

[26] Ramirez-Gutierrez CF, Londoño-Restrepo SM, Del Real A, Mondragón MA, Rodriguez-García M E. Effect of the temperature and sintering time on the thermal, structural, morphological, and vibrational properties of hydroxyapatite derived from pig bone. Ceram Int 2017; 43(10): 7552-7559.

[27] Prem Anant K, Shanmugam S, Jose S, Nathanael P, Oh AJ, Mangalaraj, THD, Ballamurugan AM. Structural and chemical analysis of silica-doped β-TCP ceramic coatings on surgical grade 316L SS for possible biomedical application. J Asian Ceram Soc 2015; 3(3): 317-324.

[28] Sun RX, Lv Y, Niu YR, Zhao XH, Cao DS, Tang J, Sun XC, Chen KZ. Physicochemical and biological properties of bovine-derived porous hydroxyapatite/collagen composite and its hydroxyapatite powders. Ceram Int 2017;18(43): 16792-16798.

[29] Hosseinzahed E, Davarpanah M, Hassanzadeh Nemati N, Tavakoli SA, Fabrication of a hard tissue replacement using natural hydroxyapatite derived from bovine bones by thermal decomposition method. Int J Organ Transplant Med 2014; 1(5): 23-31.

[30] Shaltout AA, Allam MA, Moharram MA. FTIR spectroscopic, thermal and XRD characterization of hydroxyapatite from new natural sources. Spectrochim Acta A Mol Biomol Spectrosc 2011; 83(1): 56-60.

[31] Liu J, Ye X, Wang H, Zhu M, Wang B, Yan H. The influence of pH and temperature on the morphology of hydroxyapatite synthesized by hydrothermal method. Ceram Int 2003; 29(6): 629-633.

[32] Osuchukwu OA, Salihi A, Abdullahi I, Obada DO. Experimental data on the characterization of hydroxyapatite produced from a novel mixture of biowastes. Data in Brief 2022; 42, 108305.

[33] Supriyanto NS, Sukarni W, Puspitasari P, Permanasari A. Synthesis and characterization of $CaO/CaCO_3$ from quail eggshell waste by solid state reaction process. 2019; In AIP Conference Proceedings 2019; 1: 040032.

[34] Khanwendal H, Prakash S. Synthesis and characterization of hydroxyapatite powder by eggshell. JMMCE 2016; 4: 119-126.

RESEARCH ARTICLE

SEMI-SUPERVISED CLASSIFICATION OF 2D MATERIALS USING SELF-TRAINING CONVOLUTIONAL NEURAL NETWORKS

Umut Kaan KAVAKLI [1] , Bahar GÖRGÜN [2] , Ayşegül TERZİ [3] , Cahit PERKGÖZ [4] *

[1] Department of Computer Engineering, Faculty of Engineering, Eskisehir Technical University, Eskişehir, Turkey
umutkaankavakli@gmail.com - *0009-0003-4968-4124*

[2] Department of Computer Engineering, Faculty of Engineering, Eskisehir Technical University, Eskişehir, Turkey.
bahargorgun9@gmail.com - *0009-0003-4299-4488*

[3] Department of Computer Engineering, Faculty of Engineering, Eskisehir Technical University, Eskişehir, Turkey.
terziaysegul9696@gmail.com - *0009-0009-3671-5562*

[4] Department of Computer Engineering, Faculty of Engineering, Eskisehir Technical University, Eskişehir, Turkey.
cahitperkgoz@eskisehir.edu.tr - *0000-0003-0424-7046*

Abstract

Deep learning algorithms require large amounts of data, and their accuracy rates are directly related to the amount and quality of the data. Moreover, supervised learning models require the data to be labeled. However, data labeling is always a time-consuming and laborious process. Labeling data obtained from microscope images can be more laborious. Molybdenum disulfide (MoS_2) in monolayer form, which can be produced on large surfaces with the chemical vapor deposition method (CVD) and has advantages for potential electronic applications, is a frequently studied material in the field of nanotechnology. However, MoS_2 produced on these large surfaces usually has defective surfaces and needs to be detected. This process is a difficult process to be performed with a microscope by an expert. Artificial intelligence-based supervised learning algorithms, which need labeled data, provide an effective solution for these detections. Furthermore, increasing the number of labeled data increases the accuracy of these algorithms.

In this study, a teacher-student model is explored using self-training, a semi-supervised learning technique, to effectively train a deep convolutional neural network to detect defects on MoS_2 samples. Initially, the teacher model is trained using a small amount of data labeled by an expert. This trained model is enriched by generating pseudo-labels for previously unlabeled data. Then, a student model is trained using these real and pseudo-labeled data. The trained model then replaces the teacher model, and the process repeats, gradually improving labeling accuracy. The results show that the self-training method increases accuracy from 77% to 82% compared to the CNN model trained only on the existing labeled data, and the defect regions in MoS_2 are effectively classified with minimal manual labeling.

1. INTRODUCTION

In recent years, one of the most compelling fields has been artificial intelligence (AI) and its applications, particularly due to its potential to offer solutions to complex and time-consuming problems [1, 2]. As computing power has increased, AI techniques have been applied to numerous areas where their use was previously unfeasible [3, 4]. One of these areas is nanotechnology, specifically two-

dimensional (2D) materials, which have attracted significant attention due to their superior properties. Nanotechnology generally deals with the manipulation of materials at the atomic and molecular levels, focusing on the design, production, and application of materials at extremely small scales. Understanding the complex structures and properties of nanomaterials, optimizing them, and developing them for innovative applications have become more feasible with the integration of AI techniques.

Several studies have used machine learning methods to optimize the properties of graphene-based materials. Neural networks, a subclass of artificial intelligence, have been explored as a method to predict the behavior of materials using data obtained from laboratory instruments [5]. In another study, artificial intelligence methods have shown how they can be used to optimize the production processes of nanomaterials and support their characterization processes [6]. These studies highlight the importance of AI in the field of nanotechnology, but AI can be employed not only for the design and development of new nanomaterials but also to optimize their production processes. It can predict defects in the production phase, allowing for preventive measures to be taken, thereby increasing production efficiency, reducing costs, and improving product quality.

Since the discovery of graphene [7], interest in 2D materials has surged, and various 2D materials have been extensively studied [8]. Among these, transition metal dichalcogenides (TMDs) stand out as one of the most popular groups. In their monolayer form, TMDs possess unique optoelectronic properties, such as a direct bandgap, making them highly attractive for both material science and optoelectronic device applications [9]. Additionally, 2D materials offer a solution to reducing power loss in electronic chips by lowering the off-state current in transistors and enabling further miniaturization. [10]. Due to these advantages, 2D TMDs hold promise as channel materials in MOSFETs, offering wider bandgaps compared to graphene. Among the most studied TMDs is molybdenum disulfide (MoS_2), composed of covalently bonded Mo and S atoms, with weak Van der Waals forces holding the layers together [11, 12]. However, to fabricate devices from 2D materials, they must be produced on large surfaces without defects. While techniques such as mechanical exfoliation [13] and other methods [14] have been proposed, chemical vapor deposition (CVD) is the most suitable method for compatibility with microelectronics [15]. The CVD method shows promise for producing large-area, monolayer materials [16].

A crucial step in research is the analysis and characterization of 2D materials produced in the laboratory, which presents several challenges. One of the most significant challenges is determining whether the produced materials are defect-free or defective. While techniques such as Raman scattering spectroscopy, atomic force microscopy (AFM), and photoluminescence (PL) spectroscopy [17, 18] are commonly used, microscopic analyses are the most cost-effective [19], though they require expert operators. However, automating the characterization of large surfaces under a microscope using AI could make the process more practical and efficient. AI models can predict the properties of new nanomaterials from experimental data and theoretical calculations, analyzing images to more precisely characterize the structure and properties of nanomaterials, thereby minimizing trial-and-error in experiments. Various deep learning methods have been tested for this purpose [20-22].

Deep learning, a subset of AI, has gained popularity in nearly every scientific field over the past two decades, with convolutional neural networks (CNNs) making significant advancements, particularly in image processing and classification [23-25]. However, like all deep learning methods, CNN-based approaches require a large amount of labeled data. In the case of MoS_2 samples obtained through experiments that take hours in the laboratory, gathering and labeling sufficient data is both time-consuming and labor-intensive. In cases where labelled real data is scarce, we previously used Fresnel equations to generate artificial datasets and trained a CNN model using transfer learning to classify real MoS_2 flakes as normal or defective [26].

To address challenges with limited labeled data, self-training methods have been developed, utilizing both labeled and unlabeled data to improve model performance. In self-training [27, 28], a 'teacher' model is initially trained on a small, expert-labeled dataset known as 'true labels.' The teacher model then predicts 'pseudo-labels' on a large unlabeled dataset. A 'student' model is subsequently trained using a combination of both true and pseudo-labels. The student model is iteratively replaced by a new teacher model, and pseudo-labels are generated iteratively. As iterations progress, better pseudo-labels are produced, and the model's accuracy gradually improves with each iteration. Self-training methods have been applied to segmentation problems within the context of deep learning, offering a semi-supervised approach to enhance model performance with limited labeled data [29, 30]. In this study, a semi-supervised self-training deep learning method is proposed to identify defects in 2D materials when most of the data is unlabeled. Instead of manually labeling data, which is time-consuming and requires expert input, the approach first labels the unlabeled data and then performs classification using a CNN structure. MoS_2 was selected as a representative 2D material because of its widespread use in nanotechnology studies, attributed to its semiconductor properties and layered structure.

This article proceeds as follows: Section 2 introduces the proposed methodology and CNN concept. Section 3 discusses the experimental work and results, while Section 4 presents the conclusions.

2. MATERIALS AND METHODS

The goal of this study is to use deep learning methods to classify whether MoS_2 flakes in microscope images are defective or not (Figure 1). Initially, a small set of labeled data and a teacher-student semi-supervised model will be used to label the unlabeled data through self-learning. A CNN model will then be trained using both the labeled and pseudo-labeled data, and its performance will be evaluated using test data consisting real images for classification purposes. Therefore, in the following section, the designed CNN model will first be introduced, followed by an explanation of the teacher-student model. Finally, the methods used to define the success criteria of the approach will be discussed.
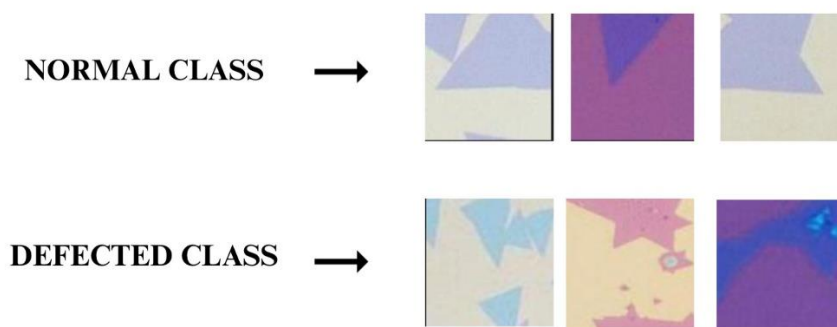

Figure 1. Normal and defected MoS_2 flakes

2.1. Convolutional Neural Networks

A Convolutional Neural Network (CNN) is a fundamental architecture in deep learning, designed specifically to process and extract information from images by progressively learning from low-level features to high-level patterns [31]. CNNs operate by applying multiple grids, known as kernels, over the input images. These kernels, which contain learnable parameters, capture different features and are optimized during training to enhance model performance. A non-linear activation function is employed to determine the activation of neurons based on the values obtained after linear computations [32].

Rather than using a single convolutional layer, CNNs consist of multiple layers, typically connected with pooling and fully connected layers. Pooling layers, such as max pooling or average pooling, reduce the spatial dimensions of the feature maps while retaining critical information, thus enhancing computational efficiency. Fully connected layers, often found in the final stages of the network, aggregate the information from the convolutional layers and serve as classifiers. Numerous state-of-the-art CNN architectures exist in the literature, including VGG [32], ResNet [33], and Inception [32], which have demonstrated strong performance in image classification tasks.

In this study, a CNN architecture with three convolutional layers is implemented, featuring 32, 64, and 128 filters of size 3x3 in each respective layer. Each convolutional layer is followed by a 2x2 max pooling layer. After the convolutional and pooling layers, a fully connected layer with 128 neurons is employed, and the final output layer utilizes a sigmoid activation function to support binary classification.

The objective of a machine learning model is to optimize its weights to achieve the best possible performance. During training, loss functions play a critical role in this optimization process by quantifying the discrepancy between the actual (ground truth) and predicted values of the model. The smaller the loss, the closer the model's predictions are to the ground truth, indicating higher model accuracy.

Several loss functions have been developed to address specific challenges, such as data imbalance. Data imbalance, a common issue in machine learning, arises when the distribution of classes is skewed, leading to biased model predictions favoring the majority class and poor performance in predicting the minority class. To mitigate this issue, specialized loss functions like Weighted Binary Cross Entropy (WBCE), Focal Loss, and Tversky Loss are often employed. However, in this study, the dataset is balanced, making the standard Binary Cross Entropy (BCE) loss function (Equation 1) sufficient for optimizing the model's performance.

$$L_{BCE} = -\frac{1}{N}\sum_{i=1}^{N}\left(y_i log(\hat{y}_i) + (1 - y_i)log(1 - \hat{y}_i)\right) \tag{1}$$

where N is the number of samples, y_i is the real label/output, and $\hat{y}$ is the predicted label/output of the model. BCE effectively measures the difference between predicted probabilities and actual binary class labels, guiding the model towards better predictions.

An optimization algorithm is used to update a model's weights based on the error output from the loss function. This process, known as backpropagation, adjusts each weight by propagating errors backward through the layers. The learning rate, a hyperparameter of the optimizer, controls the step size of these updates.

Gradient descent is a fundamental optimization method that iteratively updates the model's parameters to minimize the loss. However, it is often impractical due to its use of the entire dataset at once, which can strain memory resources. For this reason, the stochastic gradient algorithm (SGD) that uses subsets of the dataset (mini-batch) is mostly preferred. Moreover, more effective algorithms such as momentum SGD, RMSprop and Adam have also been used based on SGD. In this study, the Adam optimizer was preferred due to its durability and widespread use in deep learning applications.

While deep learning methods try to increase their accuracy performance, they only work on the dataset on which the training was made. If the algorithm is not stopped at a certain point, memorization may

occur on this dataset. As a result, while very high-performance values are obtained on the training set, the results would be worse on the test data. This situation is called overfitting and should be prevented. The strategies applied to prevent overfitting include increasing the training data, using data augmentation techniques, applying weight decay and adding dropout layers. On the contrary, in cases where the model is not complex enough or training is done with a small number of data, underfitting occurs and the performance of neural networks on the test data is again low. Increasing the model complexity can help address underfitting.

While CNNs perform effectively when trained on sufficiently large datasets, acquiring sufficiently labeled data in real-world applications can be challenging in some cases. For example, such challenges can be encountered when working with datasets that require expertise for labeling, such as microscopic images. To overcome this problem, semi-supervised approaches that utilize both labeled and unlabeled data, such as the self-training teacher-student model, have emerged as effective strategies. Improving performance in cases where limited labeled data is available can be achieved with the self-training teacher-student model.

2.2. Self-Training Model

Data labeling is one of the most challenging pre-processing steps for preparing data for model training, requiring significant expertise, time, and attention. In this study, a custom dataset was obtained under a microscope, with corresponding annotations provided by an expert. To address the challenges of labeling, a self-training method is employed. This technique, part of semi-supervised learning, utilizes a combination of a small number of labeled and a large number of unlabeled data to train the model. The training phase begins with only the labeled data, and the trained model is referred to as the teacher (Figure 2).
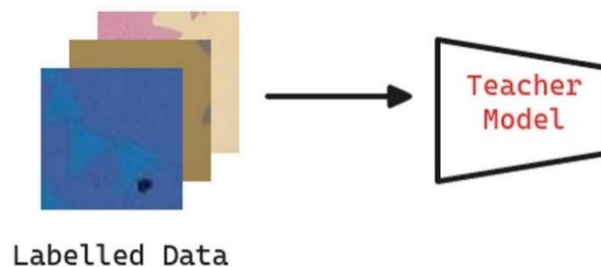
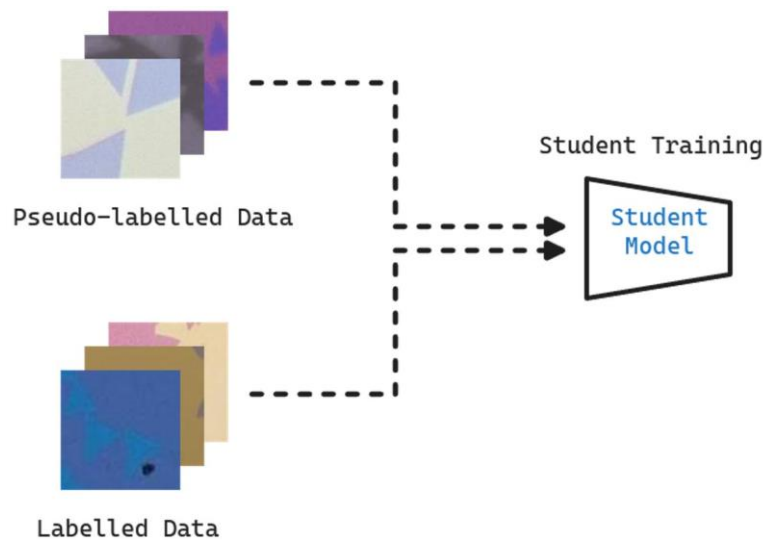

Figure 2. Teacher model trained with labelled data

After the teacher model is trained, it generates pseudo-labels by predicting on the unlabeled samples (Figure 3). As these labels are produced by the teacher model, some degree of noise is present in the predictions. Consequently, these pseudo-labels do not serve as an exact substitute for the true labeling process; however, the information they contain remains valuable for subsequent training phases. It is expected that the pseudo-labels generated by the teacher model may initially contain a certain amount of noise and may not be able to label all examples correctly. However, in the iterative teacher-student architecture, each new student model is updated, and the pseudo-labeling process continues in this loop. This gradually improves the accuracy of the pseudo-labels, improving the performance of the model.
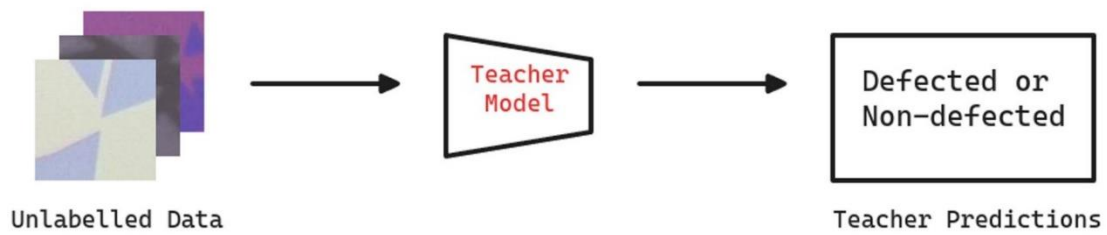
Figure 3. Teacher model predicting pseudo-labels

A new model is subsequently trained from scratch using both the real labeled and pseudo-labeled data (Figure 4). Since this model is trained on a combination of real and pseudo-labeled data, it is referred to as the student model. Although the student model may incorporate some noise, its performance is expected to improve due to training on a more diverse dataset. The noise level in pseudo-labels may affect the performance of the model at each iteration, and the low quality of pseudo-labels may lead the model to learn some incorrect patterns. This problem can be mitigated by using an early stopping point. Additionally, improving the quality of pseudo-labels using thresholding or filtering methods can significantly increase the accuracy of the model. This improvement can be further investigated in future work to optimize this method.

Figure 4. Student model trained with labelled and pseudo-labelled data

Upon completion of the training phase, the student model is promoted to serve as the new teacher model (Figure 5). It then generates a new set of pseudo-labels, which are expected to be of higher quality than the previous ones.
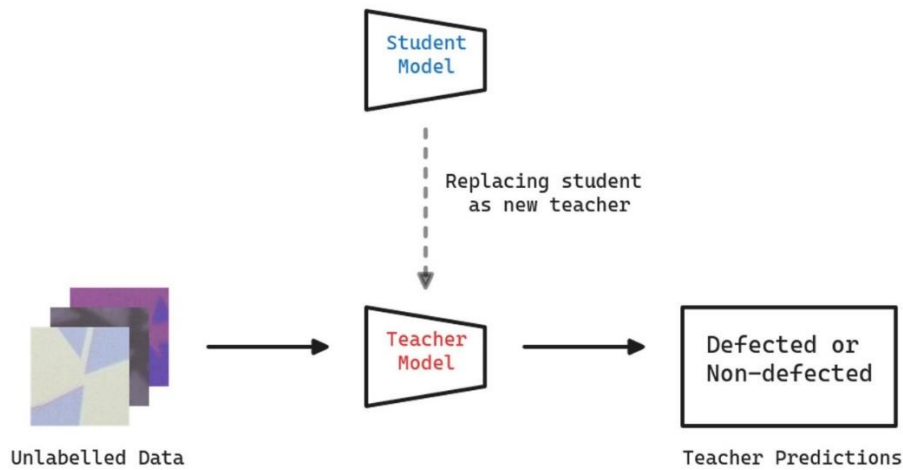
Figure 5. New teacher model copied from student model

There is no fixed limit to the number of student models that can be created or the number of pseudo-labels that can be generated. The process is iterative, as shown in Figure 6, with each new student model serving as the basis for generating updated pseudo-labels. This cycle continues until there is no significant improvement in the performance of the model. The challenges associated with training multiple student models iteratively are minimal, as the primary additional requirement is rerunning the software for the number of cycles in the teacher-student framework. This results in a linear increase in overall training time proportional to the number of iterations in each cycle. However, apart from this increase in computation time, no other significant challenges or complexities are introduced by the method. The process remains straightforward and scalable within the limits of available computational resources. At this point, the iterative process is typically stopped to avoid overfitting. The overall steps are illustrated in Figure 6.
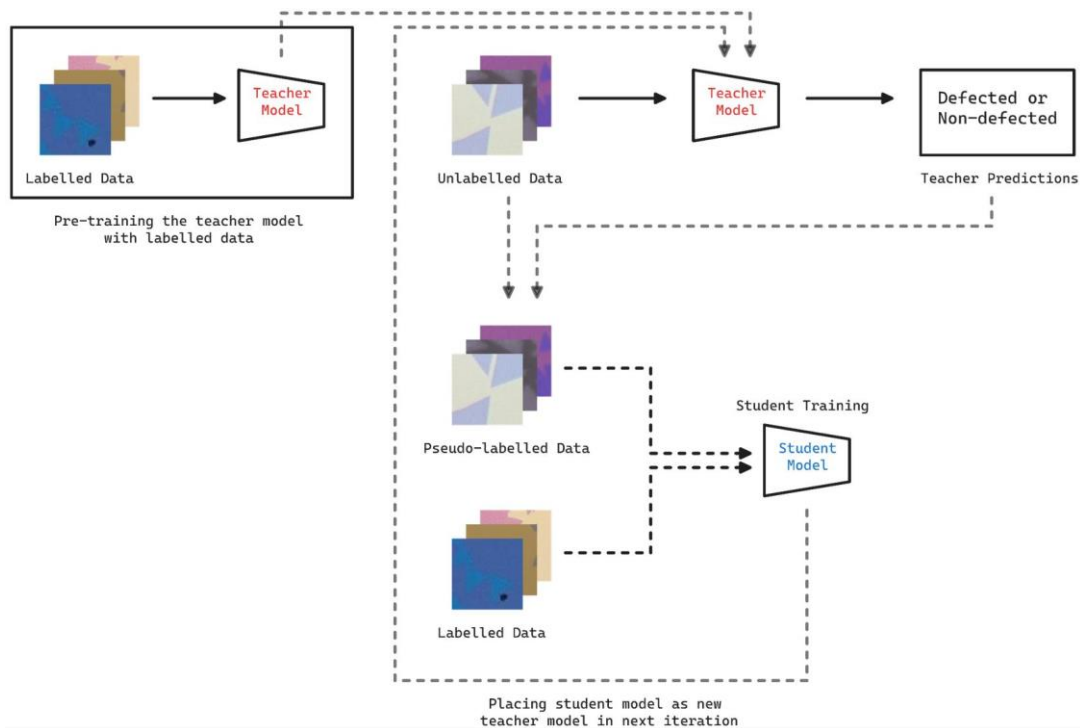

Figure 6. New teacher model copied from student model

2.3. Evaluation Metrics

The evaluation step assesses the true performance of the model. Since the model is trained on the training data and hyperparameters are optimized using the validation data, neither can be used for final evaluation, as the model is explicitly (training) or implicitly (validation) influenced by these datasets. Instead, the performance of the model on unseen samples is evaluated using a test set. Performance can be measured using various metrics, including accuracy, precision, recall, and F1 score (Equations 2-5). These metrics are computed based on a confusion matrix (Table 1), which provides a detailed breakdown of the performance of the model across specific criteria.

Table 1 Confusion matrix

The confusion matrix displays the relationship between the predicted values and the actual true values in a tabular format. It is utilized to analyze the model's errors and to identify imbalances between classes. Given that the dataset for this study was specifically designed to address data imbalance issues, only the accuracy metric was employed to evaluate the initial teacher and student models.

$$Accuracy = \frac{TP + TN}{TP + FP + TN + FN} \tag{2}$$

$$Precision = \frac{TP}{TP + FP} \tag{3}$$

$$Recall = \frac{TP}{TP + FN} \tag{4}$$

$$F1\ score = 2\ x\ \frac{Precision\ x\ Recall}{Precision + Recall} \tag{5}$$

Since the goal is to improve performance following the teacher model, the success criterion is defined as the increase in accuracy from the initial model to the final model.

3. RESULTS AND DISCUSSIONS

The model was conducted using Python programming with the Keras API of the TensorFlow framework and trained on an Nvidia GeForce GTX 1660 TI system with 6 GB of memory. Due to the relatively small image sizes (100x100 pixels), a CNN network was designed instead of resizing images to fit larger, state-of-the-art networks to mitigate overfitting. Data augmentation techniques, including Random Rotation and Random Vertical and Horizontal Flip, were applied. Non-linear activation functions in the hidden layers were selected as ReLU for its reliability, while a sigmoid function was used for the classifier at the end of the network. The networks were trained with a batch size of 4 and 10 epochs each. The choice of a low epoch size was made to prevent overfitting, given the limited amount of data. The hyperparameters and implementation details are provided in Table 2.

Table 2. Implementation details of the proposed model

Hyperparameter	Value
Input Image Size	100 x 100
Size of Labeled Training Dataset	246 (24%)
Size of Unlabeled Training Dataset	580 (56%)
Size of Validation Dataset	104 (10%)
Size of Test Dataset	104 (10%)
Epochs	10
Batch Size	4
Learning Rate	10^{-5}
Optimizer	Adam
Activation Function	ReLU
Loss Function	Binary Cross Entropy
Teacher Student Iteration	5
Data Augmentation	Random Rotation and Flip

A total of 6 networks were trained, consisting of one initial teacher network and five student networks. All results of the models were evaluated using the accuracy metric, which indicated that each subsequent student model demonstrated improved performance. The final results show an increase in accuracy from 77% to 82% with the use of self-training (Figure 7). Along with accuracy, other performance metric values (precision, recall, and F1-score) are provided in Table 3.

The iterative process in the teacher-student framework follows certain criteria to ensure effective training and prevent overfitting. In each iteration, pseudo-labels are generated based on predictions with confidence scores greater than 0.5, which are then assigned as new labels. The difference in loss values between successive student models is monitored to determine when to stop the iterative process. If this difference falls below 0.01, the training process is stopped to prevent overfitting while maintaining optimal model performance. These criteria increase the robustness of the self-training approach by providing a balance between comprehensive training and computational efficiency.
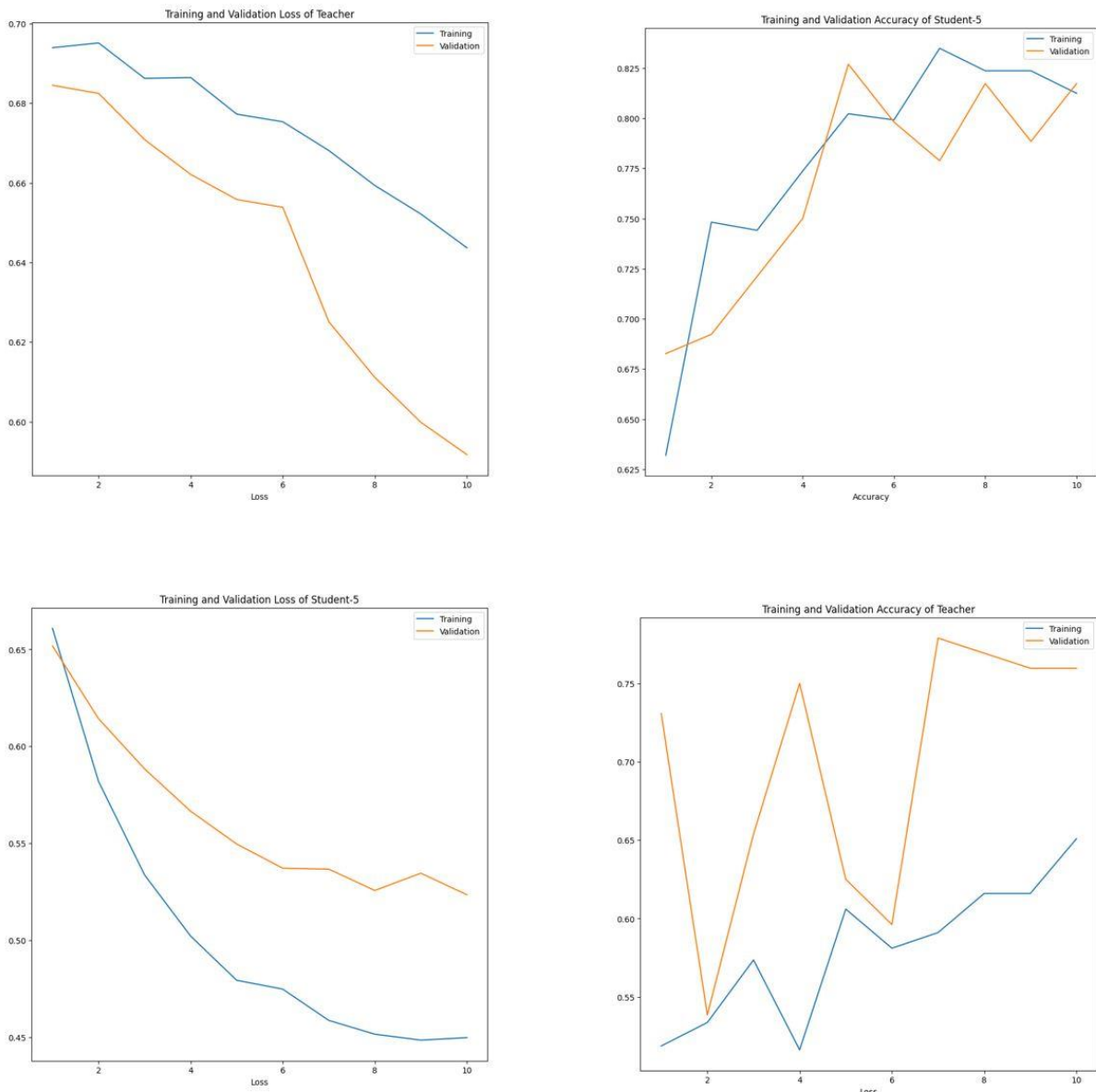
Figure 7. Loss and accuracy of teacher and student models

Table 3. Performance metric values

|	Accuracy	Precision	Recall	F1 Score
Teacher	0.7788	0.7925	0.8077	0.8002
Last Student	0.8269	0.8864	0.7500	0.8125

Early stopping and best checkpoint saving techniques were also employed to utilize the optimal weights if the model exhibited high loss or poor accuracy at the end of the training phase. Consequently, pseudo-labels were generated using the best weights of the teacher model rather than the final weights.

As shown in Figure 8, accuracy increases with each iteration of training the new student model. Although a peak in loss is observed at student 2, it did not impact the overall improvement in model performance.
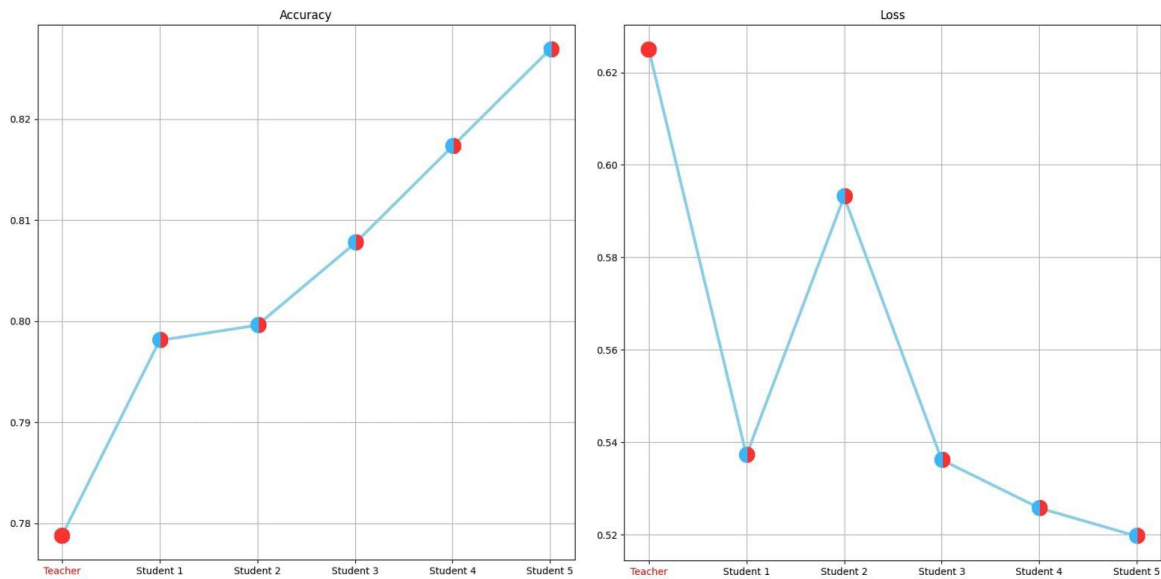
Figure 8. Accuracy and loss at each iteration

The model was tested using both the proposed Convolutional Neural Network and traditional machine learning approaches (Figure 9). The results indicate that the Convolutional Neural Network performs significantly better in classifying this problem compared to other models.
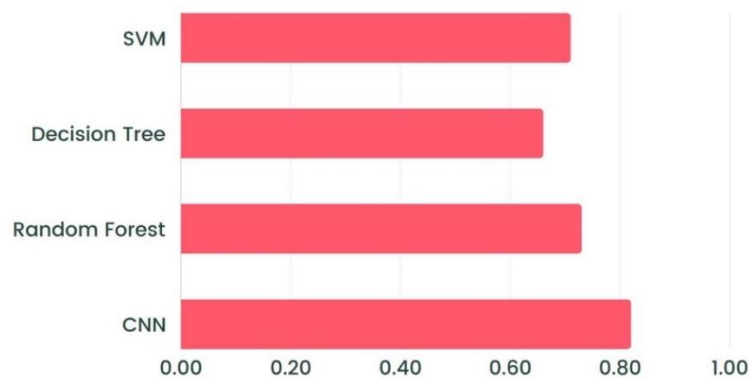
Figure 9. Comparison of machine learning algorithms with the proposed CNN model

A self-learning strategy was developed, given that only a small portion of the available data was labeled. The unlabeled data was labeled through this self-learning method. Initially, the teacher model achieved a relatively lower accuracy rate due to being trained on a limited amount of labeled data. However, as the previously unlabeled data were labeled and incorporated into the training set, an increase in the accuracy trend was observed, as expected. The model requires the training of multiple neural networks rather than a single one, which necessitates more time, but the results demonstrated improved performance compared to single-network training. Furthermore, this approach proved advantageous when compared to other machine learning models.

4. CONCLUSIONS

In this study, a self-learning method for the classification problem involving partially labeled datasets was investigated and tested on microscope images of two-dimensional nanomaterial Molybdenum Disulfide (MoS_2). Data labeling is a time-consuming and often expert-requiring preprocessing step. A dataset obtained from MoS_2 was collected and a small subset of the data was labeled under a microscope by experts. In addition to this data, unlabeled data was also provided. Semi-supervised self-training method, which allows both labeled and unlabeled data to be used in model training, was successfully implemented. The iterative training process significantly increased the performance of the algorithm as more pseudo-labeled data was used in each training cycle. All models were evaluated using the accuracy metric and it was observed that each subsequent learner model outperformed the previous model. The accuracy of the model increased from 77% to 82% with the self-training method compared to the CNN model trained with only manually labeled data. These results demonstrated the effectiveness of the method for partially labeled datasets. It has been shown to be a feasible solution to reduce the manual labeling burden in similar tasks.

In addition to the self-training method, the model has been tested using both the proposed Convolutional Neural Network (CNN) and traditional machine learning methods. The results show that proposed CNN significantly outperforms traditional models in classifying MoS_2 images. Combining labeled and pseudo-labeled data allow the model to achieve significant accuracy gains without requiring a fully labeled dataset. Collecting higher quality, larger, and more detailed images can further improve the performance of the model by providing a richer dataset for training. Furthermore, developing more advanced neural network architectures, optimizing hyperparameters, and experimenting with different learning strategies can also lead to better results. Integrating this approach into real-time platforms may offer practical applications for defect detection in industries such as semiconductor manufacturing or materials science.

In conclusion, the self-training method demonstrated in this study offers a promising solution to automate the labeling process and improve the classification accuracy of MoS_2 defects. By reducing the reliance on expert-labeled data, this method could significantly improve workflow in nanomaterial research and enable more efficient and accurate defect detection across a wider range of applications.

ACKNOWLEDGEMENTS

CONFLICT OF INTEREST

The authors stated that there are no conflicts of interest regarding the publication of this article.

CRediT AUTHOR STATEMENT

Umut Kaan Kavaklı: Methodology, Software, Formal Analysis, Data Curation, Investigation, Visualization, Validation, Writing – Original Draft.
Bahar Görgün: Conceptualization, Methodology, Software, Data Curation, Investigation, Resources, Writing – Original Draft.
Ayşegül Terzi: Methodology, Software, Validation, Data Curation, Visualization, Investigation, Writing – Original Draft.
Cahit Perkgöz: Conceptualization, Methodology, Resources, Writing – Review & Editing, Supervision.

REFERENCES

[1]   Alpaydin E. Introduction to machine learning: MIT press, 2020.

[2]   Ahmed SF, Alam MSB, Hassan M, Rozbu MR, Ishtiak T, Rafa N, et al. Deep learning modelling techniques: current progress, applications, advantages, and challenges. Artificial Intelligence Review, 2023;56:13521-617.

[3]   Liu Y, Yang Z, Yu Z, Liu Z, Liu D, Lin H, et al. Generative artificial intelligence and its applications in materials science: Current situation and future perspectives. Journal of Materiomics, 2023;9:798-816.

[4]   Vasoya N. Revolutionizing nano materials processing through IoT-AI integration: opportunities and challenges. Journal of Materials Science Research and Reviews, 2023;6:294-328.

[5]   Sobral JA, Obernauer S, Turkel S, Pasupathy AN, Scheurer MS. Machine learning the microscopic form of nematic order in twisted double-bilayer graphene. Nature Communications, 2023;14:5012.

[6]   Nandipati M, Fatoki O, Desai S. Bridging Nanomanufacturing and Artificial Intelligence—A Comprehensive Review. Materials, 2024;17:1621.

[7]   Geim AK, Novoselov KS. The rise of graphene. Nature materials, 2007;6:183-91.

[8]   Zhang Y, Yao Y, Sendeku MG, Yin L, Zhan X, Wang F, et al. Recent progress in CVD growth of 2D transition metal dichalcogenides and related heterostructures. Advanced materials, 2019;31:1901694.

[9]   Zhang H. Introduction: 2D materials chemistry. ACS Publications, 2018. p. 6089-90.

[10]   Hua Q, Gao G, Jiang C, Yu J, Sun J, Zhang T, et al. Atomic threshold-switching enabled MoS_2 transistors towards ultralow-power electronics. Nature Communications, 2020;11:6207.

[11]   Zhang Y, Wan Q, Yang N. Recent advances of porous graphene: synthesis, functionalization, and electrochemical applications. Small, 2019;15:1903780.

[12]   Fortin E, Sears W. Photovoltaic effect and optical absorption in MoS_2. Journal of Physics and Chemistry of Solids, 1982;43:881-4.

[13]   Yi M, Shen Z. A review on mechanical exfoliation for the scalable production of graphene. Journal of Materials Chemistry A, 2015;3:11700-15.

[14]   Bonaccorso F, Lombardo A, Hasan T, Sun Z, Colombo L, Ferrari AC. Production and processing of graphene and 2d crystals. Materials today, 2012;15:564-89.

[15]   Liu H, Wong SL, Chi D. CVD growth of MoS_2-based two-dimensional materials. Chemical Vapor Deposition, 2015;21:241-59.

[16]   Liu D, Chen X, Yan Y, Zhang Z, Jin Z, Yi K, et al. Conformal hexagonal-boron nitride dielectric interface for tungsten diselenide devices with improved mobility and thermal dissipation. Nature Communications, 2019;10:1188.

[17] Özden A, Şar H, Yeltik A, Madenoğlu B, Sevik C, Ay F, et al. CVD grown 2D MoS_2 layers: A photoluminescence and fluorescence lifetime imaging study. physica status solidi (RRL)–Rapid Research Letters, 2016;10:792-6.

[18] Zhang J, Yu Y, Wang P, Luo C, Wu X, Sun Z, et al. Characterization of atomic defects on the photoluminescence in two-dimensional materials using transmission electron microscope. InfoMat, 2019;1:85-97.

[19] Yorulmaz B, Özden A, Şar H, Ay F, Sevik C, Perkgöz NK. CVD growth of monolayer WS_2 through controlled seed formation and vapor density. Materials Science in Semiconductor Processing, 2019;93:158-63.

[20] Lin X, Si Z, Fu W, Yang J, Guo S, Cao Y, et al. Intelligent identification of two-dimensional nanostructures by machine-learning optical microscopy. Nano Research, 2018;11:6316-24.

[21] Ngome Okello OF, Yang D-H, Chu Y-S, Yang S, Choi S-Y. Atomic-level defect modulation and characterization methods in 2D materials. APL Materials, 2021;9.

[22] Al-Waisy AS, Ibrahim DA, Zebari DA, Hammadi S, Mohammed H, Mohammed MA, et al. Identifying defective solar cells in electroluminescence images using deep feature representations. PeerJ Computer Science, 2022;8:e992.

[23] Yao G, Lei T, Zhong J. A review of convolutional-neural-network-based action recognition. Pattern Recognition Letters, 2019;118:14-22.

[24] Alzubaidi L, Zhang J, Humaidi AJ, Al-Dujaili A, Duan Y, Al-Shamma O, et al. Review of deep learning: concepts, CNN architectures, challenges, applications, future directions. Journal of big Data, 2021;8:1-74.

[25] Bhuvaneswari V, Priyadharshini M, Deepa C, Balaji D, Rajeshkumar L, Ramesh M. Deep learning for material synthesis and manufacturing systems: A review. Materials Today: Proceedings, 2021;46:3263-9.

[26] Perkgoz C. Identifying optical microscope images of CVD-grown two-dimensional MoS_2 by convolutional neural networks and transfer learning. PeerJ Computer Science, 2024;10:e1885.

[27] Xie Q, Luong M-T, Hovy E, Le QV. Self-training with noisy student improves imagenet classification. Proceedings of the IEEE/CVF conference on computer vision and pattern recognition, 2020. p. 10687-98.

[28] Zou Y, Yu Z, Liu X, Kumar B, Wang J. Confidence regularized self-training. Proceedings of the IEEE/CVF international conference on computer vision, 2019. p. 5982-91.

[29] Yu L, Liu X, Van de Weijer J. Self-training for class-incremental semantic segmentation. IEEE Transactions on Neural Networks and Learning Systems, 2022;34:9116-27.

[30] Ke R, Aviles-Rivero AI, Pandey S, Reddy S, Schönlieb C-B. A three-stage self-training framework for semi-supervised semantic segmentation. IEEE Transactions on Image Processing, 2022;31:1805-15.

[31]   Yamashita R, Nishio M, Do RKG, Togashi K. Convolutional neural networks: an overview and application in radiology. Insights into imaging, 2018;9:611-29.

[32]   Soffer S, Ben-Cohen A, Shimon O, Amitai MM, Greenspan H, Klang E. Convolutional neural networks for radiologic images: a radiologist's guide. Radiology, 2019;290:590-606.

[33]   He K, Zhang X, Ren S, Sun J. Deep residual learning for image recognition. Proceedings of the IEEE conference on computer vision and pattern recognition, 2016. p. 770-8.

RESEARCH ARTICLE

THE EFFECT OF FIRING TEMPERATURE ON THE PROPERTIES OF GLAZES PREPARED WITH BARIUM-BASED FRIT

Betül YILDIZ [1], [*]

[1] Bilecik Şeyh Edabali University, Faculty of Engineering, Department of Metallurgical and Materials Engineering, Bilecik, Türkiye
betul.yildiz@bilecik.edu.tr - 0000-0002-7520-7722

Abstract

Barium-based frits are commonly utilized in the ceramic tile industry to produce matte glazes. In these glazes, the microstructure—and consequently, the opacity and matte finish—vary depending on factors such as composition, application conditions, and firing temperatures. This study investigates the effects of different firing temperatures on the microstructure and properties of glazes prepared with barium-based frits. For this purpose, compositions containing 92 wt% barium-based frit and 8 wt% kaolin were milled, applied to the tile surface, and then fired in a laboratory furnace at four different peak temperatures (900, 1000, 1100, and 1200°C). The results indicate that the primary phase formed in the glaze structure is celsian at peak temperatures of 1100°C and 1200°C. As the temperature increases, the glassy phase expands, and crystal size increases. A decrease in the whiteness value (L*) value was observed with rising temperature; however, the glaze generally maintained its matte finish, as indicated by the 60° gloss value.

1. INTRODUCTION

Ceramic glazes are glassy coatings that improve the hygiene, functionality, and visual appeal of ceramic products [1,2]. Glazes are mixtures and glassy coatings created from finely ground ceramic raw materials, formulated with specific compositions. When fired onto the ceramic surface, they form a glass-like structure [3]. Standard glaze formulations consist of ceramic raw materials and various frits [4]. After grinding and applying the glaze to a ceramic body, it is fired to form a partially or fully vitreous coating. This glaze enhances both the chemical and mechanical properties of the ceramic substrate [5, 6]. In addition to these functional properties, glaze significantly contributes to the aesthetic qualities of ceramic tiles [1].

In the industrial sector, glazes are commonly categorized based on their optical characteristics into four groups: transparent matte, transparent glossy, opaque matte, and opaque glossy. Matte glazes tend to have greater surface roughness compared to glossy ones, which leads to multiple reflections of incoming light. This results in reduced specular reflection and a lower gloss level. The roughness observed in matte glazes is typically attributed to the presence of crystals. These crystals are thought to obstruct the smooth flow of the surface. Even in the absence of crystals, any glaze with high viscosity can create a matte finish due to insufficient surface smoothness [7, 8]. Common crystals observed in matte glazes include wollastonite ($CaSiO_3$) and willemite (Zn_2SiO_4) [9]. Alongside wollastonite- and willemite-based glazes, celsian ($BaAl_2Si_2O_8$) based glazes which are used to achieve matte surfaces, have become popular in tile production. [7].

---

*Corresponding Author: betul.yildiz@bilecik.edu.tr

BaO functions as a flux in ceramic glazes and frits, though it becomes active at temperatures above 1100°C. Below this temperature, BaO promotes crystallization by increasing viscosity [5]. The addition of BaO enhances glaze brightness; improves mechanical properties, and lowers the thermal expansion coefficient [3, 8]. BaO is typically introduced into glaze compositions as $BaCO_3$; however, due to its high toxicity, it is preferably incorporated through frits [5, 10, 11].

The microstructure of glazes generally consists of amorphous phase, porosity, and crystalline phase(s) [12]. The composition of ceramic glazes, grinding conditions, application parameters on tile surfaces, and firing schedules directly influence the microstructure and, consequently, the aesthetic, chemical, and technical properties of the glaze [13]. This research examines how different firing temperatures affect the microstructure and optical characteristics of glazes prepared with commercial barium-based frit.

Several studies have examined the effects of firing temperatures on glaze properties. Tezza et al., for instance, investigated how firing temperature influences the characteristics of anatase-based glazes [14], while Fröberg et al. explored the effects of composition and firing cycles on phase formation in raw glazes for floor tiles [15]. Imer et al. investigated the impact of firing temperatures on the structure of luster coatings [16]. Zhao et al. also explored how glaze composition and firing cycles affect the Raman polymerization index in celadon ceramic glazes [17]. Schabbach et al. analyzed the impact of peak firing temperatures on color development in zircon-based glazes [18].

In particular, Bou et al. investigated how firing temperatures affect the structure and aesthetic properties of barium-based glazes, with a focus on the influence of grain size distributions and firing temperatures on structure and matteness in matte wall and floor tile glazes. Their study used high BaO-content barium frits for single-firing tile glazes and glazed porcelain tile production. These frits were mixed with raw materials such as zircon, nepheline, and feldspar, ground, and fired at various peak temperatures. After firing, zircon, celsian, and barium orthoclase phases were identified in the glazes. The glazes were fired at peak temperatures of 1000, 1020, 1040, 1060, and 1080°C, with observed decreases in L* and gloss values as temperatures increased [7].

In the present study, commercial barium-based frit was similarly utilized, but with a broader range of firing temperatures compared to Bou et al.'s study. Additionally, to examine the effect of temperature solely on the frit structure, no raw material other than 8 wt% kaolin was incorporated into the glaze composition. The glazes were prepared using 92 wt% barium-based frit and 8 wt% kaolin, then fired at four different peak temperatures ranging from 900°C to 1200°C, with 100°C intervals, in a laboratory-scale furnace. The effects of varying firing temperatures on glaze microstructure and aesthetic properties were examined while other factors remained constant.

2. EXPERIMENTAL METHODS

2.1. Preparation and Firing of Glaze Samples

In this study, a glaze formulation was developed using a commercial frit composition. The chemical composition of the commercial frit is shown in Table 1. A glaze mixture consisting of 92 wt% barium-based frit and 8 wt% kaolin was placed into a mill with a solid-to-liquid ratio of 70%. Next, 0.2 wt% sodium carboxy methyl cellulose (CMC) and 0.2 wt% sodium tripolyphosphate (STPP) were incorporated, and the mixture was ground for 40 minutes. After milling, the glaze density was measured to be 1.80 g/cm³. A fluidity test conducted with a 4 mm Ford Cup showed a flow time of 18 seconds. The glaze suspensions were applied to the surface of wall tiles using a 0.8 mm glazing tool. The tiles were subsequently dried at 110°C for 30 minutes. Afterward, they were fired in a Nabertherm N210E laboratory furnace at four distinct peak temperatures. The samples were heated at a rate of 10°C/min until reaching their peak temperature, held at that temperature for 10 minutes, and then cooled back to

room temperature at the same rate. To assess the impact of different firing temperatures on the glaze, the samples were fired at peak temperatures of 900°C, 1000°C, 1100°C, and 1200°C. The corresponding sample codes and descriptions are provided in Table 2.

In a previous study, the melting behavior of this frit was analyzed using hot-stage microscopy, and the particle size distribution after 40 minutes of grinding was measured using a laser technique [13]. The relevant data are provided in Tables 3 and 4, respectively. After 40 minutes of grinding, the d(0.5) value of the glaze was determined to be 6.862 µm (Table 3). The softening, half-sphere, and fusion temperatures of the glaze were found to be 854°C, 1156°C, and 1162°C, respectively. The glaze did not exhibit spherical behavior with increasing temperature (Table 4).

Table 1. The chemical composition of the frit coded as Ba-F [13]

Ba-Based Frit	Oxide weight %
Na_2O	1-5
K_2O	1-5
CaO	7-15
BaO	7-15
ZnO	7-15
Al_2O_3	10-18
B_2O_3	1-8
SiO_2	45-55

Table 2. Samples' codes and explanation

Sample code	Explanation
Ba-F	Barium based commercial frit
S Glaze	Unfired raw glaze prepared with Ba-F
S-900	S glaze fired at 900°C
S-1000	S glaze fired at 1000°C
S-1100	S glaze fired at 1100°C
S-1200	S glaze fired at 1200°C

Table 3. Particle size distribution of S glaze after 40 minutes of grinding [13]

Sample	d(0.1)	d(0.5)	d(0.9)
S Glaze	1.553	6.862	26.761

Table 4. Results of hot stage microscopy analysis of S glaze after 40 minutes of grinding [13]

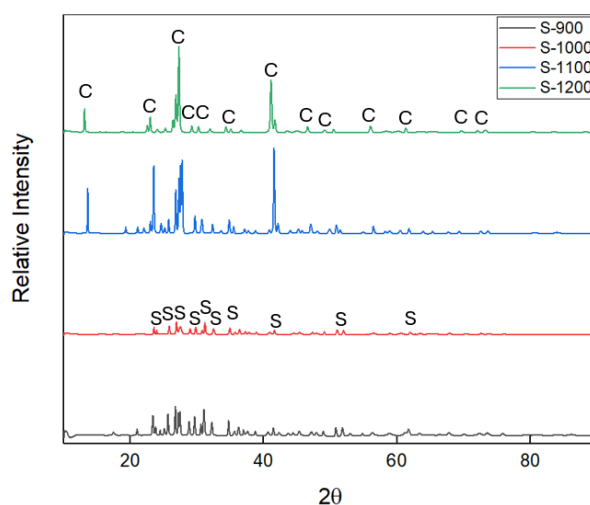| S Glaze	Temperature(°C)
$T_{Sintering}$	852
$T_{Softening}$	854
T_{Sphere}	-
$T_{Half Sphere}$	1156
T_{Fusion}	1162

2.1.2 Glaze Characterization

Panalytical/Empyrean diffractometer was used to determine the phases formed in the glaze structure after firing process. The glazed samples were analyzed within the 2θ range of 10° to 90°.

The microstructure of the glazed tiles was analyzed with a field emission scanning electron microscope (FE-SEM) equipped with an EDS detector (ZEISS, Gemini 500). Images were obtained from the cross-sectional surfaces of the glazes at magnifications of 500X and 1000X using a backscattered electron detector. EDX analysis was carried out on the light gray (crystalline phase) and dark gray (glassy phase) areas of the S-1200 coded sample, where the formed crystals were clearly visible.

The color and gloss of the samples (measured at a 60° angle) were evaluated using a Konica Minolta Spectrophotometer CM 600D. To ensure the reliability of the results, both color and gloss measurements were conducted three times, and the average values were calculated from the obtained data.

3. RESULTS AND DISCUSSIONS

The XRD patterns of the glazes are given in Figure 1. According to the XRD results, sanidine $((K,Na)AlSi_3O_8)$ was detected in the glazes fired at 900°C and 1000°C, whereas the primary phase observed at 1100°C and 1200°C was identified as celsian. Given that BaO behaves as an active flux above 1100°C [5], it is hypothesized that celsian crystal formation may have been promoted in the glazes fired at temperatures exceeding 1100°C. Although different temperatures for the crystallization of celsian in glass-ceramic structures have been reported, it is generally observed that these temperatures range from 800°C to 1050°C. In a study examining the BaO ratio in glass-ceramic glazes of the BAS $(BaO-Al_2O_3-SiO_2)$ system, the celsian crystallization temperature was found to be between 808°C and 918°C [19]. Another study determined the crystallization temperature of barium feldspar in a glass-ceramic glaze to be 955.6°C [20]. In a further study, the formation temperature of celsian crystals in the BAS glass-ceramic system was found to range from 870°C to 1050°C [21,22]. In this study, the XRD analysis conducted demonstrates that distinct celsian crystals form in glazes fired at 1100°C and 1200°C under laboratory conditions. However, firing at 900°C and 1000°C did not provide sufficient conditions for the formation of celsian crystals.

Figure 1. X-ray diffraction patterns of glazes (C: Celsian, S: Sanidine)

The microstructures of the glazed surfaces are given in Figure 2 and 3. In Figure 2, a noticeable decrease in the amount of porosity is observed as the temperature increases. The viscosity of the glaze decreased as the temperature increased during sintering [23]. Higher temperatures promoted the formation of more glassy phase, enhanced sintering and reduced the amount of porosity in the structure.

In the S-900 and S-1000 samples, sub micron crystals cluster are not clearly distinguishable within the glassy phase. However, as the temperature reaches 1100°C, the crystals within the glassy phase become more evident. In the S-1100 glaze, crystal sizes were observed to be below 10 microns, and the crystals formed a network-like structure in clusters. In contrast, in the S-1200-coded glaze, the width of the needle-like crystals ranged from 1 to 5 µm, with lengths reaching up to 100 µm (Figure 3). EDX analysis was performed on the S-1200-coded glaze. Figure 4 and Table 5 present the EDX patterns and elemental weight percentages determined for the glassy and crystalline phases of the S-1200 glaze. According to the EDX patterns, the intensities of the Al and Ba peaks from the dark area (glassy phase) were lower than those from the light area (crystalline phase), while the intensities of the Ca, Na, and Zn peaks were higher. The amount of barium element detected in the crystalline and glassy phases was 22.17% and 4.12%, respectively. These results demonstrate a clear correlation, indicating that the Ba content in the matrix crystallizes as celsian crystals. This finding is consistent with the XRD analysis, which further supports the observations.
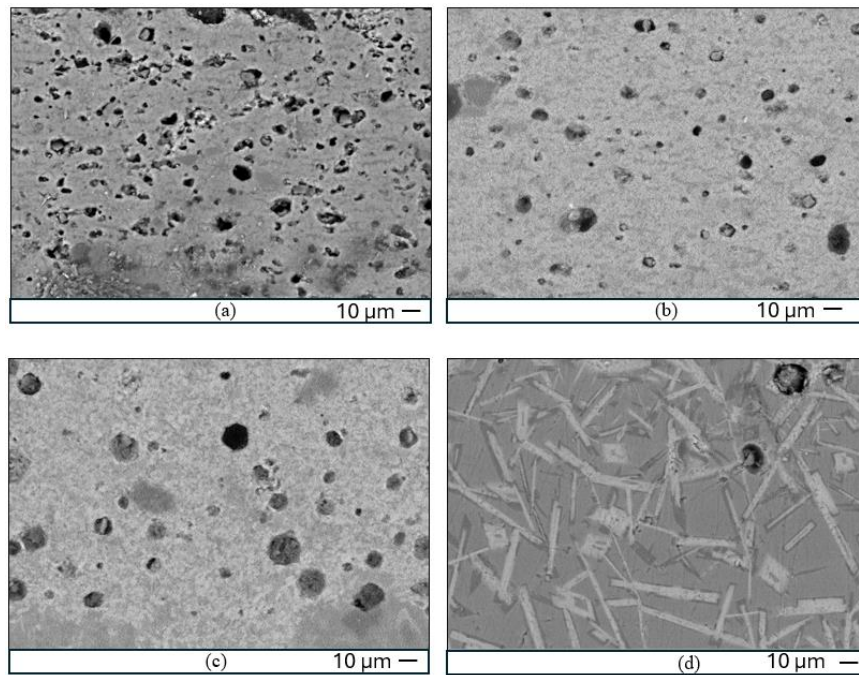
Figure 2. Scanning electron microscope images taken at 500x magnification using a backscattered electron detector from the cross-sectional surfaces of the studied glazes: (a) S-900; (b) S-1000; (c) S-1100; (d) S-1200.
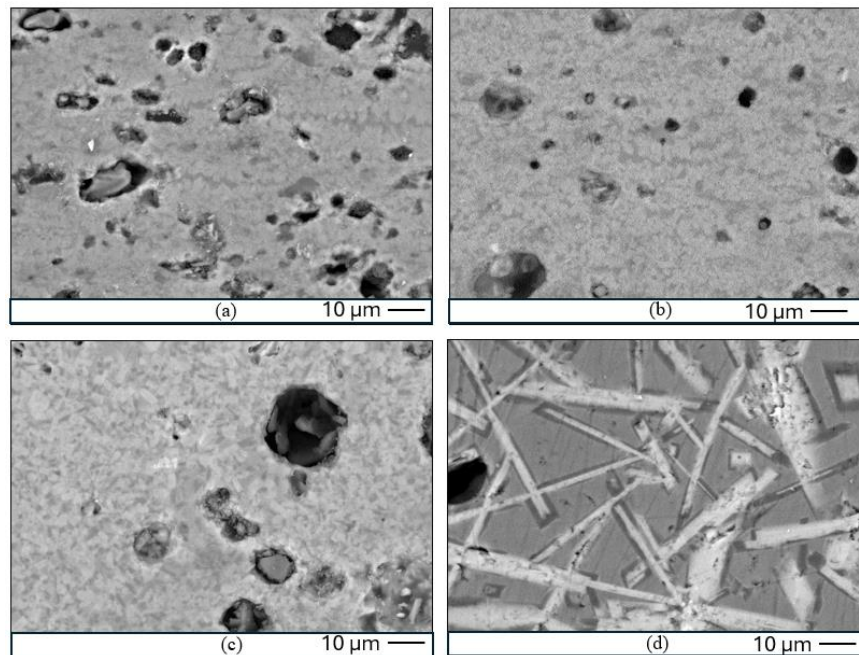
Figure 3. Scanning electron microscope images taken at 1000x magnification using a backscattered electron detector from the cross-sectional surfaces of the studied glazes: (a) S-900; (b) S-1000; (c) S-1100; (d) S-1200.

(a)

(b)
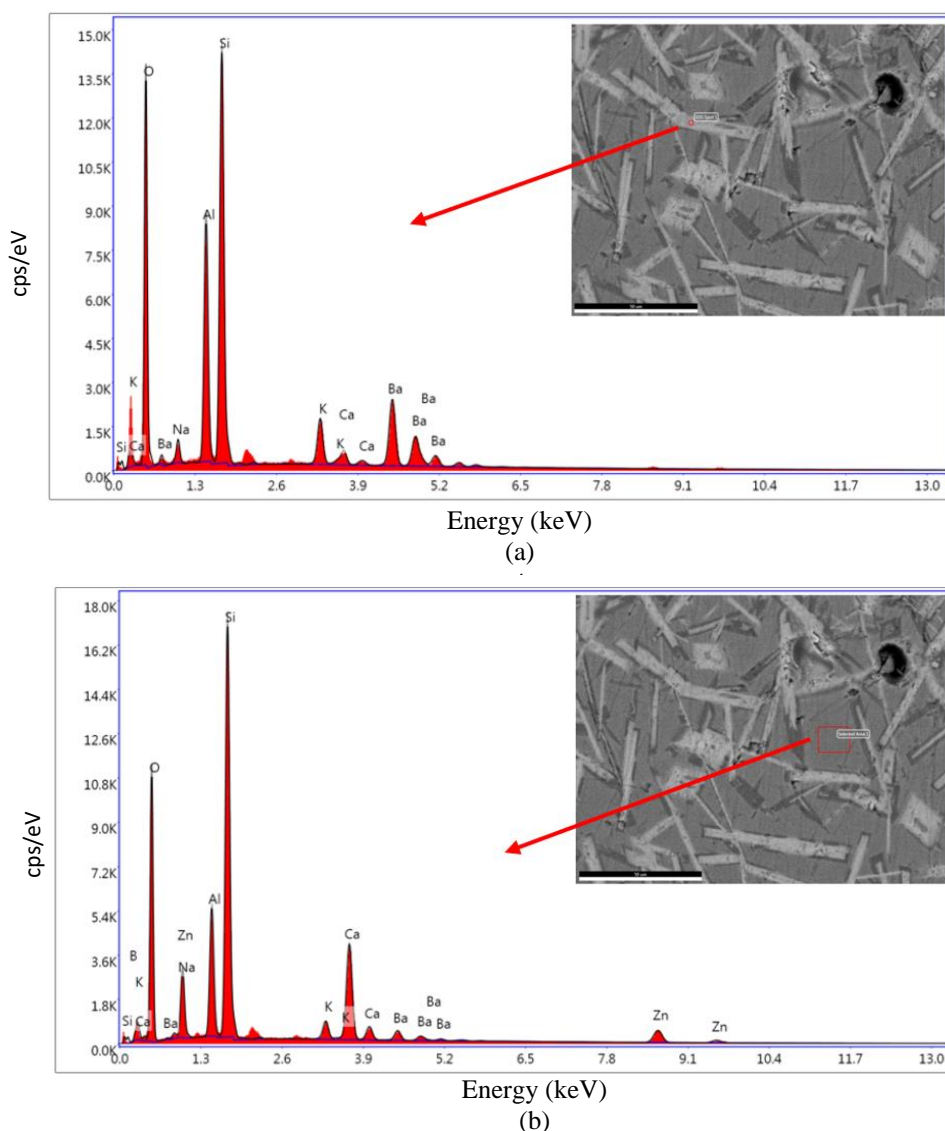
Figure 4. EDX pattern of the S-1200 coded glaze: (a) from the white area (crystalline phase); (b) from the black area (glassy phase).

Table 5. Element wt% measured in the glassy phase and crystal phase by FESEM-EDX

	Ba	Al	Si	O	Zn	B	Ca	K	Na
Crystal phase (a)	22.17	13.72	22.87	33.72	-	-	1.35	3.74	2.44
Glassy phase (b)	4.12	8.23	25.27	40.83	6.98	0.7	11.74	1.82	0.3

The images of the glazes before and after firing are presented in Figure 5, while the color values of the glazes after firing are shown in Figure 6. When the relevant glazes were examined, the samples with codes R-900 and R-1000 displayed an unfired glaze appearance. This outcome can be attributed to the high viscosity and porosity, which impeded sintering. The reduced densification led to the unfired matte appearance [24]. As the firing temperature rises, the L* value of the glazes decreases, indicating a reduction in opacity. However, no linear change was observed in the a* and b* values (Fig.6). The transparency/opacity of the glaze depends on several factors, including the type(s) of crystalline phase(s)

within the vitreous phase, the refractive index, the particle size of the crystals, the concentration of the crystalline phase, the glaze thickness, and the refractive index contrast between the vitreous and crystalline phases [6]. The refractive index of celsian crystals ranges from 1.59 to 1.61 [25], which is close to that of the remaining glassy phase. As a result, low-opacity ceramic glazes with low L* values were achieved in celsian-based glazes with S-1100 and S-1200 codes. Each glaze in the study exhibited a gloss value of less than 10 when measured at a 60° angle. The higher L* values in the S-900 and S-1000 glazes can be attributed to their unfired appearance, as well as the increased light scattering due to porosity and surface roughness.
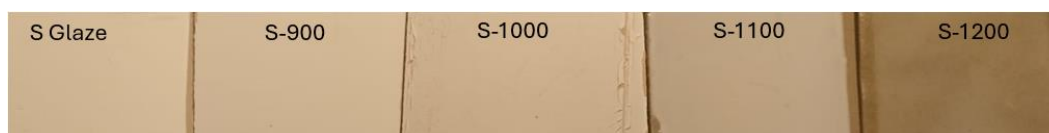

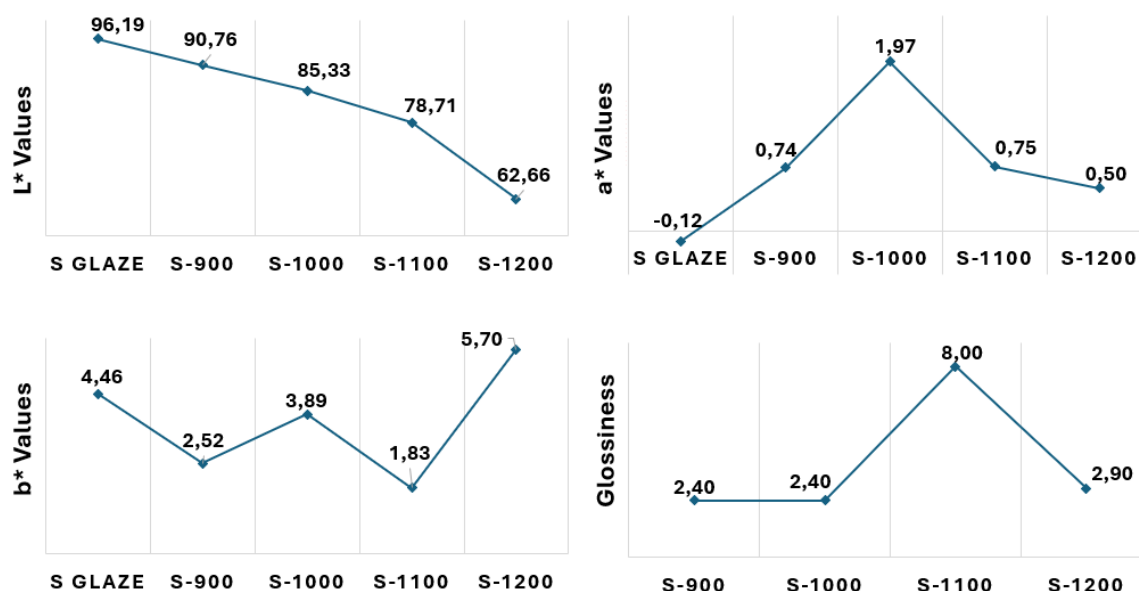**Figure 5.** Visual appearance of the glazes

Figure 6. Variations in the color indices and glossiness values of the glazes

4. CONCLUSIONS

This study investigates the effects of different firing temperatures on the glaze microstructure and color properties of barium-based frits. The findings are summarized as follows:

- With increasing firing temperature, the porosity of the glaze structure decreased, while the amount of the glassy phase increased. Celsian was the dominant phase in the S-1100 and S-1200 samples. As the temperature rose, the intensity of the celsian crystal peak within the glassy phase increased, and needle-like crystals formed, growing up to 100 microns.
- After firing at various temperatures, a matte opaque glaze with an appearance similar to an unfired glaze was obtained at 900°C and 1000°C, a satin opaque glaze at 1100°C, and a transparent matte glaze at 1200°C. The L* value of the glaze decreased from 90.76 at 900°C to 62.66 at 1200°C.

- Considering that wall tiles are typically fired at temperatures between 1050°C and 1150°C, floor tiles between 1150°C and 1200°C, and porcelain tiles between 1200°C and 1210°C in the ceramic industry, it was observed that, depending on the composition and firing temperature, matte glazes with different optical properties can be obtained by using barium-based frits.

- Even at temperatures above 1200°C, the preservation of celsian crystals within the transparent glaze structure shows that celsian based glaze structures could be achieved in porcelain tile regime.

ACKNOWLEDGEMENTS

CONFLICT OF INTEREST

The author stated that there are no conflicts of interest regarding the publication of this article.

CRediT AUTHOR STATEMENT

Betül Yıldız: Conceptualization, Methodology, Investigation, Formal analysis, Writing-original draft, Writing- Review&Editing

REFERENCES

[1]   Casasola R, Rincon JMa, Romero M. Glass–ceramic glazes for ceramic tiles: a review. J. Mater. Sci., 2012; 47, 553-582.

[2]   Kurama S, Gürkan, EA, Ozturk ZB, Karaca Y, Ubay E. Bazalt kesim atıklarının yer karosu mat sırlarda kullanım potansiyelinin araştırılması. ESOGÜ Müh. Mim. Fakültesi Dergisi, 2023; 31 (3), 816-825.

[3]   Ozturk ZB, Karaca Y, Ubay E. Enhancing thermal properties and surface quality of lappato glazed porcelain tiles through milling time optimization. Journal of Thermal Analysis and Calorimetry, 2024; 149, 7279-7287.

[4]   Yazırlı B, Sarı H, Kayacı K, Kara F. Effect of nucleating agent additions on gahnite based glass-ceramic glazes. J. Eur. Ceram. Soc., 2024; 44, 3344-3351.

[5]   Eppler RA, Eppler DR. Glazes and Glass Coatings. The American Ceramic Society, Ohio, 2000.

[6]   Taylor JR, Bull AC. Ceramic Glaze Technology. Oxford: Pergamon Press, 1986.

[7]   Bou E, Bordes MC, Felıu C, Gazulla MF, Ferrer F, Pasies G. Variables that determine the matt appearance of some ceramic floor and wall tile glazes. Proceeding of VII world congress on ceramic tile quality Qualicer, 2002; 349-364.

[8]   Campa F, Ginés F, Robles J. Matting of a transparent porous wall tile glaze by adding alumina. Proceeding of VI world congress on ceramic tile quality Qualicer, 2000; 115-117.

[9]   Kronberg T, Hupa L. The impact of wollastonite and dolomite on chemical durability of matte fast-fired raw glazes. J. Eur. Ceram. Soc., 2020; 40, 3327-3337.

[10]   Fortuna D. Sanitaryware. Faenza: Gruppo Editoriale; 2000.

[11]   Stefanov S, Batschwarov S. Ceramic glazes. Bauverlag; 1988.

[12]   Sheikhattar M, Attar H, Sharafi S, Carty WM. Influence of surface crystallinity on the surface roughness of different ceramic glazes. Materials Characterization, 2016; 118, 570-574.

[13]   Yıldız B. Effect of particle size distribution on the properties of celsian based glazes. Journal of Australian Ceramic Society, 2024.

[14]   Tezza VB, Scarpato M, Oliveira LFS, Bernardin AM. Effect of firing temperature on the photocatalytic activity of anatase ceramic glazes. Powder Technology, 2015; 276, 60-65.

[15]   Fröberg L, Kronberg T, Hupa L, Hupa M. Influence of firing parameters on phase composition of raw glazes. J. Eur. Ceram. Soc., 2007; 27, 1671-1675.

[16]   İmer C, Günay E, Öveçoğlu ML. Effects of firing temperatures and compositions on the formation of nano particles in lustre layers on a lead-alkali glaze. Ceramics International, 2016; 42, 17222-17228.

[17]   Zhao L, Zhang Y. Revealing the individual effects of firing temperature and chemical composition on raman parameters of celadon glaze. Ceramics, 2023; 6, 1263-1276.

[18]   Schab LM, Bondioli F, Ferrari AM, Manfredini T, Petter, CO, Fredel MC. Influence of firing temperature on the color developed by a $(Zr,V)SiO_4$ pigmented opaque ceramic glaze. J. Eur. Ceram. Soc., 2007; 27, 179-184.

[19]   Altındal F, Anil UE, Varisli SO, Ozturk B. Investigation of the effect of $BaO-Al_2O_3$ variations for BAS glass-ceramic glaze: Insights into thermal, phase, microstructural and surface features. J. Eur. Ceram. Soc.; 2024; 44, 3200-3209.

[20]   Partyka J, Lesniak M. Preparation of glass-ceramic glazes in the $SiO_2-Al_2O_3-CaO-MgO-K_2O-Na_2O-ZnO$ system by variable content of ZnO. Ceram. Int., 2016; 42, 8513-8524.

[21]   Kaczmarczyk K, Partyka J. Effect of $ZrSiO_4$ addition on Sintering and selected physicochemical parameters of glass-ceramic materials from the $SiO_2-Al_2O_3-Na_2O-K_2O-CaO-MgO$ system in the presence of barium oxide. Ceram. Int., 2019; 45, 22813-22820.

[22]   Han YX, Liu J, Yin WZ. Research on the mechanism of the dissociation of potassium shale during roasting. Adv. Mater. Res., 2009; 58, 155-162.

[23]   Reinosa RR, Rubio-Marcos F, Solera E, Bengochea MA, Fernandez JF. Sintering behaviour of nanostructured glass-ceramic glazes. Ceramics International, 2010; 36, 1845-1850.

[24]   Suvaci E, Yildiz B. Roles of CaO, MgO and SiO_2 on crystallization and microstructure development in diopside-based glass-ceramic glazes under industrial fast firing condition. J. Aust. Ceram. Soc., 2016.

[25]   Shannon RD, Shannon RC, Medenbach O, Fischer RX. Refractive index and dispersion of fluorides and oxides. J. Phys. Chem. Ref. Data, 2002; 31(4), 931-970.